EVALUATION OF VISCOELASTIC POISSON'S RATIO AND ANISOTROPY OF ASPHALT MIXTURES

A Thesis

Presented in Partial Fulfillment of the Requirements for the

Degree of Master of Science

with a

Major in Civil Engineering

in the

College of Graduate Studies

University of Idaho

by

Nasser A. Alanazi

Major Professor: Emad Kassem, Ph.D.

Committee Members: Fouad Bayomy, Ph.D.; S.J. Jung, Ph.D.;

Michael Maughan, Ph.D.

Department Administrator: Patricia J. S. Colberg, Ph.D.

August 2016

AUTHORIZATION TO SUBMIT THESIS

This thesis of Nasser A. Alanazi, submitted for the degree of Master of Science with a major in Civil Engineering and titled "Evaluation of Viscoelastic Poisson's Ratio and Anisotropy of Asphalt Mixtures," has been reviewed in final form. Permission, as indicated by the signatures and dates given below, is now granted to submit final copies to the College of Graduate Studies for Approval.

Major Professor: ________________________________ Date __________________
Emad Kassem, Ph.D.

Committee
Members: ________________________________ Date __________________
Fouad Bayomy, Ph.D.

________________________________ Date __________________
S.J. Jung, Ph.D.

________________________________ Date __________________
Michael Maughan, Ph.D.

Department
Administrator: ________________________________ Date __________________
Patricia J. S. Colberg, Ph.D.

ABSTRACT

The Poisson's Ratio (PR) of asphalt mixtures is an important input parameter in the constitutive models for pavement design and performance analysis. The design and performance analysis of asphalt pavements depend upon measuring proper material properties such as complex modulus and PR. The PR is often assumed to be time independent or it is calculated as the negative ratio of transverse to axial strains in the time domain under uniaxial loading when the time dependency is considered. This study presented and used accurate methods to calculate the viscoelastic PR under various loading conditions and demonstrated the error associated with using inaccurate methods for calculating the PR. The results of this study demonstrated that the viscoelastic PR increased with time in uniaxial unconfined tension and compression tests where shear relaxation was generally faster than dilatational relaxation. While the viscoelastic PR decreased with time in uniaxial confined compression tests where the dilatational relaxation was faster than the shear relaxation. In addition, the results demonstrated that asphalt mixtures with coarse aggregate gradations had lower viscoelastic PR compared to asphalt mixtures with finer aggregate gradations. Also, the viscoelastic PR was found to be sensitive to the aging and moisture conditions. The viscoelastic PR decreased with aging and increased with the level and time of moisture conditioning of the asphalt mixtures. Finally, the error introduced by incorrectly calculating the PR as the negative ratio of transverse to axial strains in the time domain was found to be significant in some cases while it was insignificant in others.

In addition, this study explored the anisotropy of asphalt mixtures. A proper understanding of the anisotropic behavior of asphalt mixtures is needed for an accurate multiaxial characterization of asphalt mixtures under different conditions. Asphalt mixtures are subjected to various loading conditions while in service. This study tested asphalt mixture specimens subjected to hydrostatic pressure to evaluate the degree of anisotropy at various conditions. The results demonstrated that the degree of anisotropy is dependent on the mix design. Asphalt mixtures with coarse aggregate gradations were found to have higher level of anisotropy compared to mixtures with finer aggregate gradations. In addition, the degree of anisotropy increased with the increase of confining pressure and temperature. Finally, the porosity of asphalt mixture had relatively significant impact on the degree of anisotropy. The anisotropy increased with the increase of porosity. The analysis of the anisotropy using the X-ray CT and image analysis techniques confirmed that the degree of anisotropy decreases with the increase of density.

ACKNOWLEDGEMENTS

In the name of Allah, the Compassionate, the Merciful.

I would like to deeply thank my advisor Dr. Emad Kassem for his endless support, patience, and great opportunity to successfully complete this thesis, without his guidance this work would be impossible.

Also, I would like to thank Dr. Fouad Bayomy and Dr. SJ Jung for their helpful inputs and fruitful comments on the thesis which improved its outcome.

My gratitude is extended to Dr. Zachary Grasley at Texas A&M University for his valuable comments and discussion on the viscoelastic PR. Also, the help of the staff of the McNew laboratory of Texas A&M Transportation Institute is greatly appreciated. Finally, I would like to thank my colleagues and friends at the University of Idaho for their encouragement and support.

DEDICATION

To my parents for their prayers and patience in my absence.

To my wife for her support and prayers.

TABLE OF CONTENTS

LIST OF FIGURES

LIST OF TABLES

CHAPTER 1 - INTRODUCTION

1.1 Overview

The Poisson's Ratio (PR) of asphalt mixtures is an important input parameter in the constitutive models for pavement design and performance analysis. The design and performance analysis of asphalt pavements depend upon measuring proper material properties such as complex modulus (E*) and PR. The PR is commonly considered to be time-independent assuming that asphalt pavements respond elastically to the applied loads (Huang et al 2007; Maher and Bennert 2008). However, this assumption is not accurate for asphalt mixtures. Several studies opposed the independency of PR on time, and showed that it is time- and temperature-dependent (Benedetto et al. 2007a, b). Moreover, when time dependency is considered, PR is commonly calculated as the negative ratio of time-dependent transverse strain to the time-dependent axial strain. Furthermore, other researchers showed that this assumption does not hold for all different loading conditions because of the dependency of the PR on the stress or strain history (Kassem et al. 2013).

The Correspondence Principle is utilized to allow the use of the elastic constitutive equations for viscoelastic materials in Laplace transform domain. Then, those relations are converted to time domain under the assumption that the asphalt concrete mixes are homogenous and isotropic materials (Grasley and Lange 2007; Kassem at al. 2013; Tschoegl et al. 2002).

Several studies have been conducted to quantify the anisotropy of asphalt mixtures and evaluate its effect on the mechanical properties of asphalt mixtures (Mamlouk et al. 2002; Masad et al. 2002; Underwood et al. 2005; Wang et al. 2005). Some researchers found that the anisotropy is affecting the mechanical properties of asphalt mixtures (Masad et al. 2002; Wang et al. 2005). However, others concluded that the anisotropy has little or no affect, and can be ignored (Mamlouk et al. 2002). The anisotropy of asphalt mixtures can be classified into two types: the inherent anisotropy and induced anisotropy (Masad et al 2002; Underwood et al. 2005).

There are different methods used to quantify the anisotropy of asphalt mixtures (Mamlouk et al. 2002; Masad et al 2002; Underwood et al. 2005; Wang et al. 2005). Underwood et al. (2005) proposed a simple method to quantify the anisotropy using a hydrostatic test. This method was validated and used in this study to evaluate the effect of several parameters including mixture type, confining pressure, temperature, and porosity on the anisotropy of asphalt mixtures.

1.2 Problem Statement and Objectives

The PR of asphalt mixtures is a fundamental material property and needed parameter for pavement design and performance analysis. The PR is often assumed to be time independent or it is calculated as the negative ratio of transverse to axial strains in the time domain in uniaxial creep tests when the time dependency is considered. The objectives of the first part of this study is to present and use accurate methods to calculate the Viscoelastic Poisson’s Ratio (VPR) of asphalt mixtures and evaluate the effect of various parameters including loading mode, loading rate, and environmental conditions on the VPR. In addition, determining the associated error introduced by incorrectly determining the PR as the negative ratio of transverse to axial strains in the time domain.

In addition, the second objective of this study is to explore the anisotropy of asphalt mixtures. A proper understanding of the anisotropic behavior of asphalt mixtures is needed for an accurate multiaxial characterization of asphalt mixtures under different conditions. Asphalt mixtures are subjected to various loading conditions while in service. In this study, the evaluation of the anisotropy is based on a simple method. This method relies on measuring the axial and radial strains during the application of hydrostatic pressure. In addition, the effect of several parameters including mixture type, temperature, level of confining pressure, and porosity on the level of anisotropy of asphalt mixtures were investigated.

1.3 Research Tasks

The above objectives were achieved by conducting the following tasks:

- Task 1: Conduct Literature Review

  The author conducted a thorough literature review and provided a background on different definitions and calculations of PR of asphalt mixtures and the use of the correspondence principle to calculate the VPR. In addition, the author provided a summary on methods used to quantify the anisotropy of asphalt mixtures and effect of the anisotropy on the mechanical properties of asphalt mixtures.

- Task 2: Prepare and Condition the Test Specimens

  Under this task, cylindrical test samples were prepared in accordance to AASHTO T 312. At least two replicates were tested at different conditions. Some of the test specimens were conditioned to simulate aging and wet conditions. The aging process was accelerated by placing the test samples in an environmental chamber at

60°C for three and six months, while test specimens were conditioned following AASHTOO T-283-07 to simulate the wet conditions.

- Task 3: Conduct the Laboratory Testing

  Laboratory experiments were conducted at various conditions (loading mode [tension or compression], loading rate, temperature, etc.). The following parameters were recorded during the laboratory experiments (load, time, temperature, confining pressure, and axial and radial deformations). A total number of four linear variable differential transformers (LVDTs) were used to measure the deformations in the tension tests; three LVDTs were used to measure the axial deformation and one circumferential LVDT to measure the radial deformation. While a total number of six LVDTs were used to measure the deformations in the compression tests, three LVDTs were used to measure the axial deformation and three LVDTs were used to measure the radial deformations.

- Task 4: Comprehensive Evaluation of the VPR at Different Conditions

  Under this task, the author presented and used accurate procedures to calculate the VPR at various conditions. The measured data were analyzed and the VPR values were compared to the PR values to calculate the percent error. In addition, the VPR at various conditions were compared to evaluate the effect of applied loading rates, influence of the environmental factors, and influence of the confining pressure on the VPR.

- Task 5: Explore the Anisotropy at Various Conditions

  Under this task, the test specimens were subjected to different levels of hydrostatic pressure for two hours and radial and axial strains were calculated with time. The test was conducted at different temperatures and asphalt mixtures with different mix design and porosity. Finally, the X-ray Computed Tomography (CT) and image analysis techniques were used to study the anisotropy of asphalt mixtures with different porosity.

1.2 Organization of the Study

Chapter 1 provides an overview of the research effort, problem statement and objectives, research tasks, and study organization. Chapter 2 provides a literature review on PR of asphalt mixtures including definitions of PR, methods used to calculate the PR, and main findings of previous studies. In addition, Chapter 2 provides a review of anisotropy of asphalt mixtures and the influence of anisotropy on the mechanical properties of asphalt mixtures.

Chapter 3 provides information about the experimental program including the design of the asphalt mixtures, test sample preparation and conditioning, and test protocol and setup. Chapter 4 presents the procedures used by the author to calculate the VPR of asphalt mixtures with different mixture design under different loading conditions. In addition, Chapter 4 presents the results of the experimental program and analysis of the VPR.

Chapter 5 presents the findings of the evaluation of the anisotropy of asphalt mixtures using mechanical loading and X-ray CT and image analysis techniques. Chapter 6 summarizes the main findings of this study and provides recommendations for future studies.

CHAPTER 2 – LITERATURE REVIEW

2.1 Review of PR of Asphalt Mixtures

2.1.1 Definition of PR

In this section, several definitions of PR were discussed and summarized. About two centuries ago, Poisson (1829a, b) defined the PR as the negative radial strain divided by the vertical strain (Eq. 2.1).

$$\upsilon = -\frac{\varepsilon_{ii}}{\varepsilon_{jj}} \tag{2.1}$$

Poisson’s definition is applicable for elastic materials only. Normally, PR of an elastic material is determined by static experimental measurements of strains in two orthogonal directions for a homogenous elastic matter (Hilton 2001). When a constant (time independent) load is applied in one direction, a constant elastic PR results because all the linear normal strains are constants too. In addition, when a time dependent and homogeneous elastic strain is applied in one direction and there is no effect from the body forces, the other strains will have the same time function, so the elastic PR would be constant (Hilton 2001).

However, asphalt mixtures and bitumen have viscous and elastic properties, so they cannot be treated as elastic materials. Benedetto et al. (2007a, b) stated that PR is temperature and time dependent. Hilton (2001) presented a concise summary of different definitions of time dependent PR found in the literature. Some of these definitions are presented as in Eqs. 2.2 and 2.3:

$$\upsilon(t) = -\frac{\varepsilon_{22}(t)}{\varepsilon_{11}(t)} \tag{2.2}$$

$$v(t) = -\frac{\varepsilon_{22}(t)}{\varepsilon_{11}},\ \varepsilon_{11} = constant \tag{2.3}$$

where $\varepsilon_{22}(t)$ is the time-dependent radial strain and $\varepsilon_{11}(t)$ is the time-dependent axial strain. Teschoegl et al. (2002) defined the PR as the negative ratio of time-dependent radial strain to the time-independent axial strain, where the axial strain is held constant as in the relaxation tests (Eq. 2.3). Also, Teschoegl et al. (2002) pointed out that Eq. 2.2 can be used for materials that are subjected to creep or uniaxial loading. Hilton (2001) mentioned that some researchers used Eq. 2.2 for asphalt mixtures that are subjected to creep loading, and Eq. 2.3 with the relaxation test, which is in good agreement with Tschoegl et al. (2002). Also, Hilton (2001) emphasized that Eq. 2.3 is a special case of Eq. 2.2.

2.1.2 Sensitivity of Asphalt Pavement Distress with Constant PR

Maher and Bennet (2008) conducted a sensitivity analysis of asphalt pavement performance using the Mechanistic Empirical Pavement Design Guide (MEPDG) software. The sensitivity analysis included an assumption of several PR values of asphalt layer; 0.15, 0.3, and 0.45. Figure 2.1 shows an example of the predicted total pavement rutting and longitudinal cracks. According to the researchers, the higher the PR, the less rutting on the pavement. Higher PR indicates more toleration for the horizontal deflection and transmittal for the applied stress. In addition, the longitudinal cracking significantly decreased with higher PR because the higher the PR the less induced vertical stresses. Therefore, assuming constant values of PR may underestimate or overestimate the performance analysis for asphalt pavements.

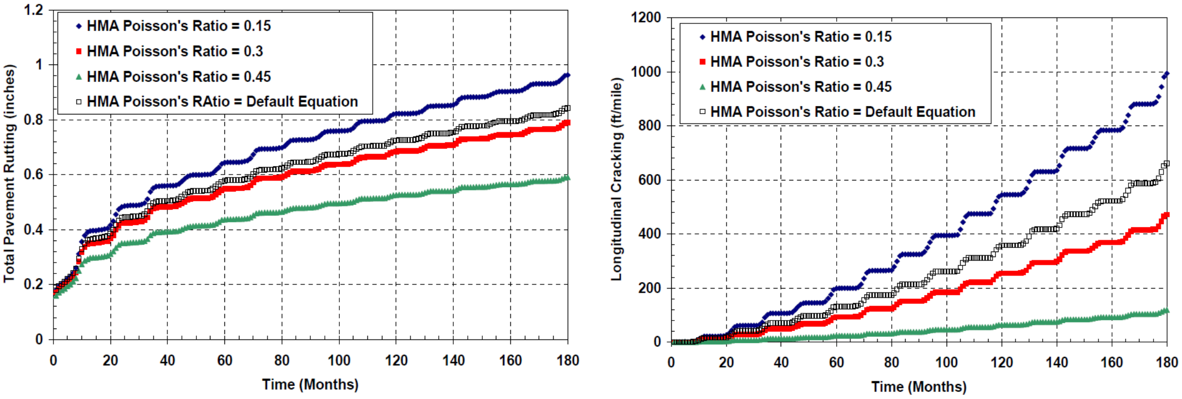

(a) Total Pavement Rutting (b) Longitudinal Cracking

Figure 2.1 (a) Sensitivity of Total Pavement Rutting and (b) Longitudinal Cracking on Variation of PR Parameter from MEPDG Software (Maher and Bennet 2008)

2.1.3 VPR Calculations

One of the tests used by researchers to calculate the VPR is the Brazilian test or indirect tension (IDT) test. This test has gained attention because of its ability to test both field cores and laboratory specimens (Lee and Kim 2009). Lee and Kim (2009) performed the IDT test on cores extracted from the field to determine the creep compliance and VPR. These cores were 5.9 in. in diameter and 1 in. thick. The test samples were conditioned at 10°C for 24hrs before testing.

The researchers performed two IDT tests; 1) IDT creep test following AASHTO T-322 (AASHTO 2007b) and 2) complex IDT test according AASHTO TP-62 (AASHTO 2007a). Lee and Kim (2009) also derived expressions for VPR, and creep compliance from both the IDT creep test and from the complex modulus IDT test as given below.

The plane stress constitutive equations for linear, elastic, and isotropic materials are:

$$\varepsilon_x = D\left[\sigma_x - \upsilon\sigma_y\right] \tag{2.4}$$

$$\varepsilon_y = D\left[\sigma_y - \upsilon\sigma_x\right] \tag{2.5}$$

where σ_y is the compressive vertical stress and σ_x is the tensile horizontal stress that are resulted from the IDT creep test. D and υ are the compliance and PR of an elastic material, respectively. Lee and Kim (2009) used the Correspondence Principle (which is discussed later in this chapter in detail) for viscoelastic materials through the Laplace transform (LT) on Eq. 2.4, and 2.5.

$$\hat{\varepsilon}_x(s) = s\widehat{D}(s)\left[\hat{\sigma}_x(s) - s\hat{\mu}(s)\hat{\sigma}_y(s)\right] \tag{2.6}$$

$$\hat{\varepsilon}_y(s) = s\widehat{D}(s)\left[\hat{\sigma}_y(s) - s\hat{\mu}(s)\hat{\sigma}_x(s)\right] \tag{2.7}$$

Eq. 2.6 and 2.7 were solved for $\hat{\mu}(s)$ that yields:

$$\hat{\mu}(s) = \frac{\hat{\varepsilon}_x\hat{\sigma}_y - \hat{\varepsilon}_y\hat{\sigma}_x}{s(\hat{\varepsilon}_x\hat{\sigma}_x - \hat{\varepsilon}_y\hat{\sigma}_y)} \tag{2.8}$$

where $\hat{\mu}(s)$ is VPR in LT domain.

Lee and Kim (2009) stated that for IDT creep test, the creep strain is represented by a fitted power function as given in Eq. 2.9

$$\varepsilon(t) = \varepsilon^0 + \varepsilon^1 t^m \tag{2.9}$$

Expand the above equation using Prony series would result in Eq. 2.10.

$$\varepsilon(t) = \varepsilon_0 + \frac{1}{\eta_\varepsilon}t + \sum_{i=1}^{N}\varepsilon_i\left[1 - e^{-t/\tau_i}\right] \tag{2.10}$$

By taking LT of Eq. 2.10, the following equation (Eq. 2.11) can be obtained.

$$\hat{\varepsilon}(s) = \frac{\varepsilon_0}{s} + \frac{1}{\eta_\varepsilon \,.\, s^2} + \sum_{i=1}^{N}\varepsilon_i\left[\frac{1}{s} - \frac{1}{s + 1/\tau_i}\right] \tag{2.11}$$

Equation 2.11 can be used for LT vertical and horizontal strains, and substituted in Eq. 2.8. After that, Eq. 2.8 is expanded using partial fraction expansion, and finally inverted to time domain which yields Eq. 2.12.

$$\mu(t) = C_1 + C_2 e^{-t/\lambda_1} + \cdots + C_{N+2} e^{-t/\lambda_{N+1}} \tag{2.12}$$

where $\mu(t)$ is VPR in time domain.

Once the creep VPR is determined, then the creep compliance can be found by rearranging Eq.2.6, and 2.7 as

$$\hat{D}(s) = \frac{\hat{\varepsilon}_x(s)}{s(\hat{\sigma}_x(s) - s\hat{\mu}(s)\hat{\sigma}_y(s))} \tag{2.13}$$

$$\hat{D}(s) = \frac{\hat{\varepsilon}_y(s)}{s(\hat{\sigma}_y(s) - s\hat{\mu}(s)\hat{\sigma}_x(s))} \tag{2.14}$$

Equations 2.13 and 2.14 are used to determine the vertical and horizontal creep compliances in LT, respectively. Lee and Kim (2009) followed the same derivation steps of the creep VPR to derive the creep compliance in time domain, the reader is referred to Lee and Kim (2009) and Kim et al. (2010) for more information. Also, Lee and Kim (2009) presented the derivations of frequency-dependent VPR [$\mu^*(\omega)$] and creep compliance [$D^*(\omega)$] from the complex modulus test.

Lee and Kim (2009) presented a comparison between the creep compliance determined from the creep test and the creep compliance from the complex modulus test as presented in Fig. 2.2(a). They pointed out that the creep compliance from the complex test is lower than the one from creep test. The researchers stated the reason of that difference is the applied load is not constant at zero loading time in the creep test. Also, they indicated that

that the VPR is less influenced by the discrepancy between the two compliances and could be determined from any one as presented in Fig. 2.2(b).

Furthermore, Lee and Kim (2009) studied the sensitivity of assuming constant values of PR on the creep and complex compliances. Three constant values of PR were assumed (0.25, 0.35, and 0.45). Figures 2.3 and 2.4 show the creep compliances the field cores at different PR values, determined from the IDT creep test and from the complex modulus test, respectively.

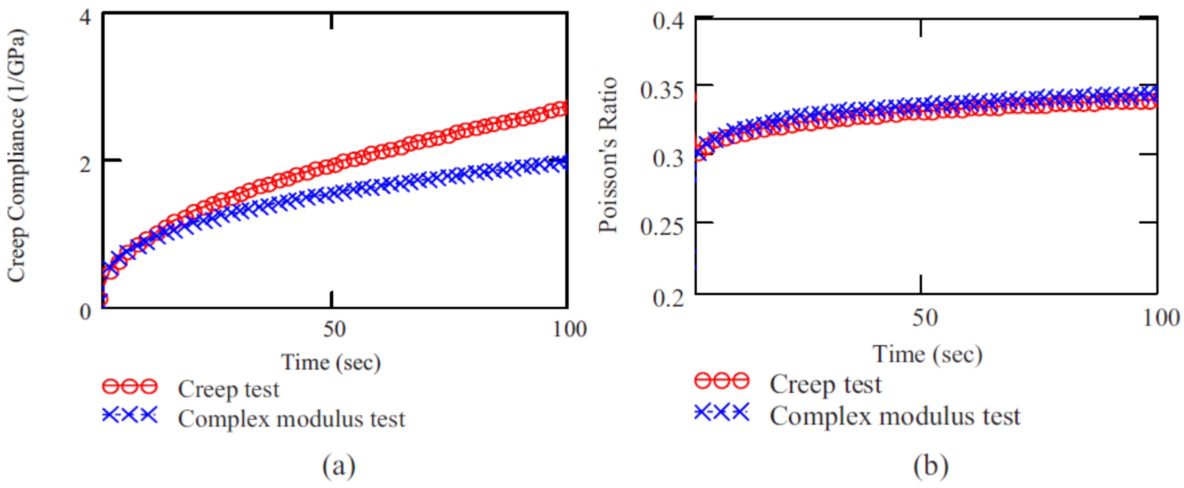

Figure 2.2 Comparison of (a) Creep Compliance; (b) PR obtained from IDT Creep and Complex Modulus (Lee and Kim 2009)

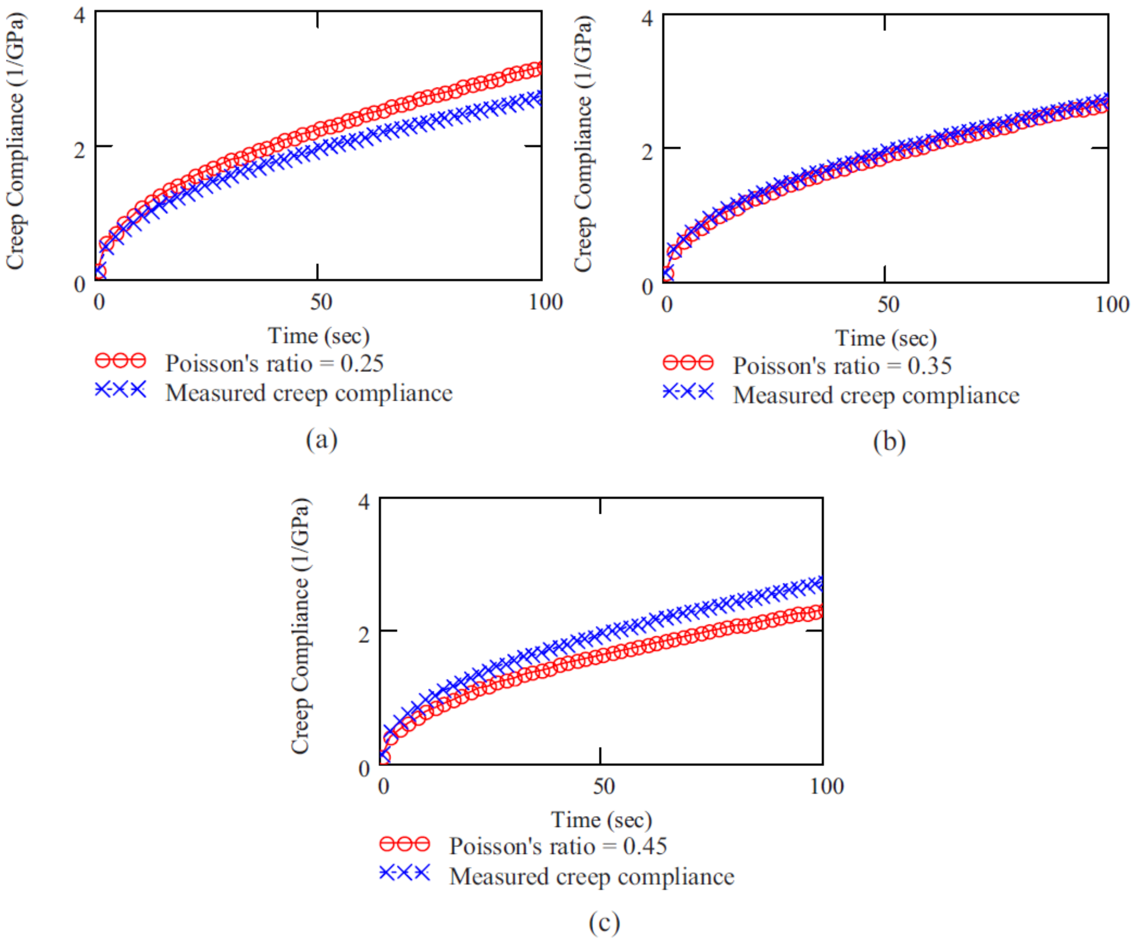

(a) (b) (c)

Figure 2.3 Creep Compliance from IDT Creep Test with (a) 0.25 PR; (b) 0.35 PR; and (c) 0.45 PR (Lee and Kim 2009)

Lee and Kim (2009) found that PR of 0.35 provided exactly the same creep compliance determined from both the IDT Creep Test and the complex modulus IDT Test. The PR of 0.35 was the terminal value of the PR as shown in Fig. 2.2(b). Moreover, the researchers stated that the results demonstrated that the PR has a significant effect on the calculated compliances and therefore it is important to determine the time- or frequency-dependent VPR to accurately predict the creep compliances.

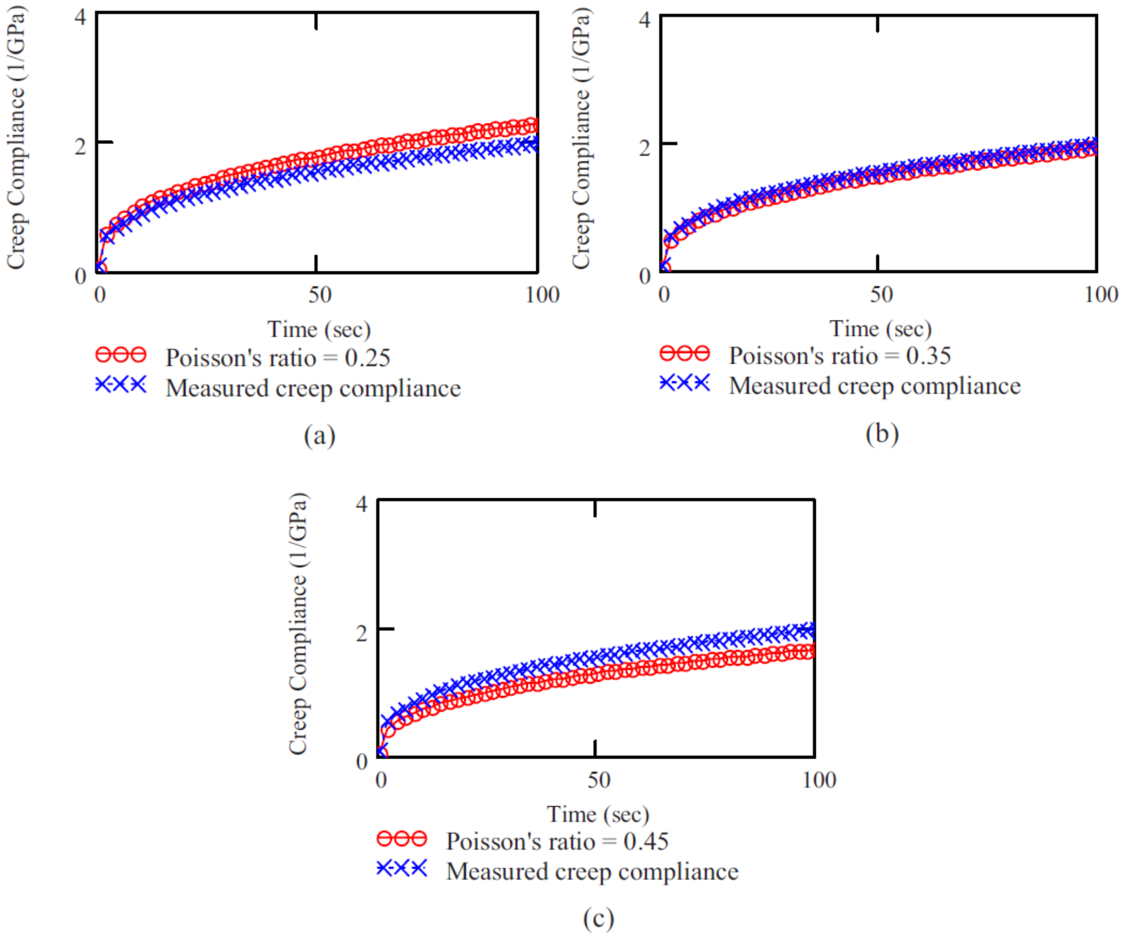

(a)

(b)

(c)

Figure 2.4 Creep Compliance from Complex Modulus IDT with (a) 0.25 PR; (b) 0.35 PR; and (c) 0.45 PR (Lee and Kim 2009)

2.1.4 Complex PR (ν*)

Benedetto et al. (2007a) introduced a procedure to calculate what was called the complex Poisson's ratio (ν*), as a function of temperature and frequency and developed a master curve similar to complex modulus (E*) master curve of asphalt mixtures. The test samples were 4.72 in. in height and 3.15 in. diameter of bitumen and mastic.

They applied sinusoidal stress $[\sigma_1(t)]$ and measured the resulted vertical $[\varepsilon_1(t)]$ and horizontal $[\varepsilon_2(t)]$ strains. The measured stress and strains were function of time (or frequency) and calculated as follows:

$$\varepsilon_1(t) = \varepsilon_{01}\sin(\omega t) \tag{2.15}$$

$$\varepsilon_2(t) = \varepsilon_{02}\sin(\omega t + \pi + \phi_v) = -\varepsilon_{02}\sin(\omega t + \phi_v) \tag{2.16}$$

$$\sigma_1(t) = \sigma_{01}\sin(\omega t + \phi_E) \tag{2.17}$$

where, ϕ_E is the phase angle between the vertical strain and the axial stress and ϕ_v is the phase angle between the vertical and radial strains. The researchers considered the complex number (j = -1$^{0.5}$) and substituted into it into the Eqs. 2.15, 2.16, and 2.17 to yield the following equations.

$$\varepsilon_1{}^*(t) = \varepsilon_{01}\mathrm{e}^{j\omega t} \tag{2.18}$$

$$\varepsilon_2{}^*(t) = \varepsilon_{02}\mathrm{e}^{j(\omega t+\pi+\phi_v)} = -\varepsilon_{02}\mathrm{e}^{j(\omega t+\phi_v)} \tag{2.19}$$

$$\sigma_1{}^*(t) = \sigma_{01}\mathrm{e}^{j(\omega t+\phi_E)} \tag{2.20}$$

The complex Young's modulus (E*), shear modulus (G*), and complex PR (ν*) can be calculated as follows:

$$E^*(\omega) = \frac{\varepsilon_1{}^*}{\sigma_1{}^*} = |E^*(\omega)|\mathrm{e}^{j\phi_E} \tag{2.21}$$

$$\mathrm{v}^*(\omega) = \frac{-\varepsilon_2{}^*}{\varepsilon_1{}^*} = |\mathrm{v}^*(\omega)|\mathrm{e}^{j\phi_v} \tag{2.22}$$

$$G^*(\omega) = \frac{E^*(\omega)}{2[1+\mathrm{v}^*(\omega)]} \tag{2.23}$$

Benedetto et al. (2007a) applied six frequencies from 0.3 Hz to 10 Hz at eight different temperatures from -30°C to 40°C, but they limited the temperature to 0°C for bitumen and mastic to prevent flowing of the specimens.

The results of complex PR and the phase angle for pure bitumen of a penetration grade of 50/70 are as shown in Fig. 2.5.

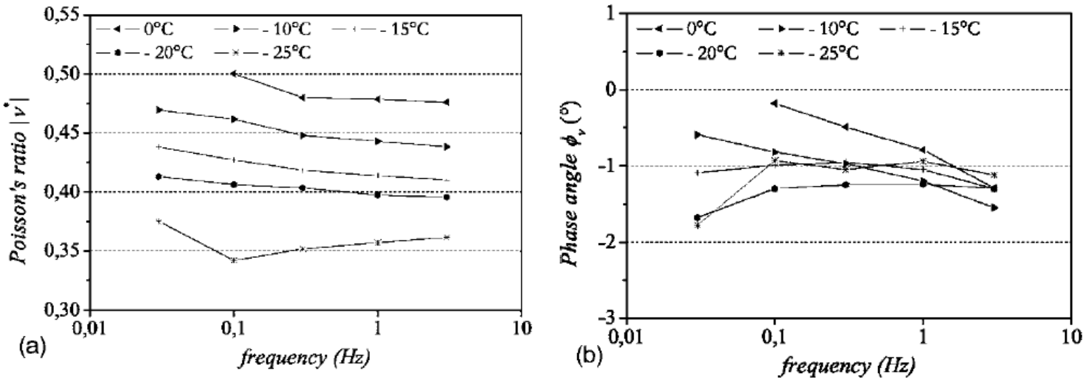

Figure 2.5 (a) Complex PR (ν*) and (b) the Phase Angle at Different Frequencies and Temperatures (Benedetto et al. 2007a)

According to Benedetto et al. (2007a), the phase angle varied from 0° to -1.8° which indicated a slight delay in the response of the radial strain compared to vertical strain as in Fig.2.5 (b). In addition, Benedetto et al. (2007a) calculated and complex PR and phase angle for mastic samples, and they noticed a similar trend to the pure binder samples (Fig. 2.5). The reader is referred to (Benedetto et al. 2007a) for more information.

Benedetto et al. (2007a) generated a master curve for E* presented in Fig. 2.6 and a master curve for the complex PR (ν*) as given in Fig.2.7 at a reference temperate of 0°C and same shift factor for both ν* and E*. The authors concluded that based on the time-temperature superposition to construct a master curve for E*, it could be utilized to construct a similar plot for ν*. In addition, ν* ranged from 0.5 at low frequency and high temperature to 0.35 at high frequency and low temperature, which indicated that PR is temperature- and frequency- (or time) dependent.

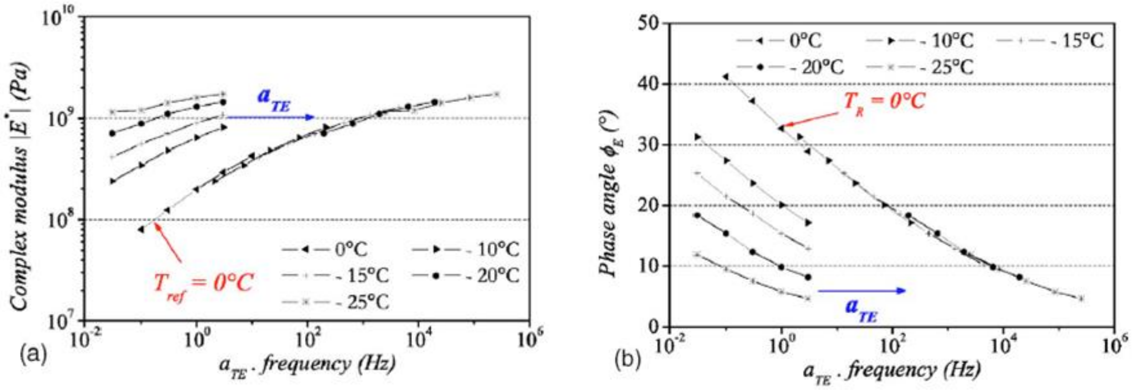

Figure 2.6: (a) Master Curve for E* with 0°C as a Reference Temperature; and (b) Phase Angle (ϕ_E) for Pure Bitumen (Benedetto et al. 2007a)

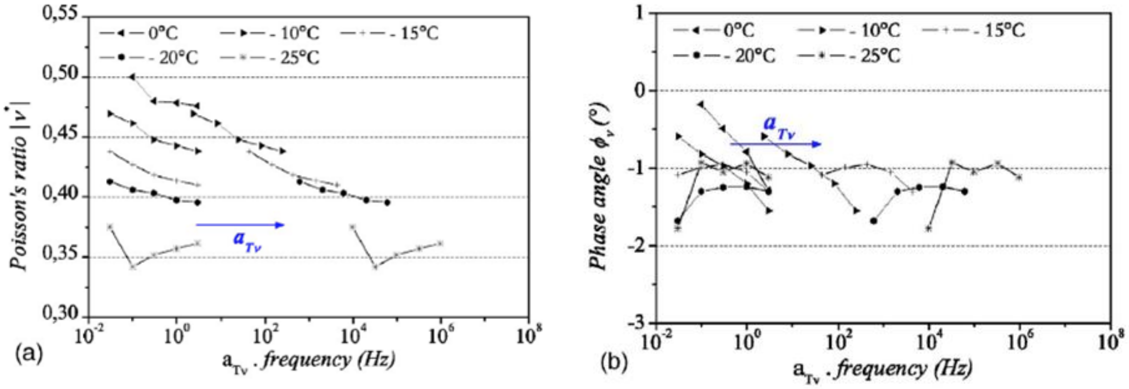

Figure 2.7: (a) Master Curve for ν* with 0°C as a Reference Temperature; and (b) Phase Angle ($\phi_ν$) for Pure Bitumen (Benedetto et al. 2007a)

2.1.5 The Correspondence Principle

For elastic materials such as steel and other metals, the constitutive relationships between PR (ν), Young's (E), Shear (G), and bulk (K) moduli can be found according to the following simple equations (Tschoegl et al 2002):

$$G = \frac{E}{2(1+\nu)} \tag{2.24}$$

$$K = \frac{E}{3(1-2\nu)} \tag{2.25}$$

$$E = \frac{9KG}{3K+G} \tag{2.26}$$

$$\nu = \frac{3K-2G}{2(3k+G)} \tag{2.27}$$

Flexible pavements are assumed to act elastically under light axel loads at low temperatures. However, as traffic loads and temperature increase, the elastic behavior alone does not hold. Under the assumptions that the asphalt mixtures are isotropic and homogeneous Eqs. 2.24 and 25 may be written as (Elseifi et al. 2006; Kim et al. 2008):

$$G(t) = \frac{E(t)}{2(1+\nu)} \tag{2.28}$$

$$K(t) = \frac{E(t)}{3(1-2\nu)} \tag{2.29}$$

where PR is time independent and E(t), G(t), and K(t) are time dependent. However, these equations cannot be used directly for viscoelastic materials. The Correspondence Principle was formulated to allow the use of elastic constitutive relations for viscoelastic materials in LT domain.

According to Kassem et.al (2013), the constitutive equation that describes the general relationship for linear viscoelastic, homogenous, isotropic materials is defined in Eq. 2.30

$$\varepsilon_{ij}(t) = \int_0^t S_{ijkl}\,(t-t')\,\frac{\partial \sigma_{kl}(t')}{\partial t'}\,dt' \tag{2.30}$$

where S_{ijkl} = component of viscoelastic compliance, $\sigma_{kl}(t)$ = component of stress tensor, and $\varepsilon_{ij}(t)$ = component of strain tensor. The integral operator means the equation is derived for linear elastic solutions and is not directly applicable for viscoelastic materials because of the dependency on stress or strain history. The LT function f(s) of a function of time is written as:

$$f(s) = \int_0^\infty f\,(t)exp(-st)dt = L[f(t)] \tag{2.31}$$

where L is the LT notation, and s = a + jω.

Kassem et al. (2013) pointed out that Read (1950) derived a method for utilizing the elastic constitutive equations for viscoelastic materials in LT domain, so Eq. 2.30 can be expressed in algebraic form in LT domain as:

$$\bar{\varepsilon}_{ij}(s) = s\overline{S_{ijkl}}(s)\overline{\sigma_{kl}}(s) \tag{2.32}$$

where s is the LT variable, and the transformed variables are noted with overbars. Eq. 2.32 is valid for viscoelastic materials, and then could be inverted to time domain.

Therefore, the constitutive equations of elastic materials are valid for viscoelastic materials in Laplace or Fourier domain, and then retransformed to time or frequency domain under the assumption that the material is isotropic and homogeneous (Teschoegl et al. 2002; Kassem et al. 2013).

The elastic moduli's reciprocals or compliances could have direct relations such that

$$D = \frac{1}{E} \tag{2.33}$$

$$G = \frac{1}{J} \tag{2.34}$$

where D, and J are the elastic and shear compliances respectively. The same relations are applicable for viscoelastic materials, but in LT with s- multiplied as (Tschoegl et al 2002):

$$\overline{D}(s) = \frac{1}{s} * \frac{1}{\overline{E}(s)} \tag{2.35}$$

$$\overline{G}(s) = \frac{1}{s} * \frac{1}{\overline{J}(s)} \tag{2.36}$$

$$\overline{E}(s) * \overline{D}(s) = \frac{1}{s^2} \tag{2.37}$$

and the same concept is applied on the bulk modulus. Also, the viscoelastic Young's modulus in LT is expressed as (Tschoegl et al 2002):

$$s\overline{E}(s) = \frac{\overline{\sigma}(s)}{\overline{\varepsilon}(s)} \rightarrow \overline{E}(s) = \frac{1}{s} * \frac{\overline{\sigma}(s)}{\overline{\varepsilon}(s)} \tag{2.38}$$

Also, applying the correspondence principle to Eq. 2.24 to 2.27 leads to (Tschoegl et al 2002):

$$\overline{G}(s) = \frac{\overline{E}(s)}{2[1+s\overline{v}(s)]} \tag{2.39}$$

$$\overline{K}(s) = \frac{\overline{E}(s)}{3[1-2s\overline{v}(s)]} \tag{2.40}$$

$$\overline{E}(s) = \frac{9\overline{K}(s)\overline{G}(s)}{3\overline{K}(s)+\overline{G}(s)} \tag{2.41}$$

$$\overline{v}(s) = \frac{1}{s} * \frac{3\overline{K}(s)-2\overline{G}(s)}{2\left[3\overline{k}(s)+\overline{G}(s)\right]} \tag{2.42}$$

Kim et al. (2010) derived expressions for viscoelastic Young's, shear, and bulk moduli of viscoelastic materials under IDT creep test in time domain. They used Eq. 2.37 to find the Young's modulus, and then Eq. 2.39 or 2.40 to find the shear or bulk moduli. They used the same derivation procedure of VPR, and creep compliance (as presented in Eqs. 2.11 & 2.12) to find the moduli in time domain. Figure 2.8 shows the resulted moduli after inverting them to time domain.

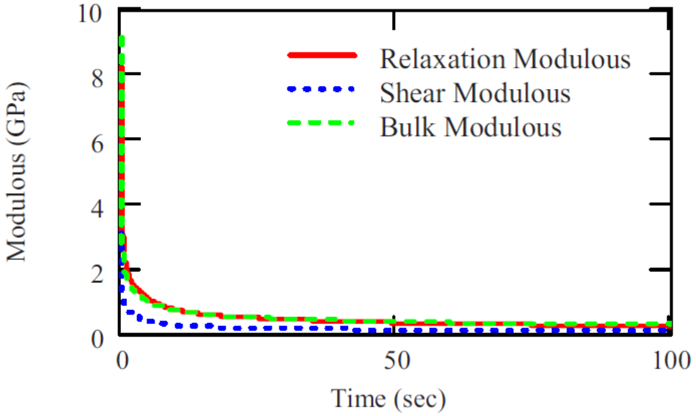

Figure 2.8 Relaxation, Shear, and Bulk Moduli from IDT Creep Test (Kim et al. 2010)

The author discussed the procedure used to calculate the VPR of asphalt mixtures in Chapter 4.

2.2 Reviews on Anisotropy of Asphalt Concrete Mixes

2.2.1 Introduction

Several performance models of asphalt mixtures assume that asphalt mixtures are isotropic materials (Kassem et al. 2013; Tschoegl et al 2002). However, it is well established that the asphalt mixtures are anisotropic materials. Mamlouk et al. (2002) showed that the asphalt mixtures are isotropic materials in tension and compression loading. However, Underwood et al. (2005) observed that the anisotropy has slight effect on strength from the tensile loading and considerable effect under the compressive loading, but not on the initial modulus. Also, other studies showed that the asphalt mixtures are generally anisotropic (Masad et al. 2002; Tashman et al. 2001; Wang et al. 2005).

The anisotropy of asphalt mixtures can be classified into two types: 1) the inherent anisotropy which is based on the internal structure of the material such as the preferential orientation of the longest axes of the aggregate and air void distribution with respect to the compaction direction; and 2) the induced anisotropy which is based on the response of the material to the applied stresses. (Masad et al. 2002; Underwood et al. 2005)

2.2.2 Inherent Anisotropy

Tashman et al. (2001) studied the inherent anisotropy using image analysis techniques of field and laboratory asphalt mixture samples. The laboratory samples were prepared at different parameters including height, angle of gyration, compaction pressure, and mold and base plate temperatures. The samples were sliced vertically and horizontally to compare and study the internal structure of field and laboratory samples.

One of the aspects that Tashman et al. (2001) explored is the orientation of longest axis of aggregates with respect to the compaction direction. The researchers used image analysis techniques to characterize the internal structure of asphalt mixtures. These techniques rely on processing digital images to separate the object(s) of interest from all other constituents. In their study, they separated the aggregates from the air voids and mastic. In addition, they developed expressions to characterize the preferred orientation of the aggregates as given in Eqs. 2.43 through 2.45.

$$\Delta = \frac{100}{N}\sqrt{\left(\sum \sin 2\theta_k\right)^2 + \left(\sum \cos 2\theta_k\right)^2} \tag{2.43}$$

$$Average\ Absolute\ Angle\ (AAA) = \frac{\sum |\theta_k|}{N} \tag{2.44}$$

$$Average\ Angle\ (AA) = \frac{\sum \theta_k}{N} \tag{2.45}$$

where θ_k is the preferred aggregate orientation with respect to the horizontal plane from -90° to +90°, and where +90° corresponds to the horizontal plan and θ_k is measured counterclockwise. Δ is the percent of vector magnitude, which varies from 0% to100%, where 0% indicates that the aggregates are randomly distributed, while a percent of 100% indicates that all of the captured aggregate particles have the same orientation. N is the number of aggregate particles in the analyzed image. The difference between average absolute angle (AAA), and average angle (AA) is that AAA gives the absolute value of the aggregates' angle without considering the sign of the angle, whereas AA takes the sign into account.

Also, Tashman et al. (2001) stated that Masad et al. (1998) used harmonic series to quantify the aggregate orientation as presented in Eq. 2.46.

$$n(\theta_i) = n_a(1 + A_2 cos^2\theta_i + 2B_2 cos\theta_i sin\theta_i - A_2 sin^2\theta_i) \tag{2.46}$$

where $n(\theta_i)$ is the aggregate orientation at a certain angle (θ_i) from the horizontal plane. The parameters n_a , A_2, and B_2 are defined according to the following equations:

$$n_a = \frac{N}{N_d} \tag{2.47}$$

$$A_2 = \frac{2}{N}\sum_{k=1}^{N} \cos(2\theta_k) \tag{2.48}$$

$$B_2 = \frac{2}{N}\sum_{k=1}^{N} \sin(2\theta_k) \tag{2.49}$$

where N is the total number of aggregate particles in the analyzed image, N_d is the number of directions considered in the harmonic series approximation. For random aggregate distribution, A_2 and B_2 are zeros, and Eq. 2.46 is always equal to n_a, which is perfect circle in the polar diagram.

Figure 2.9(a) and (b) show AAA and Δ, respectively for the aggregate particles coarser than 4.75 mm.

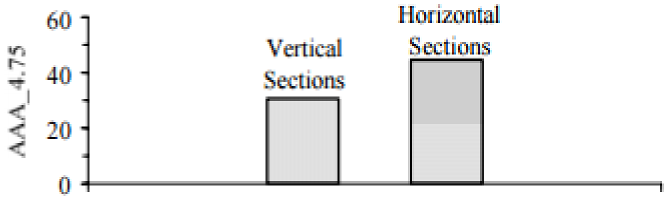

(a) Average Absolute Angle of Aggregates Orientation.

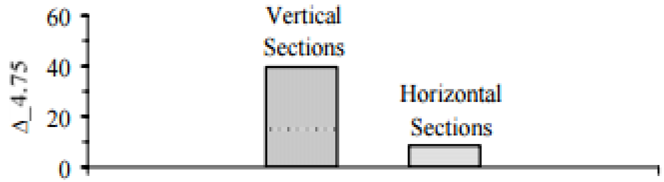

(b) Vector Magnitude of Aggregates Orientation.

Figure 2.9 (a) Average Absolute Angle of Aggregates Orientation and (b) Vector Magnitude of Aggregate Orientation (Tashman et al. 2001)

Tashman et al. (2001) stated that AAA is lower in the vertical sections than horizontal ones, and Δ is almost zero in the vertical sections. The results demonstrated that the longest axes of the aggregates have preferred orientation to the horizontal direction. Based on these findings, the researchers stated that the asphalt mixtures are anisotropic materials with respect to the compaction direction.

Moreover, the researchers compared the analysis of field cores to laboratory samples at 5% significance level (P-value). They found that the angle of gyration and the height of the sample were significant parameters in affecting the aggregate orientation (Tashman et al. 2001).

Figure 2.10 shows the polar diagram according to Eq. 2.46 for horizontal sections (Fig. 2.10 [a]) and for vertical sections (Fig. 2.10 [b]). The radius in Fig. 10 represents the number of aggregate particles that have a preferred orientation in that direction. Figure 2.10 (a) shows that the aggregate particles are randomly distributed, whereas in Fig. 2.10 (b) shows that there is a preference of the aggregate particles toward the horizontal direction.

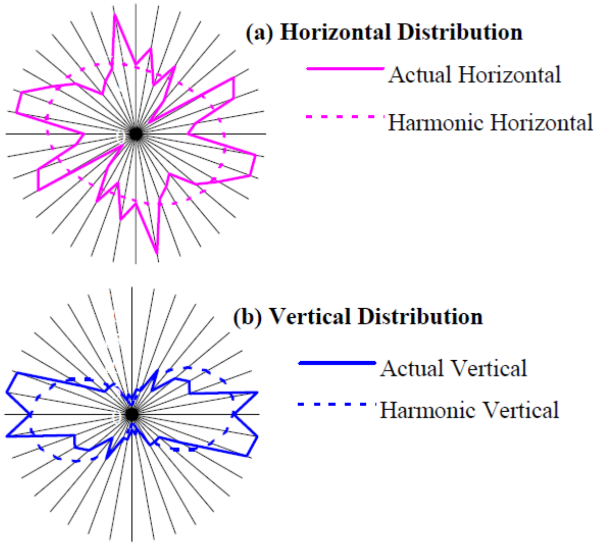

Figure 2.10 Aggregate Orientation of Vertically and Horizontally Sliced Samples in Polar Diagram (Tashman et al. 2001)

Masad et al. (2002) derived micromechanics-based models to quantify the stiffness anisotropy of asphalt mixtures. The researchers obtained the model parameters by analyzing the anisotropy of the internal structure of asphalt mixture samples. The anisotropy was quantified in terms of preferred orientation of longest axes and contact normal of aggregates.

The researchers used image analysis techniques, similar to the ones used by Tashman et al. (2001), to conduct the internal structure measurements. They found that characterizing the stiffness anisotropy based on the orientation of aggregate was simple and more effective than the other methods. Also, they quantified the stiffness anisotropy and found that the asphalt mixtures exhibit inherent anisotropy perpendicular to the direction of compaction. Moreover, they supported their conclusions by finite element analysis which showed a good agreement with the models they developed.

2.2.3 Induced Anisotropy

Mamlouk et al. (2002) performed uniaxial tension tests and compression tests under different strain rates and at a confining pressure of 20 psi. The researchers prepared asphalt mixture samples in the laboratory and cored small specimens in different directions (vertical, horizontal, and diagonal [45° from the horizontal direction]). All of the small samples had a percent air void of 4% ± 0.5%, and dimensions of 2.17 in. in diameter, and 4.33 in. in height.

Mamlouk et al. (2002) studied the effect of anisotropy on the tensile and compressive properties of asphalt mixtures including peak strength, initial modulus, and secant modulus at 90% of the peak deviator stress. The compression tests were performed on the vertically- and horizontally-cored samples at 50°C, and strain rates of 0.01 m/m/s and 0.001 m/m/s, whereas the tension tests were performed on vertically-, horizontally-, and diagonally-cored samples at 25°C, and at the same strain rates of compression tests.

Mamlouk et al. (2002) statistically compared the results of tension and compression tests using ANOVA test. Figure 2.11, and 2.12 show their findings for compression and tension tests, respectively. Based on the ANOVA analysis for both compression and tension tests, they concluded that there is no significant difference, and the influence of the anisotropy on asphalt mixtures can be disregarded.

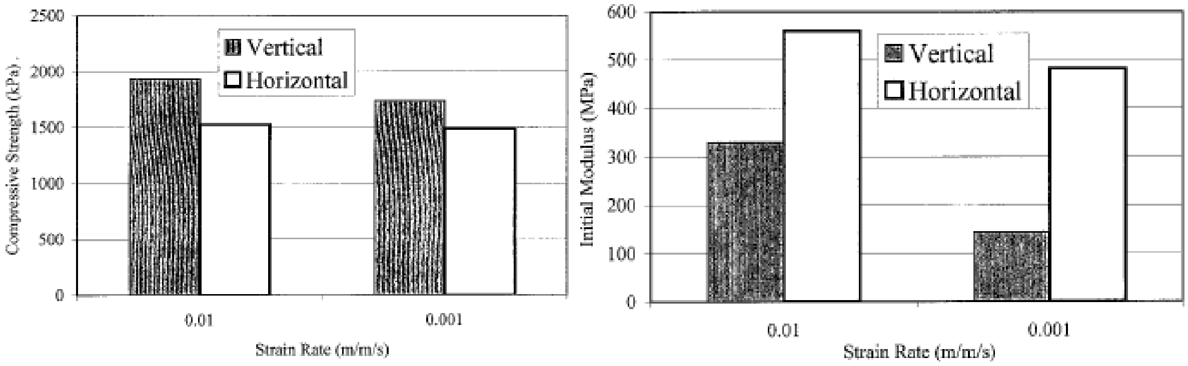

(a) Compressive strength.

(b) Initial modulus.

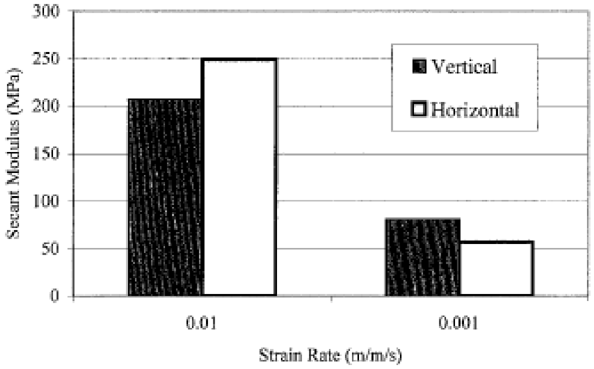

(c) Secant modulus.

Figure 2.11 (a) Compressive Strength, (b) Initial Modulus, and (c) Secant Modulus from Compression Tests (Mamlouk et al. 2002)

Wang et al. (2005) performed an experimental investigation on field cubical samples that had dimensions of 4 in. and binder content of 5.5%, and 8% air void at room temperature (25^{o}C). They performed multiple laboratory tests in specified sequence including isotropic compression (up to 25 psi on each face) and conventional triaxial extension tests. They found that the vertical stiffness is larger than the horizontal stiffness by 2 to 5 times. Therefore, they concluded that field compacted asphalt concretes are generally anisotropic materials.

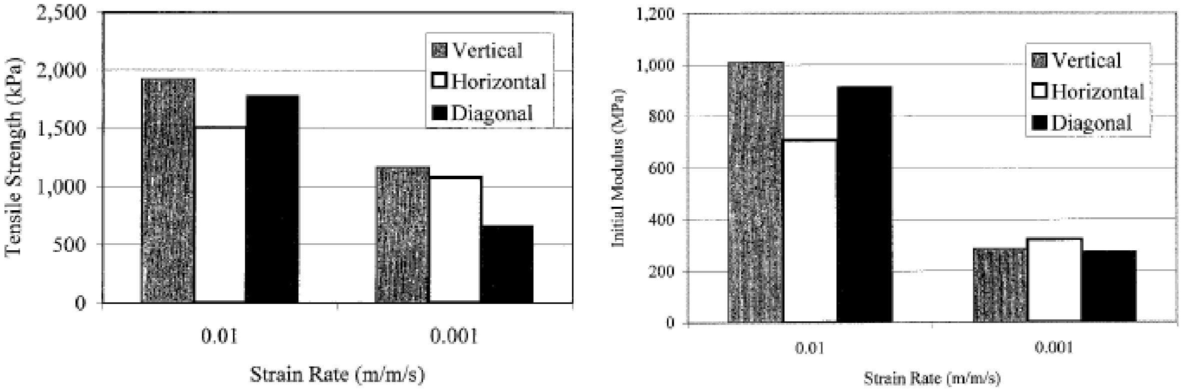

(a) Tensile strength. (b) Initial modulus.

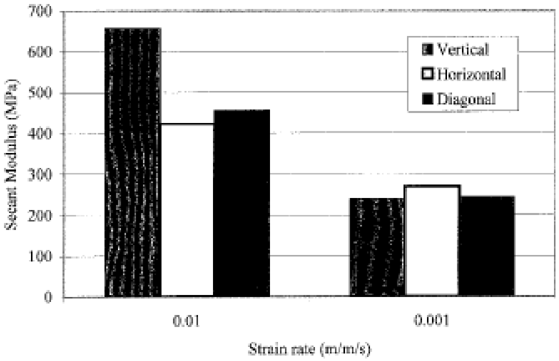

(c) Secant modulus.

Figure 2.12 (a) Tensile Strength, (b) Initial Modulus, and (c) Secant Modulus from Tension Tests (Mamlouk et al. 2002)

Underwood et al. (2005) carried out a set of experiments to evaluate the induced anisotropy of cylindrical asphalt mixture specimens on the mechanical properties. The test specimens were cored vertically and horizontally from Superpave gyratory compactor (SGC) samples. The vertically- and horizontally-cored specimens had the same dimensions of 2.95 in. in diameter and 3.54 in. in height. The percent air void was slightly different for the vertically-cored and horizontally-cored specimens. The percent of air void for vertical specimens was 3.8% ± 0.35%, and 3.2% ± 0.3% for the horizontal specimens. The study included five different tests including dynamic modulus under tension-compression test and compression-only test, uniaxial tension test, uniaxial compression test, and hydrostatic pressure test. In all of the tests (except the hydrostatic pressure test), the researchers compared the results of both vertically- and horizontally- cored specimens.

Figure 2.13 compares E* between tension-compression and compression-only tests. Underwood et al (2005) did not observe a significance difference in the dynamic modulus tests between the vertically- and horizontally-cored specimens. Therefore, they stated that the preferential aggregate orientation due to compaction has no effect on E* although Figs. 2.13(c) and 2.13(d) show that there are some differences in E* values. However, the researchers demonstrated that one of the reasons for that difference is the end plate effect because the plates were glued in the tension test whereas they were not glued in the compression test.

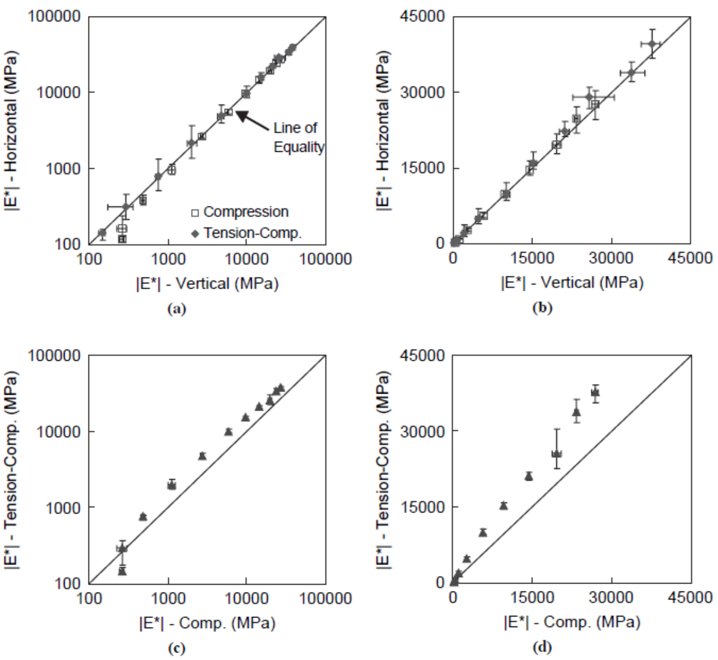

Figure 2.13 Comparison of $|E^*|$ between Horizontal and Vertical Cores in (a) log-log and (b) semi-log scales; Tension-Compression and Compression-only Methods in (c) log-log, and (d) semi-log scales (Underwood et al. 2005)

The uniaxial tension and compression tests were conducted at different strain rates and temperatures. The researchers compared the results of the mechanical tests for the vertically cored specimens against the horizontally-cored specimens. They calculated several parameters from the mechanical tests including peak stress that corresponds to the maximum induced stress on the material, axial and radial strains that correspond to the peak stress, and initial modulus which is the slope of the stress-strain curve up to 75 micro-strains. The results are presented in Fig. 2.14, and 2.15 for direct tension and compression tests, respectively.

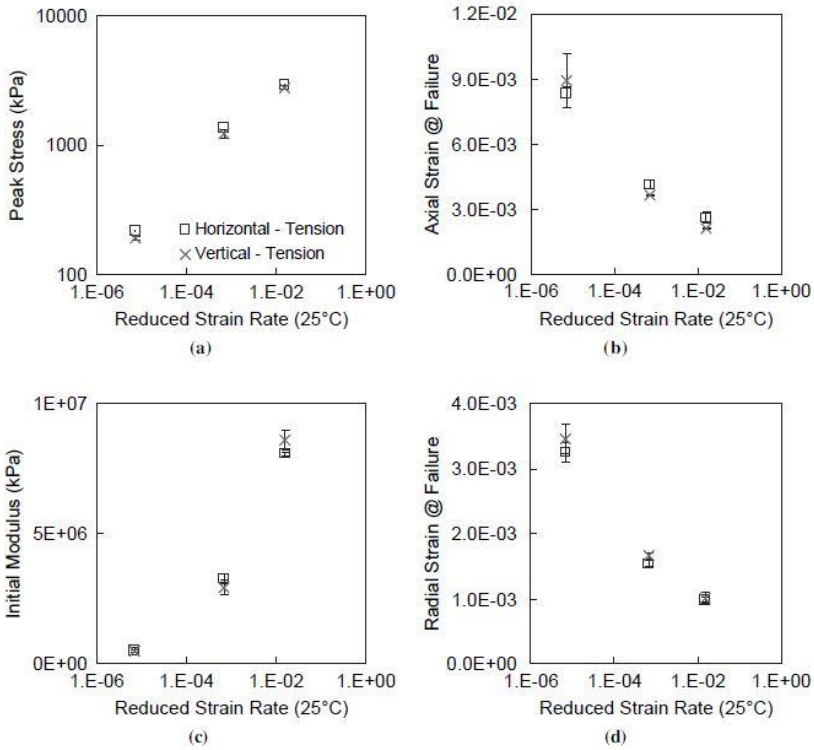

Figure 2.14 Effect of the Anisotropy in Uniaxial Tension on (a) Peak Stress, (b) Axial Strain at Failure, (c) Initial Modulus, and (d) Radial Strain at Failure (Underwood et al. 2005)

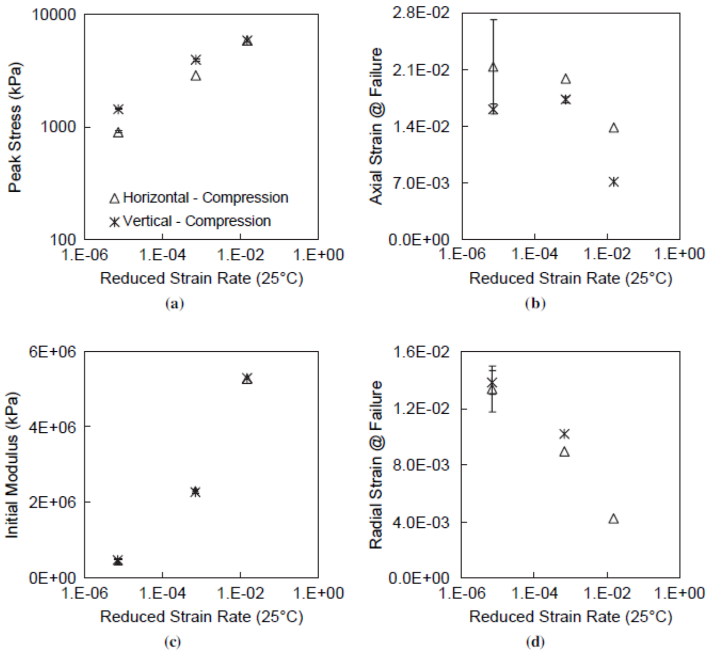

Figure 2.15 Effect of the Anisotropy in Uniaxial Compression on (a) Peak Stress, (b) Axial Strain at Failure, (c) Initial Modulus, and (d) Radial Strain at Failure (Underwood et al. 2005)

Figure 2.14 presented the uniaxial tension test results. Underwood et al. (2005) found that the direction of the cored specimens, whether they are cored vertically or horizontally, have slight variations in peak stress. However, despite the differences in the strains at failure, the researchers stated that there is no significant difference regarding the coring direction.

Figure 2.15 shows the results of the uniaxial compression test. From Fig. 2.15(a), Underwood et al. (2005) found that peak strength is higher in the vertical specimens because of the aggregate interlocking in that direction. Also, they stated that the axial strain is higher and the radial strain is lower in horizontal cores. The results demonstrated the significance of the aggregate orientation and interlock on the mechanical properties. However, the researchers reported that there is no significant difference in the initial modulus as per Fig. 2.15 (c).

The final test that was performed by Underwood et al. (2005) was to evaluate the anisotropy of asphalt mixtures under hydrostatic pressure for vertically cored samples. Also, they introduced what they called the hydrostatic anisotropy ratio, which is defined as in the following equation:

$$HAR = \frac{\varepsilon_r(t)}{\varepsilon_a(t)} \tag{2.50}$$

where HAR stands for Hydrostatic Anisotropy Ratio, and $\varepsilon_r(t)$ and $\varepsilon_a(t)$ are the radial and axial strains, respectively. The researchers applied four different hydrostatic pressure levels: 6 psi (42 kPa), 20 psi (138 kPa), 40 psi (275 kPa), and 60 psi (414 kPa). The sequence of applying the confining pressures is shown in Fig. 2.16 with a rest period in between.

According to Fig. 2.16, first Underwood et al. (2005) applied three cycles of 42 kPa under the assumption that 42 kPa is within the range of linear viscoelastic limit. Then, after each large input of confining stress, 42 kPa confining pressure was followed to quantify the effect of the applied hydrostatic pressure on the anisotropy. A total number of nine cycles were applied, and in the next discussion the applied confining pressure will be named based on the cycle number as in Fig. 2.16.

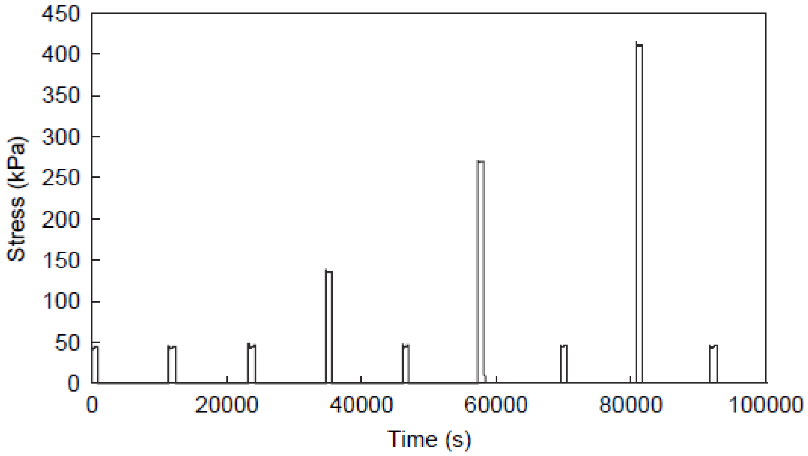

Figure 2.16 Input of Confining Pressures (Underwood et al. 2005)

Figure 2.17 shows the strains resulting from the first and last cycles of the hydrostatic pressures. Comparing Fig. 2.17 (a) and (b), one can observe that the difference between the strains is higher in the last cycle compared to the first one and the axial strain is almost the same. The researchers stated the reason for that is that the material is less stiff in the radial direction than the axial one due to aggregate interlocking in the compaction direction.

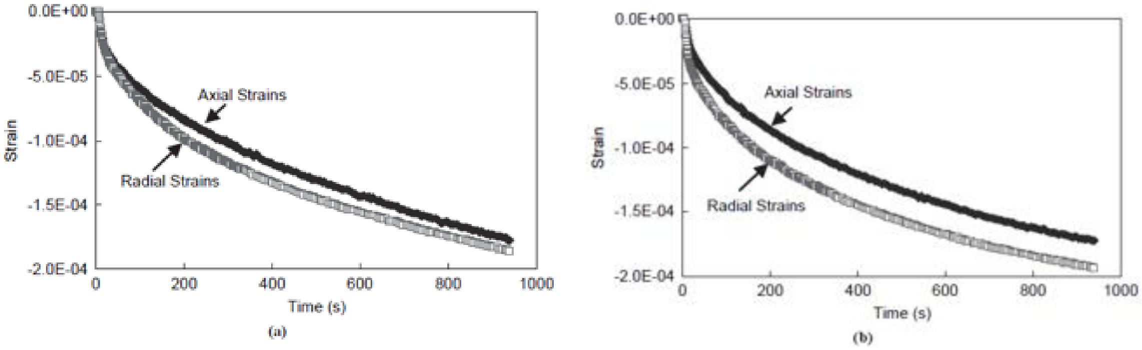

Figure 2.17 Anisotropic Response of Asphalt Concrete at Low Confining Pressure: at (a) First 42 kPa Pressure Cycle, and (b) Last 42 kPa Pressure Cycle (Underwood et al. 2005)

According to Underwood et al. (2005), the decrease in the anisotropy ratio (as in Fig. 2.18) could be due to particle reorientation until they reach an equilibrium state. All cycles, except the first one, in Fig. 2.18(b) reached an anisotropy ratio of 1.2. The researchers also demonstrated that upon releasing the hydrostatic pressure, the microstructure tends to partially return to its original random distribution.

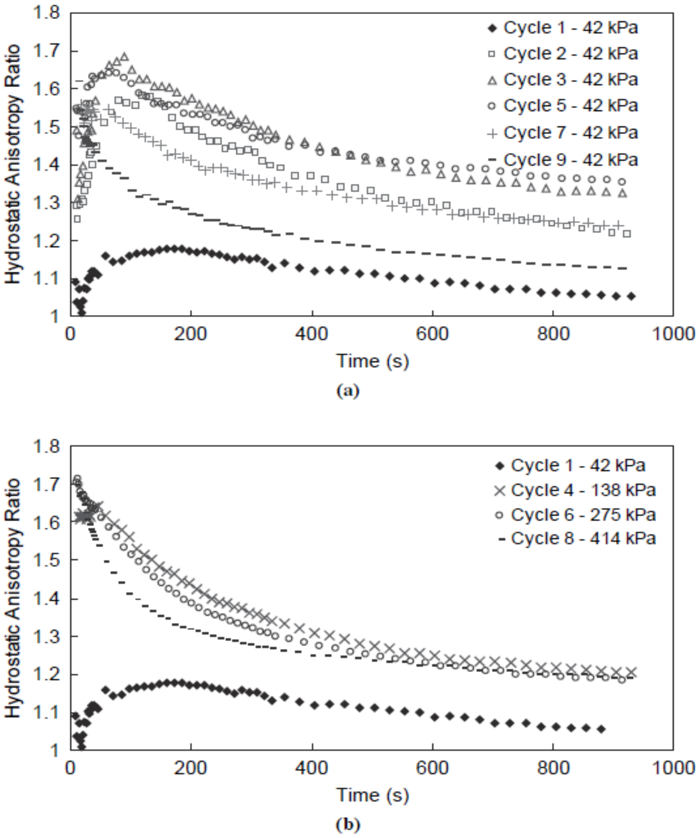

(a)

(b)

Figure 2.18 Anisotropy Ratio from Hydrostatic Tests as a Function of Time for (a) 42 kPa tests and (b) 138-, 275- and 414 kPa Tests (Underwood et al. 2005)

CHAPTER 3 – LABORATORY EXPERIMENTS

3.1 Introduction

This chapter provides information about the experimental program of this study including the design of the asphalt mixtures, test sample preparation and conditioning, and test protocol and setup. Various asphalt mixtures with different aggregate gradation and binder content were prepared and tested. The results were used to evaluate the effect of various parameters on the VPR, PR, and anisotropy of asphalt mixtures.

3.2 Asphalt Mixtures Design and Sample Preparation

A total number of five asphalt mixtures were prepared with different binder content (by weight), aggregate gradation, and Performance Grade (PG) binder. Table 3.1 presents the mixture ID, binder content, and PG of the asphalt binders. Figure 3.1. shows the aggregate gradation of the five mixtures evaluated in this study. The average percent of air void was 7% ± 0.5% for all of test samples of VPR analysis. However, for the anisotropy analysis, two different percentages of air void were considered, 7% ± 0.5% and 4% ± 0.5% to evaluate the effect of percent air void on the anisotropy.

The preparation of the cylindrical samples was conducted according to AASHTO T-312. All the mixtures were plant-mixed lab-compacted except mixtures 4 and 5 which were prepared and compacted in the laboratory. The Superpave Gyratory Compactor (SGC) was used to compact the test samples. The SGC samples were 7 in. in height and 6 in. in diameter. The SGC samples were cored and trimmed to have final dimensions of 6 in. and 4 in. in height and diameter, respectively. The test samples were checked to ensure smooth and parallel ends using a machinist’s square. Figure 3.2 shows an image of the sample preparation. The percent air void was measured to ensure that the target air void was achieved before testing.

Table 3.1: Mixture ID, Binder Content, and Performance Grade

Mixture ID	Binder Content	Performance Grade (PG)
Mix-1	7.6	PG 76-22
Mix-2	4.9	PG 64-22
Mix-3	4.6	PG 64-22
Mix-4	4.4	PG 67-22
Mix-5	4.4	PG 64-16

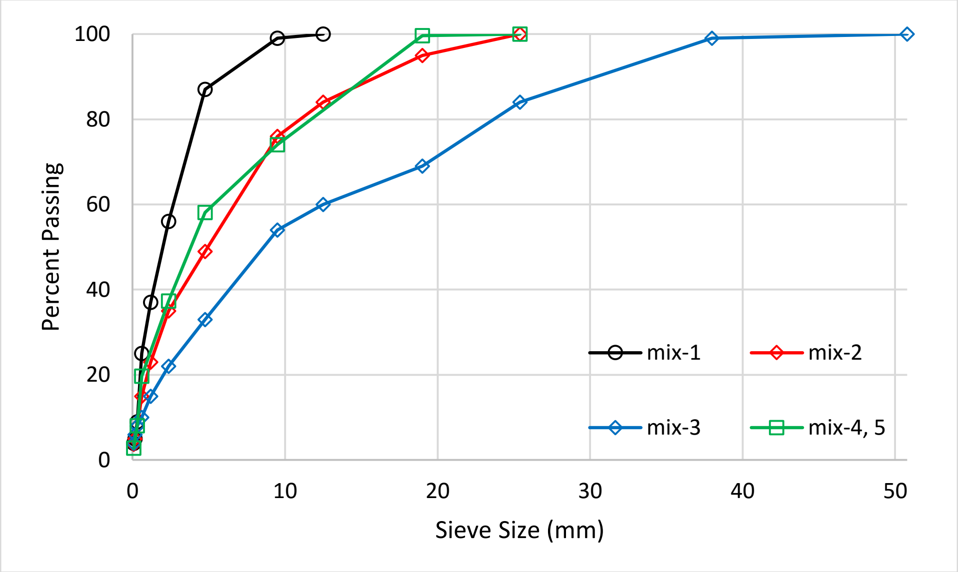

Figure 3.1 Aggregate Size Distribution of the Test Mixtures

Drying aggregates

Sieving aggregates

Mixing aggregates
with binder

Molding specimen

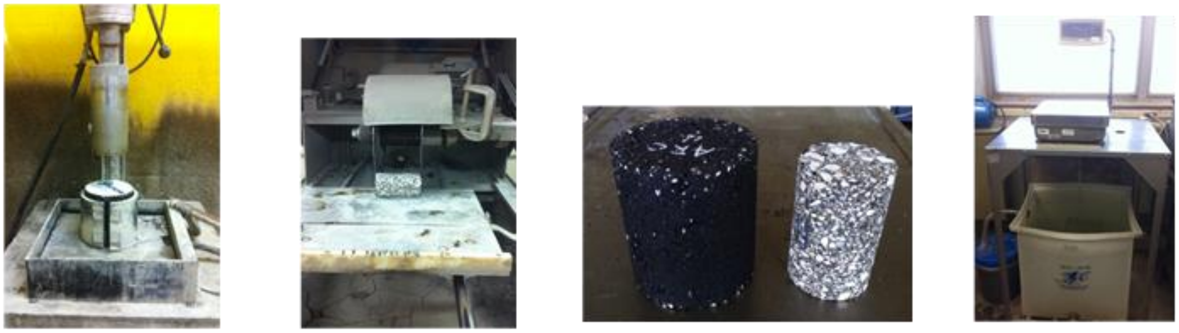

Coring specimen

Cutting specimen

Test specimen after
coring/cutting

Measuring density
Target AV±0.5%

Figure 3.2 Steps of Specimen Preparation

3.3 Tests Setup

A set of Uniaxial Constant Strain Rate (UCSR) tests in tension and compression at different conditions were conducted. A Mechanical Testing Machine (MTS) was used to load the specimens until failure. The researchers recorded the load, time, and radial and axial deformations during loading. Three axial Linear Variable Differential Transformers (LVDTs) were mounted on the sample at 120^{o} apart with a gauge length of 4 inches to record the vertical deformation. Figure 3.3 shows a schematic view of the setup with the vertical LVDTs.

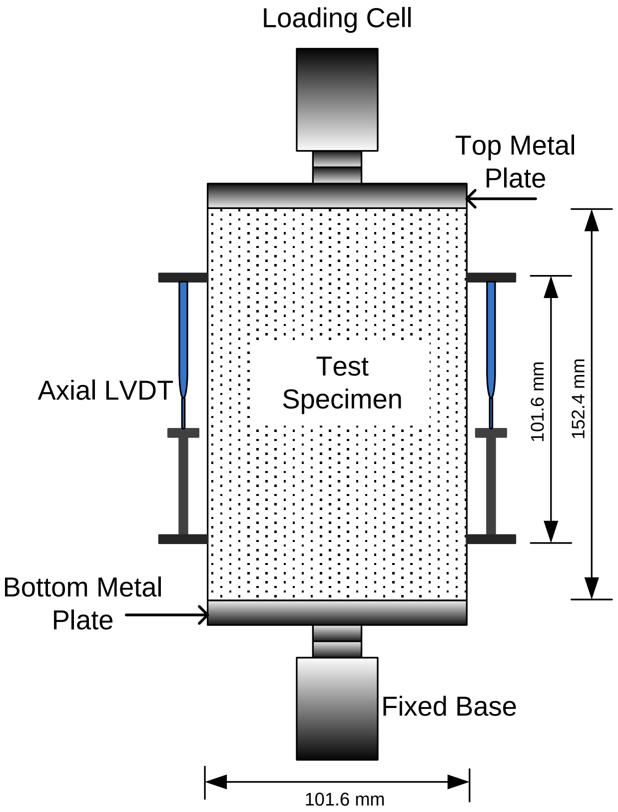

Figure 3.3 Schematic View of the Mounted Vertical LVDTs

The researchers used a circumferential LVDT to measure the radial deformation in tension tests. The circumferential LVDT was placed at the middle of the sample as in Fig. 3.4, while the researchers used three horizontal (through-the-wall) LVDTs to measure radial deformation in compression tests. The horizontal LVDTs were placed at 120^o around the middle of the sample. Figure 3.5 shows the test set-up for the compression test. Also, for the compression test, the specimens were enclosed in rubber membrane and the studs for the LVDTs were glued directly on the specimen.

Figure 3.4 Test Setup for the Tension Test

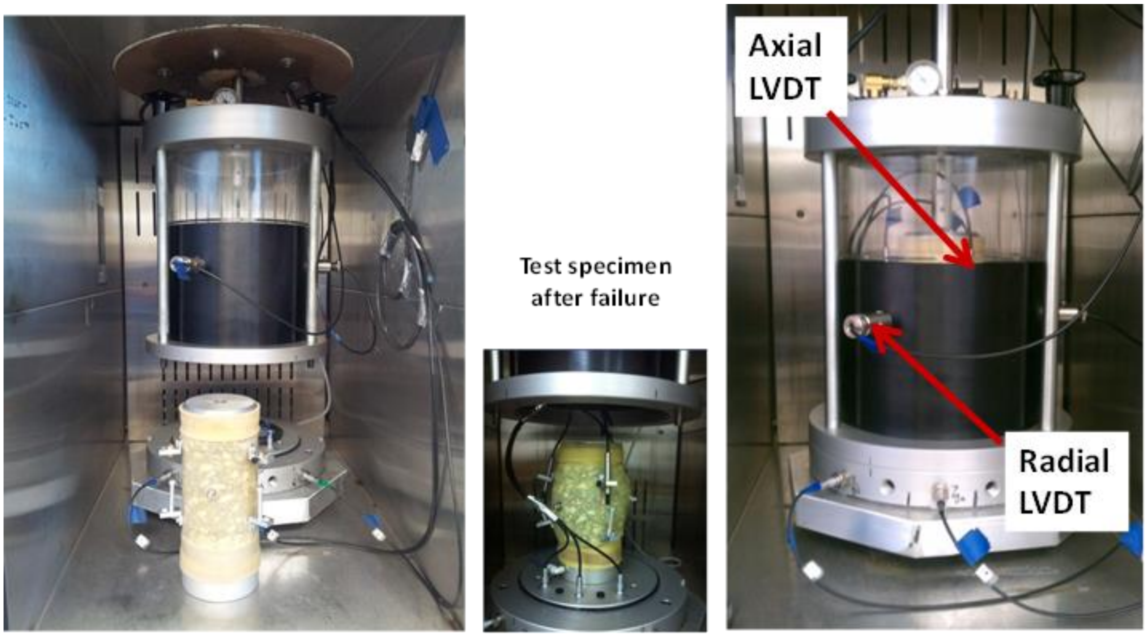

Figure 3.5 Test Setup for the Compression Test

3.4 Testing Matrix

The laboratory testing conducted in this study followed a proposed standard procedure titled "Calibration of the Pavement Analysis Using Nonlinear Damage Approach (PANDA) Constitutive Relationships" which is used to characterize various properties of asphalt mixtures (Darabi et al. 2015). Table 3.2 presents the testing matrix conducted to evaluate the VPR in this study. The table presents various applied constant strain rates, temperatures, aging, and moisture conditions. At least two replicates or samples were tested at each condition (S1 and S2). This testing matrix includes two loading modes (tension and compression), four different asphalt mixtures (Mix-1, Mix-2, Mix-3, and Mix-5), three different temperatures (5°C, 19°C in tension and 55°C in compression), various strain rates in tension, different confining pressure in compression (0 psi, 10 psi, and 20 psi), and different aging levels (0, 3, and 6 months). In addition, some specimens were tested in dry and wet conditions.

Table 3.3 presents the testing matrix performed to study and quantify the anisotropy of asphalt mixtures. The test involved the application of hydrostatic pressure for two hours. The testing matrix includes four different asphalt mixtures (Mix-1, Mix-2, Mix-3, and Mix-4), three different temperatures (19°C, 40°C, and 55°C), two levels of aging (0 and 6 months), two percentages of air voids (4% and 7%), and two confining pressures (10 psi and 20 psi).

Table 3.2 The Testing Matrix of the VPR

Mixture ID	Number of Specimens	Temperature (°C)	Strain Rate (1/sec)	Moisture Conditioning	Aging Conditioning	Confining Pressure (psi)	Test Type
Mix-1, 2, and 3	6	5	5.0E-5	0	0	0	**UCSR Tension Test**
			1.0E-5				
			5.0E-6				
Mix-5	6	5	5.0E-5	0	0	0	
			1.0E-5				
			5.0E-6				
	4	19	1.0E-4	0	0	0	
			5.0E-4				
	6	5	1.0E-5	70-80%-12Hr	0	0	
				70-80%-24Hr			
				50-60%-24Hr			
	4	19	1.0E-4	70-80%-12Hr	0	0	
				70-80%-24Hr			
	4	19	1.0E-4	0	3 Months	0	
					6 Months		
	6	55	1.0E-3	0	0	0, 10, 20	**UCSR Compression Test**

Table 3.3 The Testing Matrix of Asphalt Anisotropy

Mix- ID	Number of specimen	Temperature (°C)	Aging Conditioning (months)	% of air void	Confining Pressure (psi)	Test Type
Mix-1, 2, and 3	6	55	0	7	20	Hydrostatic
Mix-4	4	19	0	7	10, 20	
	4	40				
	4	55				
	2	40	0	4	20	
	2		0	7		

3.5 Sample Conditioning

3.5.1 Temperature Control

Since the mechanical properties of asphalt mixtures are sensitive to the change in temperature, an environmental chamber was used to control the temperature of the test specimens at the desired temperatures. Dummy samples were placed in the environmental chamber to ensure that the temperature of the specimens reached the target temperature before testing. Also, the chamber was big enough to accommodate the triaxial cell that was used to apply the confining pressure. Figure 3.6 shows the environmental chamber and the MTS system used in this study.

Figure 3.6 the MTS with an Environmental Chamber at the Texas A&M Transportation Institute

3.5.2 Aging Conditioning

The test specimens were kept in an environmental room at 60°C for 3 and 6 months. Conditioning the test specimens at this temperature simulate and accelerate many years of field aging (Glover et al. 2005). Figure 3.7 shows a visual comparison between aged and non-aged samples, where it is noticeable that the aged samples are relatively darker due to binder flushing on the surface and absorbed binder into the aggregates.

(a) Non-aged (b) 3 months aging (c) 6 months aging.

Figure 3.7 Aged and Non-Aged Specimens

3.5.3 Moisture Conditioning

The test specimens were moisture-conditioned following the AASHTO T-283-07 procedure (AASHTO 2007). A vacuum pressure of 3.38 kPa was applied until the target saturation level was achieved. In this study, two different saturation levels were considered; 70% to 80 % and 50% to 60% as given in Table 3.2. Then the test specimens were submerged in a water bath at 60^{o}C for 12 hours or 24 hours.

3.5.4 Confinement Level

The researchers used a triaxial cell to apply confining pressure (air) in the compression test. The test samples were placed inside the cell and a confining pressure was applied until the target level was achieved. The confining pressure was applied for two hours, this was found to be sufficient time for the bulk creep to take place and terminal values of axial and radial deformations achieved. Figures 3.5 and 3.8 show the triaxial cell inside the environmental chamber and a schematic view of the triaxial cell, respectively.

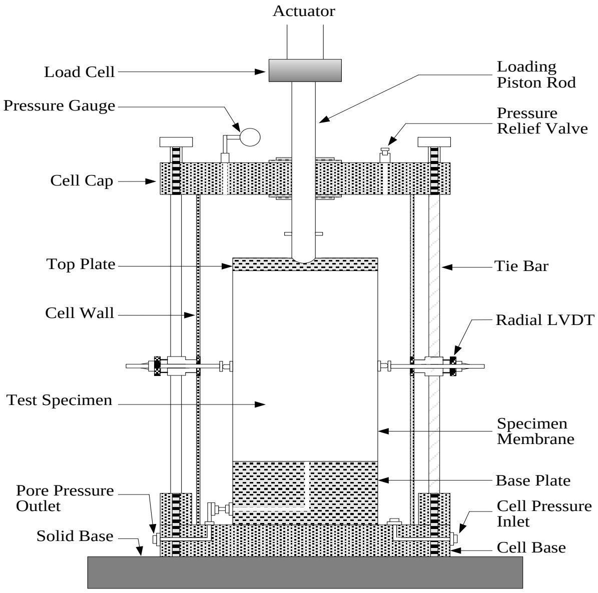

Figure 3.8 Schematic View of Typical Triaxial Cell with through-the-wall Radial LVDTs (Darabi et al. 2015)

CHAPTER – 4 ANALYSIS OF VISCOELASTIC POISSON'S RATIO OF ASPHALT MIXTURES

4.1 Introduction

4.1.1 Derivation of VPR of Asphalt Mixtures

Chou and Pagano (1967) demonstrated that for elastic materials, the derivation of the VPR can be obtained by considering the general elastic constitutive equation for an isotropic material in terms of the Lamé constants (λ and G) as given in Eq. 4.1.

$$\sigma_{ij} = \lambda\varepsilon\delta_{ij} + 2\mathrm{G}\varepsilon_{ij} \tag{4.1}$$

Rearranging Eq. 4.1 yields

$$\varepsilon_{ij} = \frac{1}{2G}\left(\sigma_{ij} - \lambda\delta_{ij}\frac{\sigma_{kk}}{3\lambda+2\mathrm{G}}\right) \tag{4.2}$$

where

$$\sigma_{kk} = 3\lambda\varepsilon + 2\mathrm{G}\varepsilon_{kk} = (3\lambda + 2\mathrm{G})\varepsilon \tag{4.3}$$

Defining PR (ν^*), and Young's modulus (E) as

$$\nu^* = \frac{\lambda}{2(\lambda+\mathrm{G})} \tag{4.4}$$

$$E = \frac{\mathrm{G}(3\lambda+2\mathrm{G})}{\lambda+\mathrm{G}} \tag{4.5}$$

PR and E are then substituted into Eq. 4.2 yielding

$$\varepsilon_{ij} = \frac{1+\nu^*}{E}\sigma_{ij} - \frac{\nu^*}{\mathrm{E}}\delta_{ij}\sigma_{kk} \tag{4.6}$$

For viscoelastic materials, Eq. 4.6 may be written as

$$\varepsilon_{ij}(t) = \int_0^t \frac{\partial}{\partial t'}\left[\int_0^{t'} J(t'-\tau)\frac{\partial \sigma_{ij}(\tau)}{\partial \tau}d\tau\right][1+\nu^*(t-t')]dt' - \int_0^t \frac{\partial}{\partial t'}\left[\int_0^{t'} J(t'-\tau)\frac{\partial \sigma_{kk}(\tau)\delta_{ij}}{\partial \tau}d\tau\right][\nu^*(t-t')]dt' \tag{4.7}$$

where *J(t)* is the uniaxial viscoelastic compliance, and ν^**(t)* is viscoelastic material property (Kassem et al. 2013). In case of uniaxial loading, $\sigma_{11} \neq 0$ and $\sigma_{ij} = 0$, $\varepsilon_{11}(t)$ and $\varepsilon_{22}(t)$ can be calculated as

$$\varepsilon_{11}(t) = \int_0^t J\,(t-t')\,\frac{\partial \sigma_{11}(t')}{\partial t'}dt' \tag{4.8}$$

$$\varepsilon_{22}(t) = -\int_0^t \frac{\partial}{\partial t'}\int_0^{t'}\left[J(t'-\tau)\,\frac{\partial \sigma_{11}(\tau)}{\partial \tau}d\tau\right] \times \nu^*(t-t')dt' \tag{4.9}$$

Then, the strain ratio (PR) is

$$\nu(t) = -\frac{\varepsilon_{22}(t)}{\varepsilon_{11}(t)} = \frac{\int_0^t \frac{\partial}{\partial t'}\int_0^{t'}\left[J(t'-\tau)\frac{\partial \sigma_{11}(\tau)}{\partial \tau}d\tau'\right]\times \nu^*(t-t')dt'}{\int_0^t J(t-t')\frac{\partial \sigma_{11}(t')}{\partial t'}dt'} \tag{4.10}$$

Taking LT of Eq. 4.8 and 4.9 yields

$$\bar{\varepsilon}_{11}(s) = s\bar{J}(s)\bar{\sigma}_{11}(s) \tag{4.11}$$

$$\bar{\varepsilon}_{22}(s) = -s^2\bar{J}(s)\bar{\sigma}_{11}(s)\bar{\nu}^*(s) \tag{4.12}$$

Then, solving Eq. 4.11 and 4.12 for $\bar{\nu}^*(s)$ (which is VPR in LT):

$$\bar{\nu}^*(s) = -\frac{1}{s} * \frac{\bar{\varepsilon}_{22}(s)}{\bar{\varepsilon}_{11}(s)} \tag{4.13}$$

Inverting Eq. 4.13 to time domain as

$$\nu^*(t)=\mathrm{L}^{-1}\left[\frac{1}{s}*\frac{\bar{\varepsilon}_{22}(s)}{\bar{\varepsilon}_{11}(s)}\right] \tag{4.14}$$

Equation 4.10 shows that v(t) (PR) is not a material property and dependent on the stress history of the material whereas VPR $[\nu^*(t)]$ (Eq. 4.14) is independent on the stress history and thus a material properly.

Kassem et al. (2013) concluded that the percent error between calculating PR according to Eq. 2.2 and VPR according to Eq. 4.14 varies from 10% to 30% in the uniaxial tension test. The reader is referred to Kassem et al. (2013) for more information of their experiments.

In case of uniaxial loading under confining pressure, where $\sigma_{11} \neq 0$ and $\sigma_{ij} \neq 0$, Eq. 4.14 is not valid for calculating VPR. Instead, the VPR is calculated as a function of bulk and shear moduli as follows (Zachary and Lange 2007):

$$\sigma_m(t) = \frac{1}{3}[\sigma_{zz}(t) + 2\sigma_{rr}(t)] \tag{4.15}$$

$$\varepsilon(t) = [\varepsilon_{zz}(t) + 2\varepsilon_{rr}(t)] \tag{4.16}$$

where $\sigma_m(t)$ is the mean stress, $\sigma_{zz}(t)$is the axial stress, $\sigma_{rr}(t)$ is the applied confining pressure, $\varepsilon(t)$ is the volumetric strain, $\varepsilon_{zz}(t)$ is the axial strain, and $\varepsilon_{rr}(t)$ is the radial strain. The bulk modulus in the LT $[\overline{K}(s)]$ can be calculated as

$$\overline{K}(s) = \frac{1}{s}\frac{\overline{\sigma}_m(s)}{\overline{\varepsilon}(s)} \tag{4.17}$$

where $\overline{\sigma}_m(s)$, and $\overline{\varepsilon}(s)$ are the LT of the mean stress and volumetric strain, respectively. Zachary and Lange (2007) pointed out that Kachanov (1974) found the deviatroic stress-strain relationship by defining the effective stress [$\tau_e(t)$], and the effective strain [$\gamma_e(t)$] and they can be calculated directly as

$$\tau_e(t) = \frac{1}{\sqrt{3}}|\sigma_{zz}(t) - \sigma_{rr}(t)| \tag{4.18}$$

$$\gamma_e(t) = \frac{2}{\sqrt{3}}|\varepsilon_{zz}(t) - \varepsilon_{rr}(t)| \tag{4.19}$$

then the shear modulus in LT $\left[\overline{G}(s)\right]$ can be found according to Eq. 4.20:

$$\overline{G}(s) = \frac{1}{s}\frac{\bar{\tau}_e(s)}{\bar{\gamma}_e(s)} \tag{4.20}$$

where $\bar{\tau}_e(s)$, and $\bar{\gamma}_e(s)$ are the LT of the effective stress and strain, respectively. Once the bulk, and shear moduli are determined, $\nu^*(t)$ can be determined according to Eq.4.24. The VPR [$\nu^*(t)$] can be calculated by taking LT of Eq. 4.2 as given in Eq. 4.2.

$$\bar{\nu}^*(s) = \frac{1}{s} * \frac{3\overline{K}(s) - 2\overline{G}(s)}{2\left[3\bar{k}(s) + \overline{G}(s)\right]} \tag{4.21}$$

$$\nu^*(t) = \mathrm{L}^{-1}\left[\frac{1}{s} * \frac{3\overline{K}(s) - 2\overline{G}(s)}{2\left[3\bar{k}(s) + \overline{G}(s)\right]}\right] \tag{4.22}$$

4.2 Calculation of the VPR

The author considered the data up to an axial strain level of 200 με. Studies showed that this strain level is too low to cause damage in the asphalt mixtures (Kassem et al. 2013). Equation 4.14 was used to determine VPR from the UCSR test in tension and compression where the confining pressure is zero, while Eq. 4.22 was used to determine the VPR for the UCSR in compression subjected to confining pressure.

The author followed the steps below to determine the VPR using Eq. 4.14:

- Calculate the axial and radial strains; $\varepsilon_{11}(t)$ and $\varepsilon_{22}(t)$, respectively.
- Fit power functions to the resulted strains.
- Take LT of the $\varepsilon_{11}(t)$ and $\varepsilon_{22}(t)$ to obtain $\bar{\varepsilon}_{11}(s)$and $\bar{\varepsilon}_{22}(s)$.
- Substitute $\bar{\varepsilon}_{11}(s)$and $\bar{\varepsilon}_{22}(s)$ into Eq. 4.13 which results in $\bar{\nu}^{*}(s)$; and
- Invert $\bar{\nu}^{*}(s)$ into time domain (Eq. 4.14).

Figure 4.1 shows an example of the calculated axial and radial strains from UCSR test in tension. The power function was found to fit the strains accurately with r-squared of 0.99. Figure 4.2 shows a comparison between the VPR calculated from Eq. 4.14 and PR calculated inaccurately as the negative ratio of radial to axial strains.

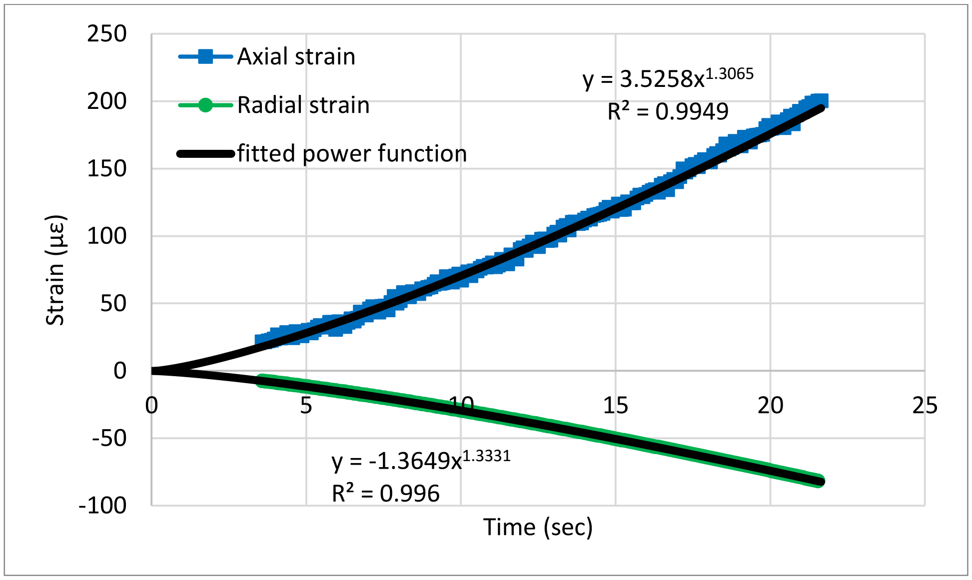

Figure 4.1 Average Axial and Radial Strains from UCSR Tension Test

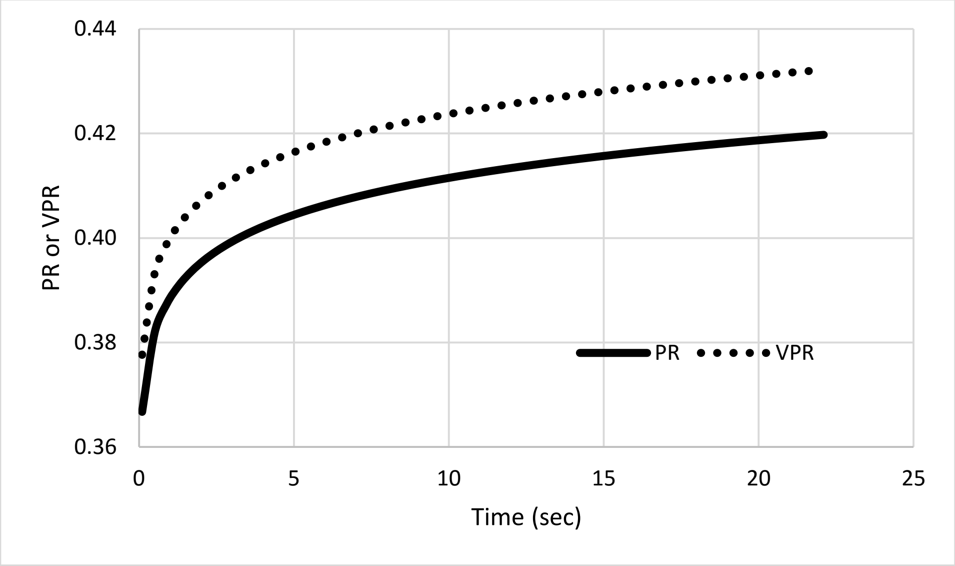

Figure 4.2 PR versus VPR from the Direct Tension Test

In addition, the shear and bulk moduli of test samples subjected to unconfined uniaxial loading (tension or compression) were calculated as follows:

- Calculate the applied stress by dividing the applied force over the cross sectional area.
- Fit functions to the applied stress and axial strain versus time.
- Take LT of the stress and the axial strain functions.
- Calculate $\overline{E}(s)$ as in Eq. (2.38).
- Calculate $\overline{\mathrm{v}}(\mathrm{s})$ (according to the steps of calculating VPR using Eq. 4.14).
- Substitute $\overline{\mathrm{E}}(\mathrm{s})$ and $\overline{\mathrm{v}}(\mathrm{s})$ into Eq. 2.39 to calculate the shear modulus in LT domain.
- Substitute $\overline{\mathrm{E}}(\mathrm{s})$ and $\overline{\mathrm{v}}(\mathrm{s})$ into Eq. 2.40 to find the bulk modulus in LT domain, and
- Invert $\overline{\mathrm{G}}(\mathrm{s})$ and $\overline{\mathrm{K}}(\mathrm{s})$ to time domain to get shear modulus [G*(t)] and bulk modulus [K*(t)] as a function of time.

The author followed the steps below to calculate the VPR of test samples subjected to confined compressive loading:

- Calculate the vertical and radial strains from the LVDTs as in Fig. 4.3.

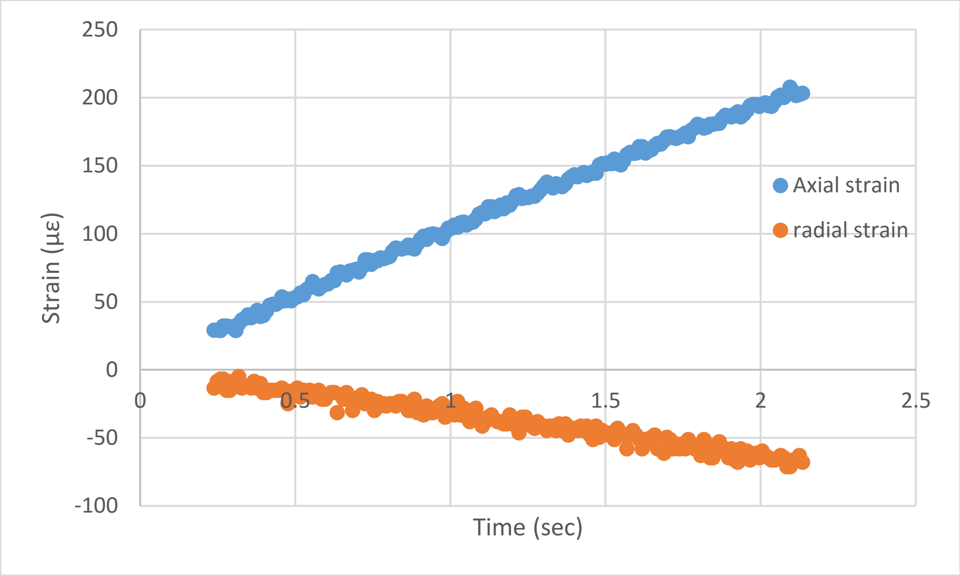

Figure 4.3 The Axial and Radial Strains with Time

- Calculate the mean stress, and volumetric strain according to Eq. 4.15 and 4.16, respectively. Figure 4.4 shows an example of the applied axial stress [$\sigma_{zz}(t)$] and radial stress [$\sigma_{rr}(t)$]. Then, Figs. 4.5 and 4.6 show the mean stress [$\sigma_m(t)$] and volumetric strain [$\varepsilon(t)$], respectively.

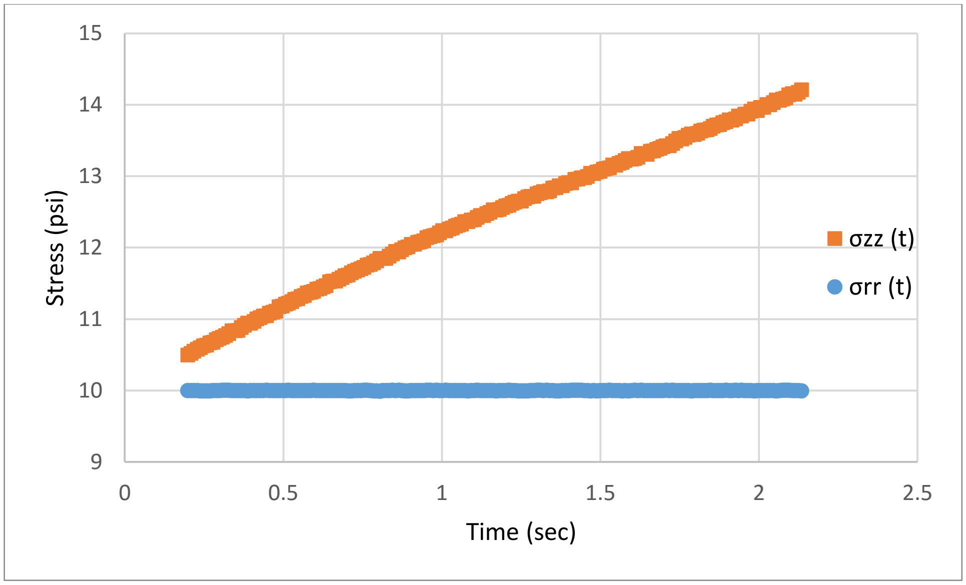

Figure 4.4 The Applied Confining Pressure and Axial Stress on the Axial Direction

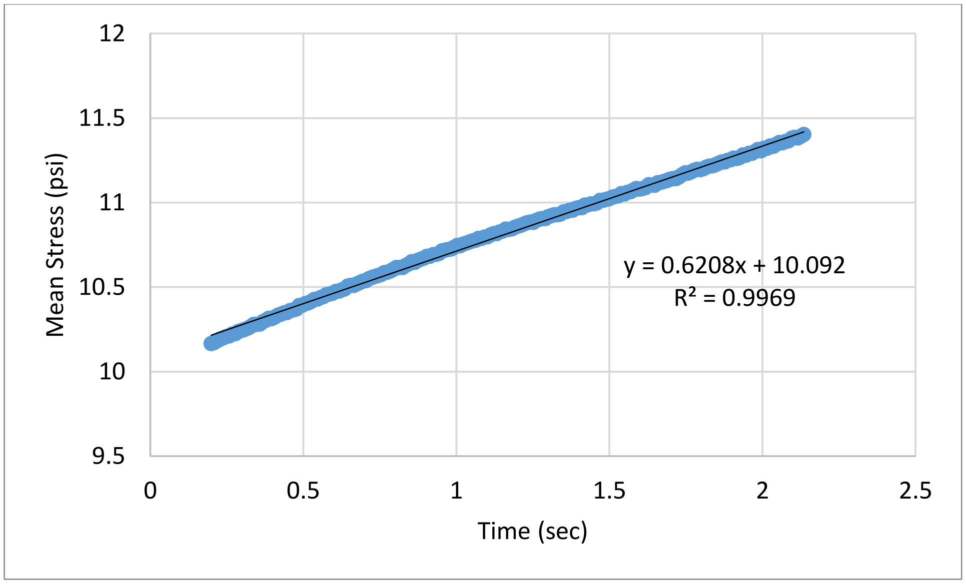

Figure 4.5 Mean Stress with the Fitted Linear Function

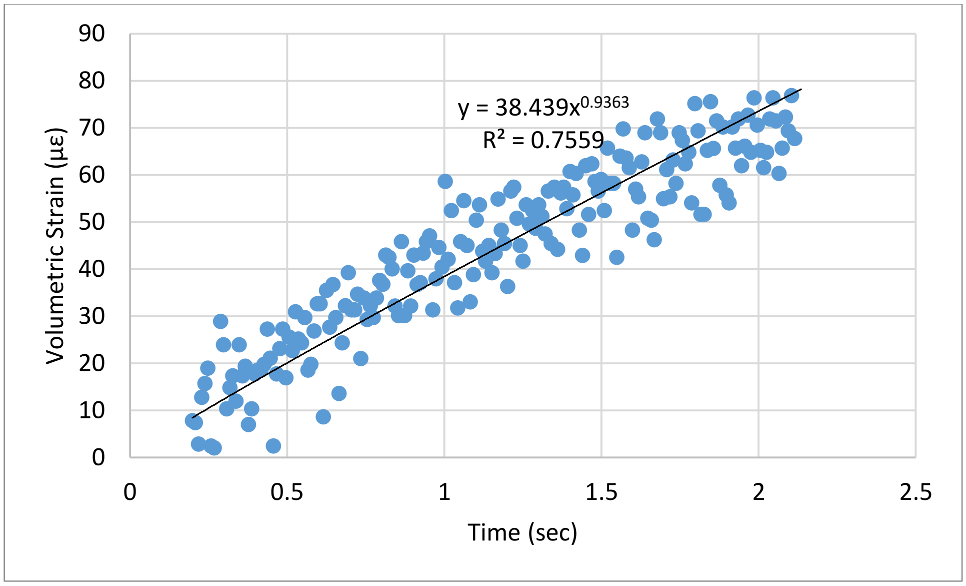

Figure 4.6 Volumetric Strain with the Fitted Power Function

- Calculate the effective stress using Eq. 4.18 and the effective strain using Eq. 4.19 as shown in Fig 4.7 and 4.8, respectively.

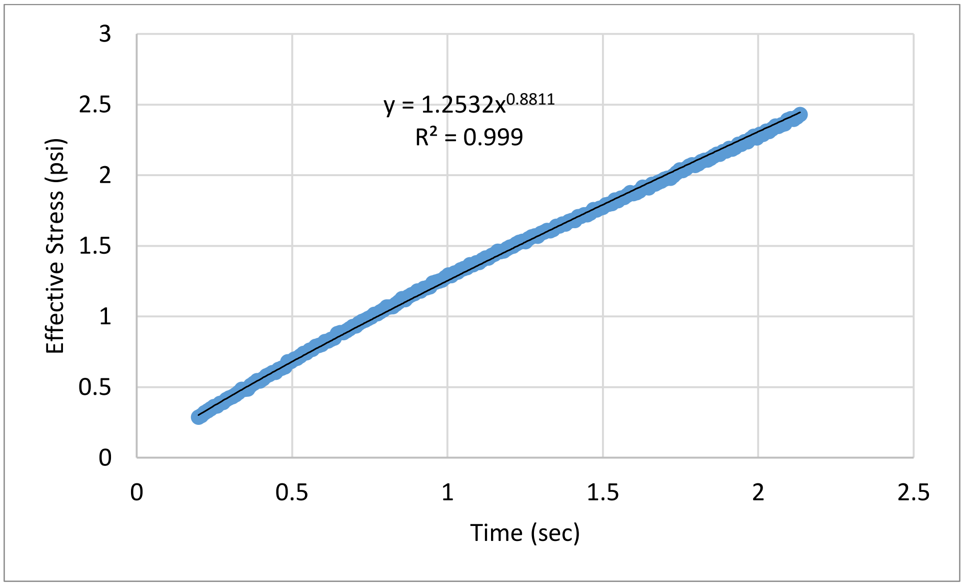

Figure 4.7 The Resulted Effective Stress with the Fitted Power Function

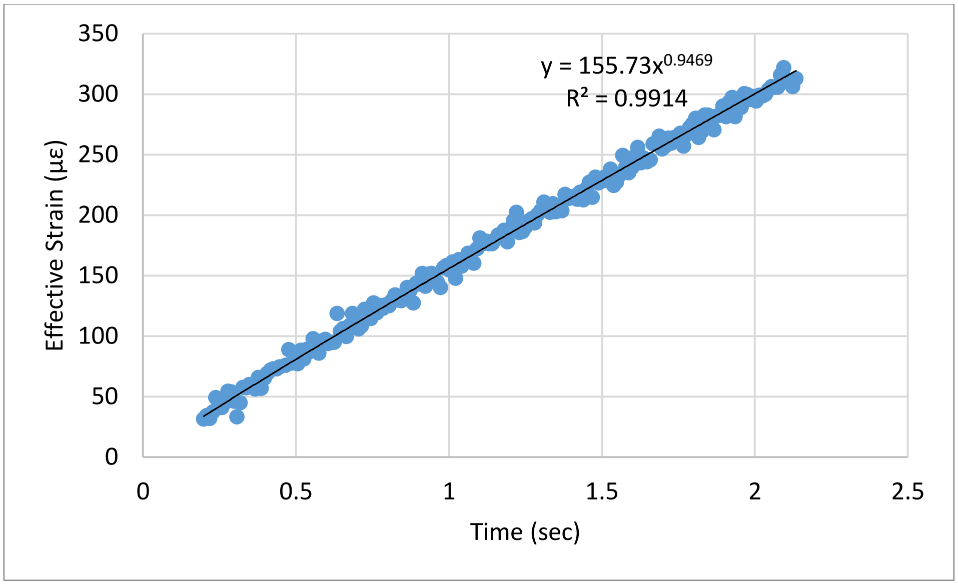

Figure 4.8 The Resulted Effective Strain with the Fitted Power Function

- Fit functions to the mean stress, volumetric strain, effective stress, and effective strain as presented in Figs. 4.5 through 4.8.
- Take LT of the fitted above functions.
- Calculate the bulk (Eq. 4.17) and shear (Eq. 4.20) moduli.
- Calculate $\nu^*(s)$ using Eq. 4.21
- Invert $\nu^*(s)$ to time domain to obtain $\nu^*(t)$ using Eq. 4.22 as shown in Fig. 4.9.

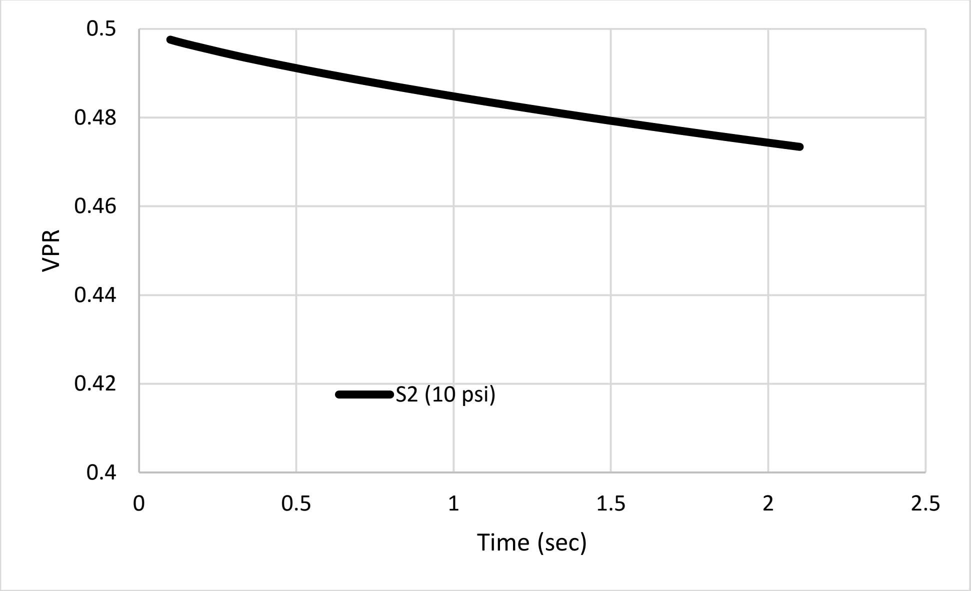

Figure 4.9 VPR under 10 psi Hydrostatic Pressure and 55ºC

Figure 4.9 shows that VPR is decreasing with time for the asphalt mixture under uniaxial compressive loading and confining pressure unlike the unconfined uniaxial tensile or compressive loading. Figure 4.10 shows the bulk and shear moduli after inverting them to time domain from Eq. 4.17 and 4.20, respectively. According to Fig. 4.10, the shear modulus relaxes slower than the bulk modulus which explains why VPR decreases with time.

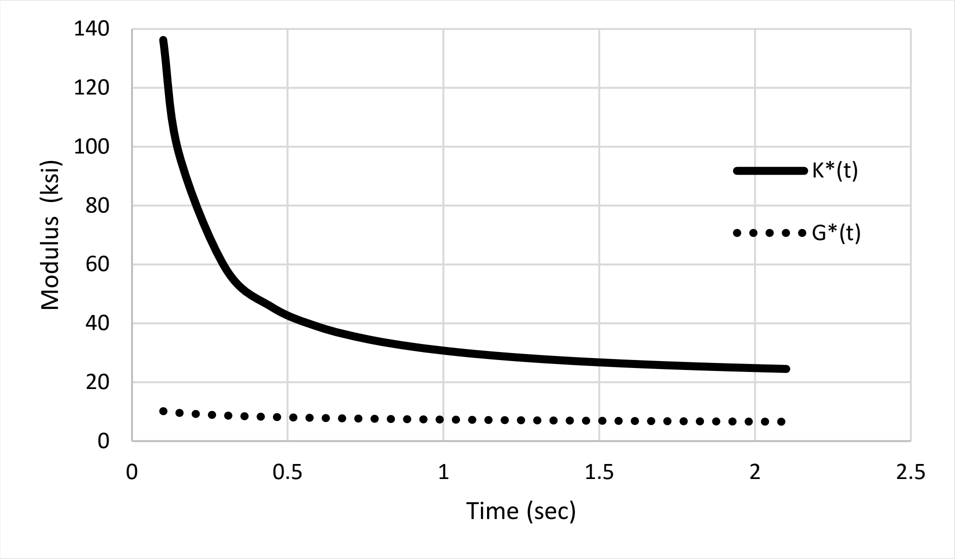

Figure 4.10 Bulk and Shear Moduli at 55ºC

4.3 Effect of Different Uniaxial Tension Loading Rates on VPR

In this section, the effect of loading rate on VPR was investigated. Several strain rates were examined as presented in Table 3.2. Figure 4.11 shows an example of measured stress at different loading rates up to 200με of the axial strain. As expected, the higher applied strain rate, the higher the measured stress due to the viscoelastic nature of the asphalt mixtures.

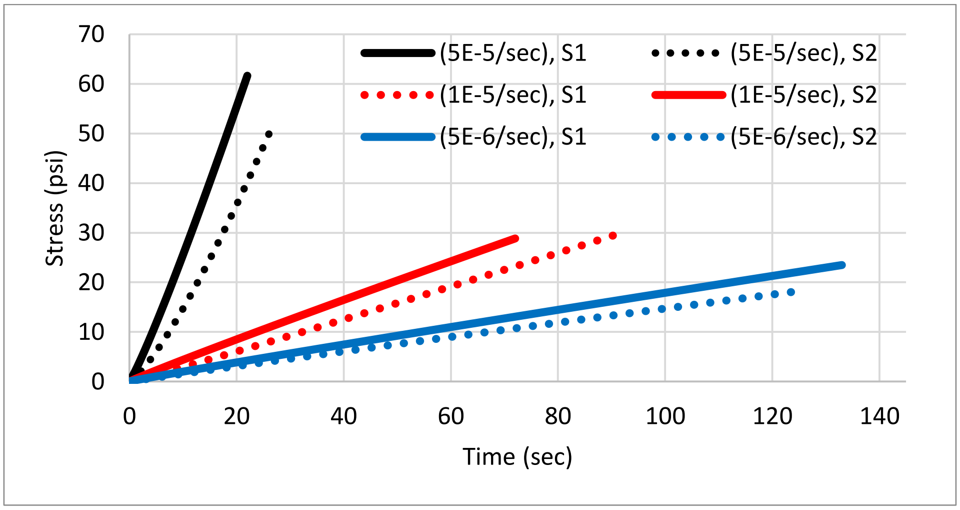

Figure 4.11 Stresses of Different UCSR Tension Test

Figures 4.12 through 4.16 show the VPR versus time at different loading rates and temperatures for various asphalt mixture subjected to unconfined tensile loading. The results showed that the VPR increased with the time, regardless of the strain rate or mixture design. These results are in good agreement with the findings of previous studies by Lee and Kim (2009) and Kassem et al. (2013). The increase of the VPR with time indicates that the shear relaxation is faster than dilatational relaxation. The results demonstrated that there was no clear trend between the applied strain rate and the measured VPR at the evaluated temperature and the range of strain rates for all test samples. It was found that the variability between the replicates overcome that relationship in most cases.

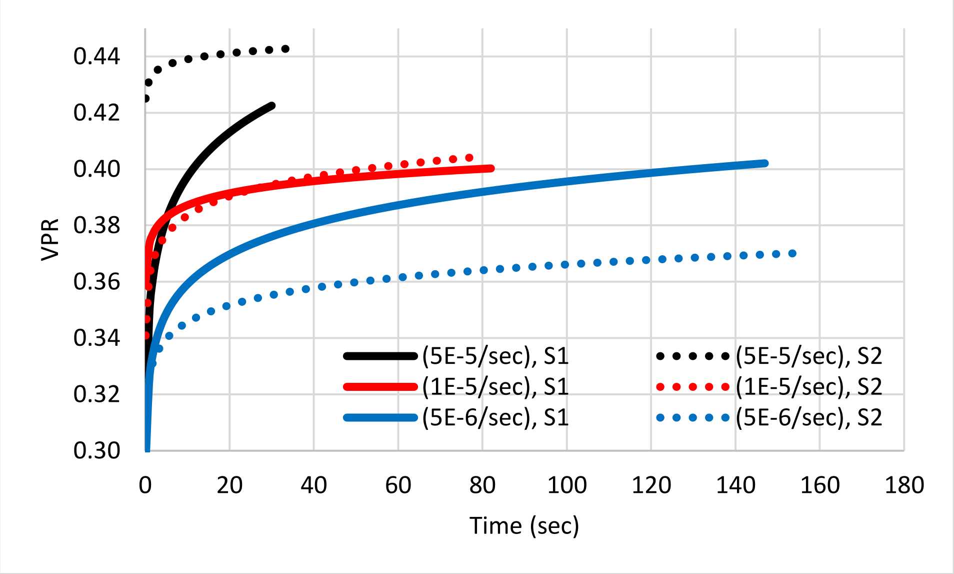

Figure 4.12 Effect of Different Tensile UCSR on Mix-1 at 5^{o}C

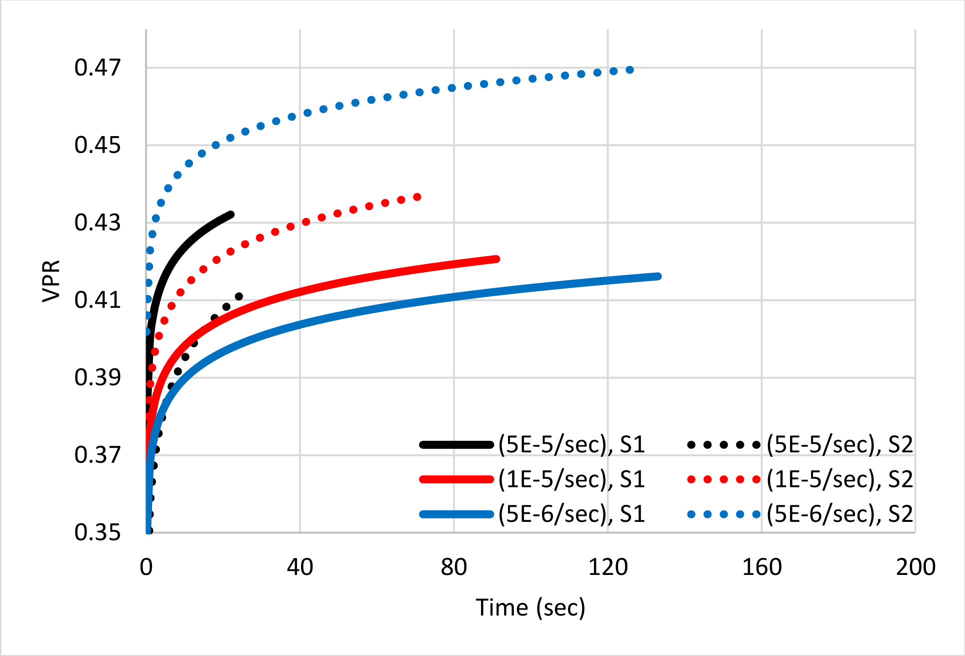

Figure 4.13 Effect of Different Tensile UCSR on Mix-2 at 5ºC

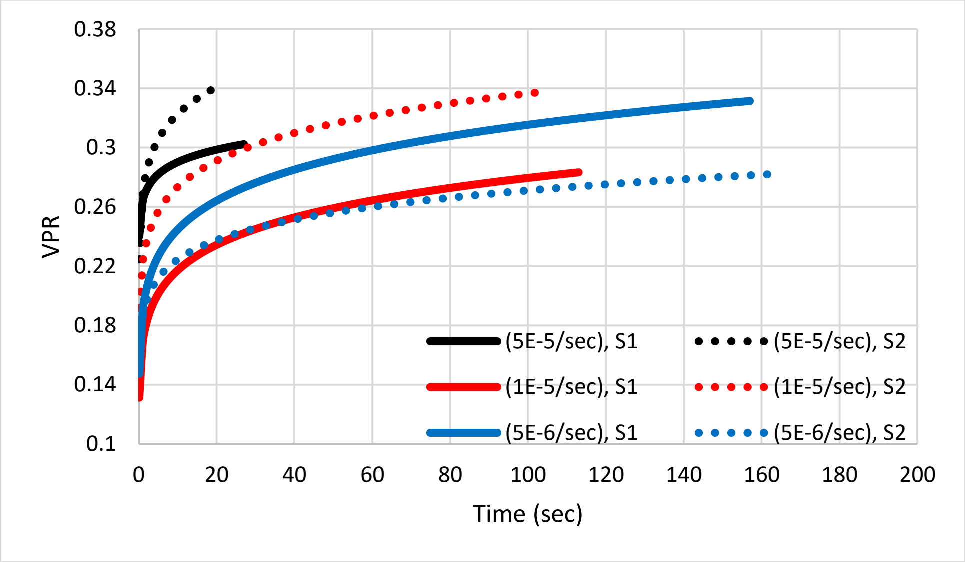

Figure 4.14 Effect of Different Tensile UCSR on Mix-3 at 5ºC

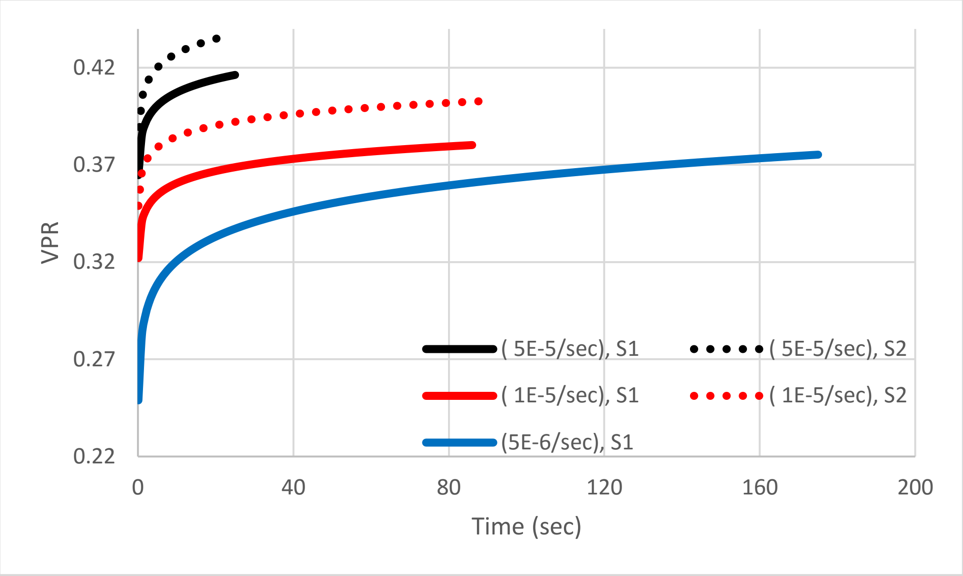

Figure 4.15 Effect of Different Tensile UCSR on Mix-5 at 5ºC

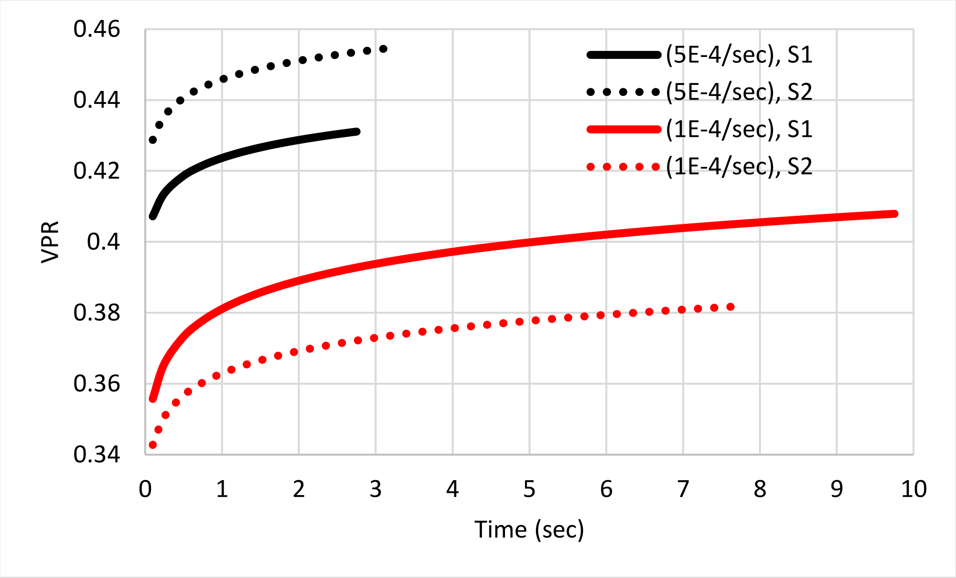

Figure 4.16 Effect of Different Tensile UCSR on Mix-5 at 19ºC

The viscoelastic Young's modulus [E*(t)], shear modulus [G*(t)], and bulk modulus [K*(t)] were calculated for Mix-1, 2, 3, and 5, and Fig. 4.17 shows the results for Mix-2. Figures A.1 to A.4 in Appendix A show the moduli for the remaining mixtures (Mix-1, 3, and 5). The results show the moduli are also dependent on the loading rate where they decrease with lower loading rate. These results are in good agreement with the findings of Kim et al. (2010).

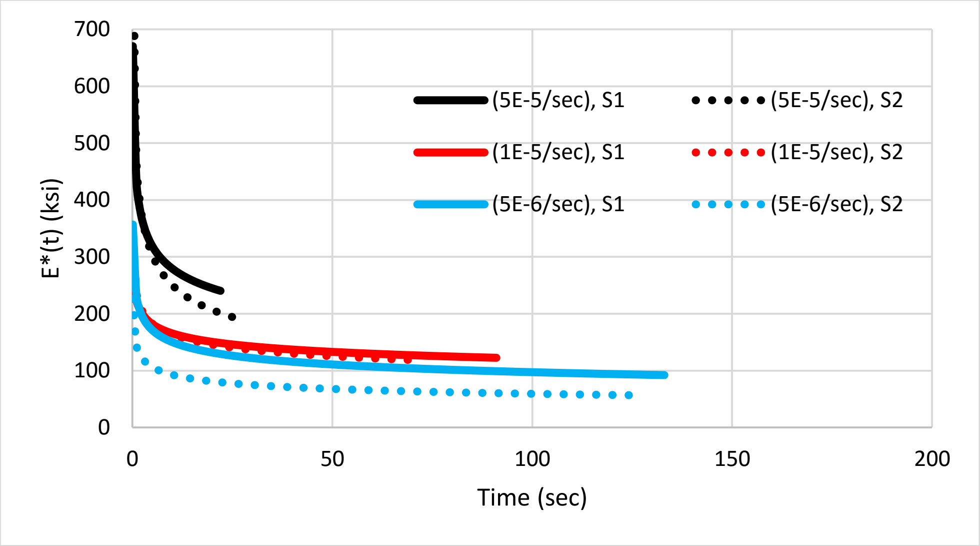

(a) E*(t)

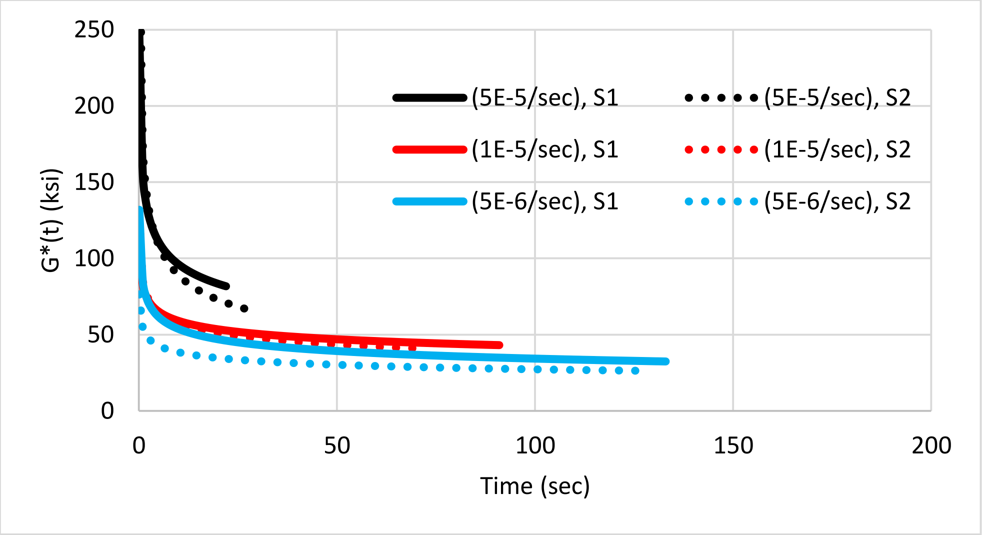

(b) G*(t)

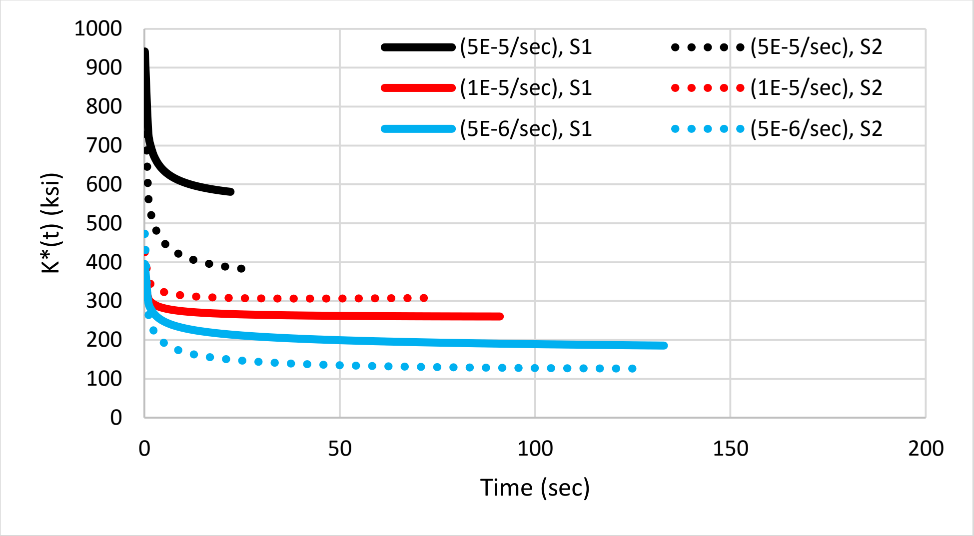

K*(t)

Figure 4.17 (a) E*(t), (b) G*(t), and K*(t) of Mix-2 at 5ºC

As one expected, the results showed that E*(t), G*(t), and K*(t) are higher at faster loading rate. Also, the results demonstrated that shear modulus always relaxes faster than the bulk modulus.

The author explored the error associated by incorrectly assuming the PR as the negative ratio of time-dependent radial to time-dependent axial strains and the correct VPR. Figure 4.18 shows an example of percent error for Mix-3 at different loading rates. Figure A.5 to A.8 show the percent error for the other mixtures. The percent error varied from 1.5% to 11%. The percent error did not show a clear relationship with strain rates and/or temperature. However, Mix-3 has the highest percent error among the all mixtures. Mixture No. 3 is relatively coarser compared to other mixtures (Mix-1, Mix-2, and Mix-5).

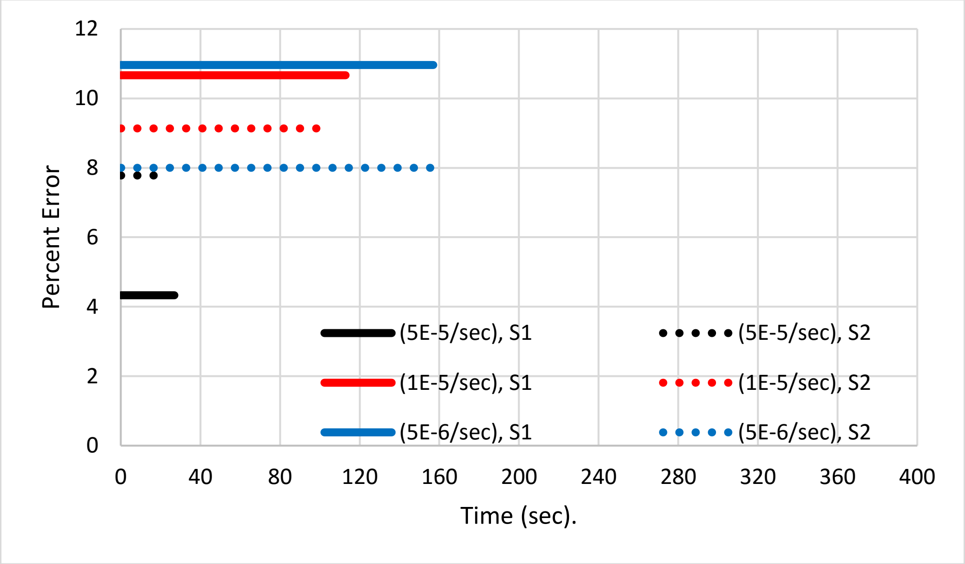

Figure 4.18 Percent Error between PR and VPR for Mix-3 at 5^{o}C

4.4 Influence of Asphalt Mixture Design on VPR

Figures 4.19 to 4.21 show VPR of the various asphalt mixtures at loading rate of 5E-5/sec, 1E-5/sec, and 5E-6/sec, respectively. The results demonstrated that Mix-3 has relatively lower VPR compared to other mixtures. Mix-3 has relatively coarser aggregate gradation compared to other mixtures (Mix-1, Mix-2, and Mix-5) that have similar aggregate gradation. Tashman et al. (2001) and Masad et al. (2002) showed that the aggregates have a preferred orientation perpendicular to the compaction direction. It is believed that the lower VPR of asphalt mixture with coarser aggregate gradation is related to the aggregate-to-aggregate contact, which decreases the radial strain the beginning of the test.

Figure 4.22 shows normalized VPR at a strain rate of 1E-5/sec. The normalized VPR under the strain rate of 5E-5/sec and 5E-6/sec is shown in Fig. B.1 and B.2 in Appendix B. It is interesting to observe that Mix-3 has a higher increasing rate of VPR compared to other mixtures. This emphasizes the significant role of aggregate gradation on the VPR of asphalt mixtures.

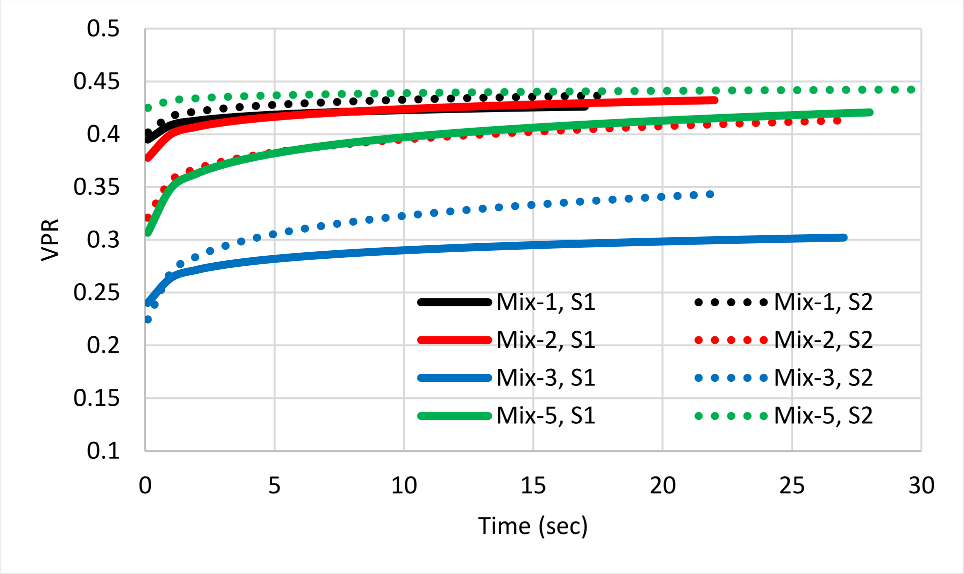

Figure 4.19 VPR of Different Asphalt Mixtures at UCSR of 5E-5/sec in The Direct Tension Test

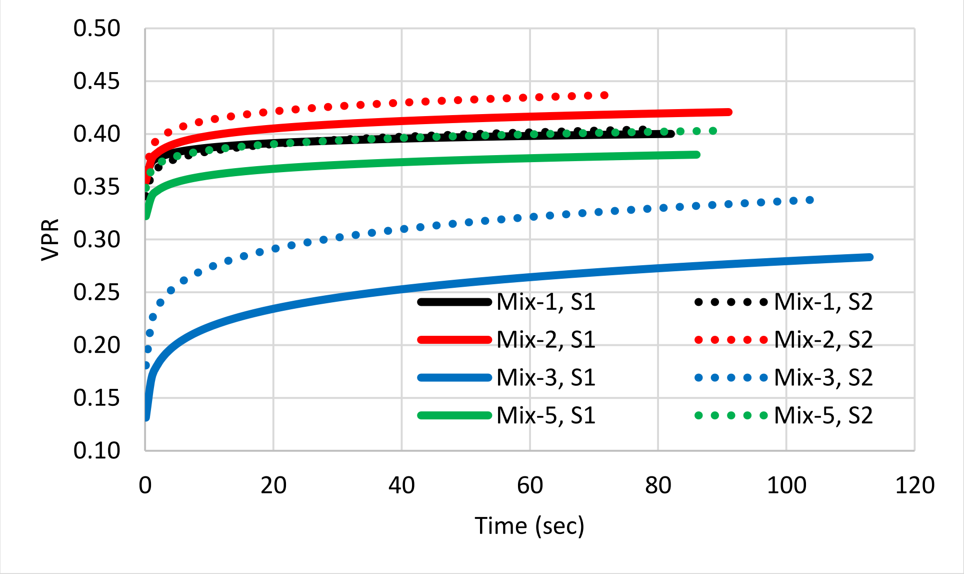

Figure 4.20 VPR of Different Asphalt Mixtures at UCSR of 1E-5/sec in The Direct Tension Test

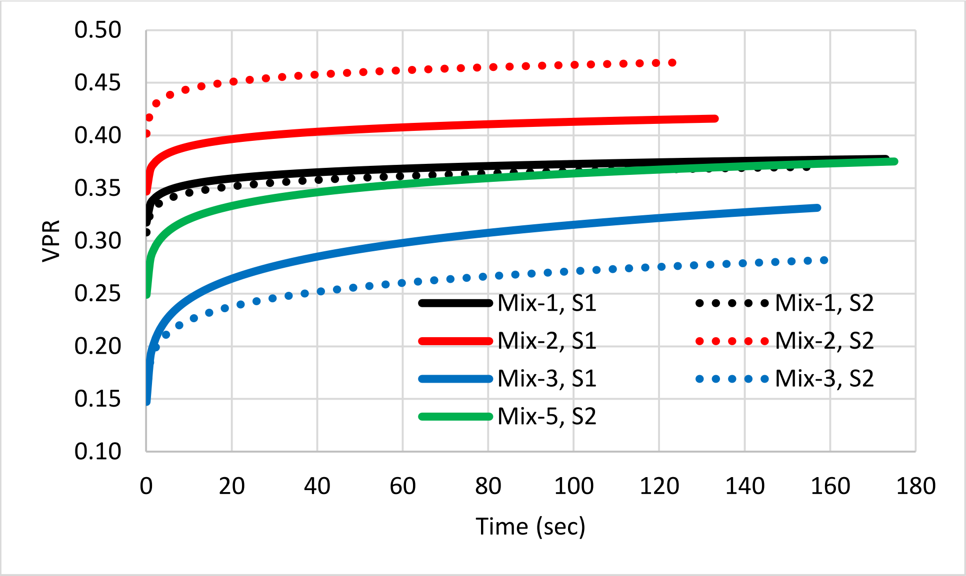

Figure 4.21 VPR of Different Asphalt Mixtures at UCSR of 5E-6/sec in The Direct Tension Test

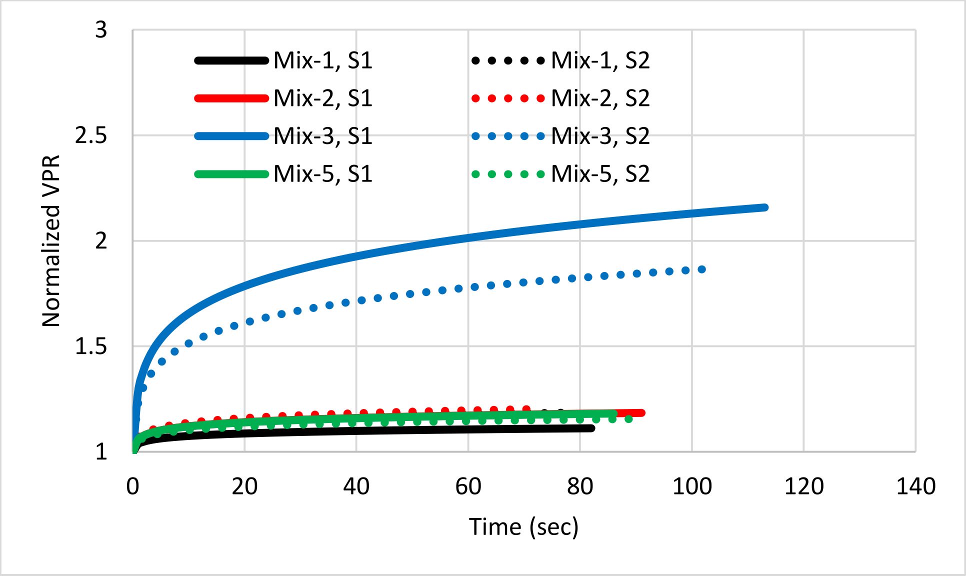

Figure 4.22 Normalized VPR of Different Mixtures at the UCSR of 1E-5/sec

4.5 Influence of Environmental Factors on VPR under UCSR Tension Test

4.5.1 Effect of Moisture on VPR

The mechanical properties of flexible pavements are influenced by the surrounding environment over the years such as temperature and moisture. The diffusion of the water into the asphalt mixes has a direct influence on the mechanical properties where it weakens the adhesive bond between the aggregate and the binder and causes early failures in the pavements (Kassem et al. 2011).

The effect of moisture on VPR was evaluated at 5^{o}C and 19^{o}C. The test included testing dry and wet specimens at different saturation and conditioning times. Chapter 2 provides information about the testing protocol and sample preparation and conditioning. UCSR tests in tension at strain rates of 1E-5/sec at 5^{o}C and 1E-4/sec at 19^{o}C were conducted. Figure 4.23 shows the effect of moisture at 5^{o}C while Fig. 4.24 shows the effect of moisture at 19^{o}C.

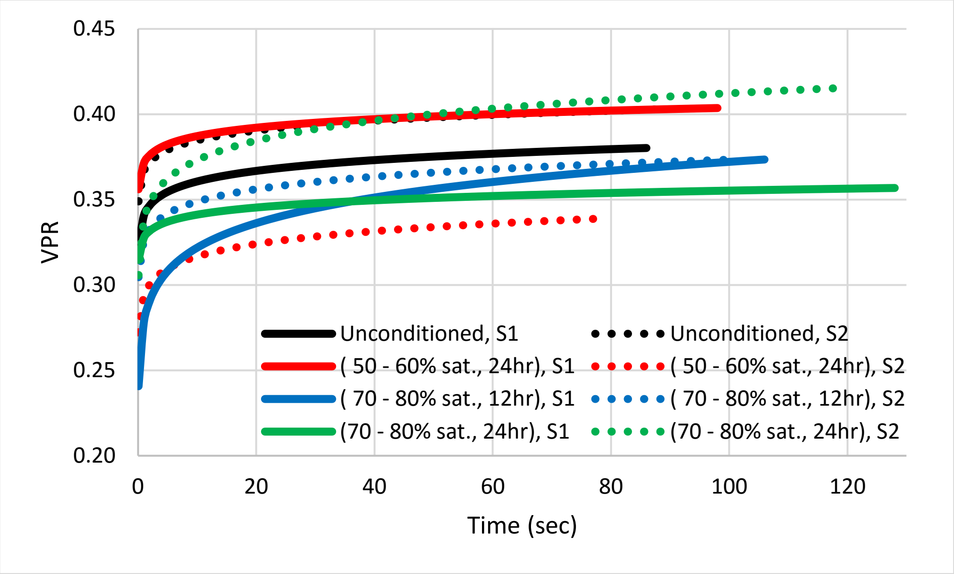

Figure 4.23 Effect of Moisture on VPR at 5ºC

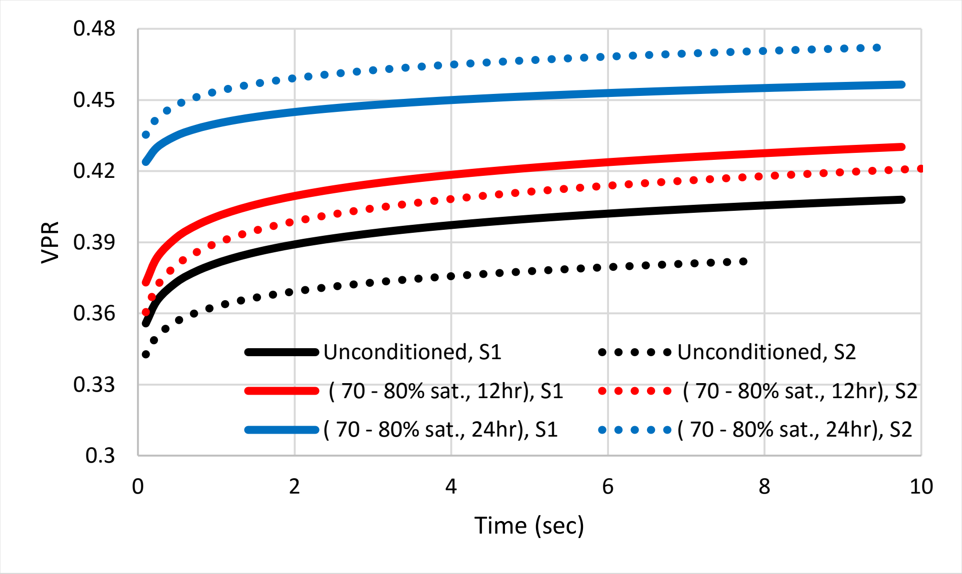

Figure 4.24 Effect of Moisture on VPR at 19ºC

The influence of moisture is not clear in Fig. 4.23 where the VPR with time for the wet samples are overlapping with the dry ones. However, Fig. 4.24 shows that the wet samples have higher VPR compared to the dry (unconditioned) ones. Also, Fig. 4.24 shows that the difference in VPR of 24 hrs-moisture-conditioned samples was higher compared to the 12 hrs-moisture-conditioned samples. This could be due to the loss of adhesion between asphalt binder and aggregates or loss of cohesion of mastic leading to larger deformation in radial direction. It is reported in the literature that the longest axis of the aggregates has a preferred orientation toward the perpendicular direction of compaction of asphalt mixtures (Tashman et al. 2001; Masad et al. 2002). The aggregate interlock in axial direction (direction of compaction) would provide more resistance to deformation compared to radial direction.

4.5.2 Influence of Aging on VPR

In this section, the influence of aging was investigated. The aging of asphalt mixture was simulated and accelerated by placing several samples in a room temperature of 60^{o}C for three months and other set were kept for six months. The reader is referred to Chapter 3 for more information about the sample preparation, conditioning, and testing. The VPR of the aged and non-aged asphalt mixture samples was compared under loading rate of 1E-4/sec and temperature of 19^{o}C.

Figure 4.25 shows the results of VPR of both aged and non-aged samples. The results show that the aged samples have significantly lower VPR than the non-aged ones. The VPR of the 6-month-aged samples was slightly lower than 3-month-aged ones. Previous research showed that there is no significant influence from aging occurred between 3 months and six months (Mehrez et al. 2014). Aging hardening stiffens the asphalt mixture and makes it behave more elastically to the applied loading.

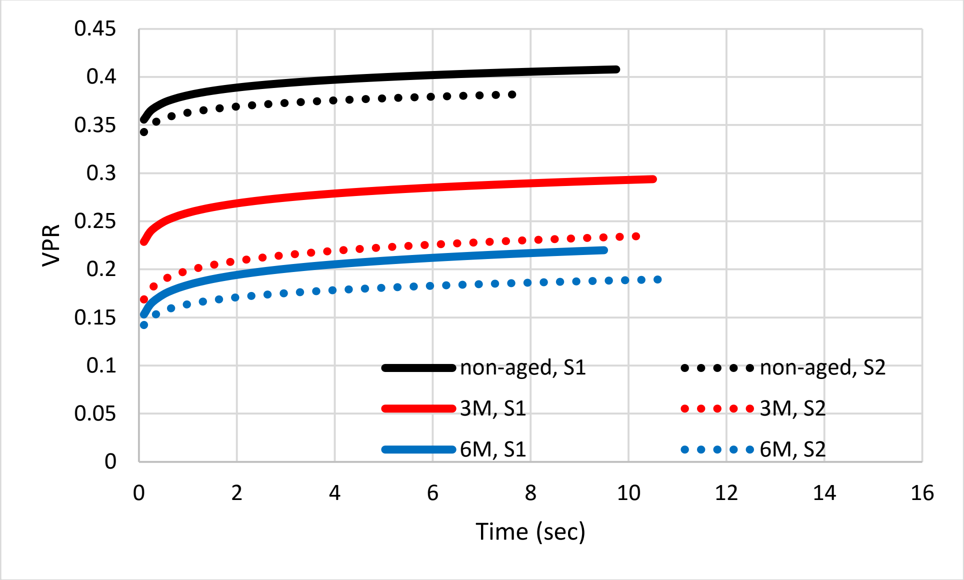

Figure 4.25 Influence of Aging on VPR at 19^{o}C

4.6 Effect of Confining Pressure on VPR

The investigation of the effect of confining pressure was carried out through applying different confining pressures on the same asphalt mixture. The applied UCSR and temperature are 1E-3/sec and 55^{o}C, respectively. Three levels of confining pressures were used in this test including 0 psi, 10 psi, and 20 psi. For 0 psi test, the VPR was calculated according to Eq. 4.14. However, for confining pressures of 10 psi and 20 psi, VPR was calculated according Eq. 4.22. Note that the confining pressure was applied for two hours prior to applying the uniaxial loading.

Figure 4.26 shows the G*(t) while Fig. 4.27 shows the K*(t) for both confined and unconfined UCSR in compression tests. The results show that G*(t) decreases with time as one expects; however, the relaxation rate is higher for the unconfined UCSR compression test compared to the confined UCSR compression test. On the contrary, the relaxation rate of the K*(t) is higher for the confined UCSR compression test compared to the unconfined

UCSR compression test. These responses led to an increase of VPR with time for the unconfined samples while the VPR decreases for the confined samples (Fig. 4.28).

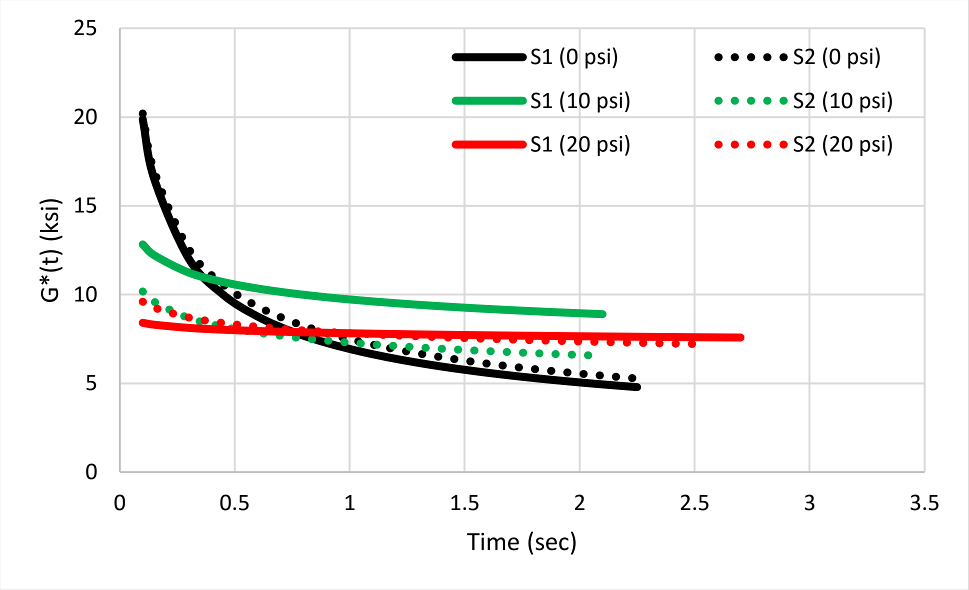

Figure 4.26 Effect of Different Confining Pressures on G*(t)

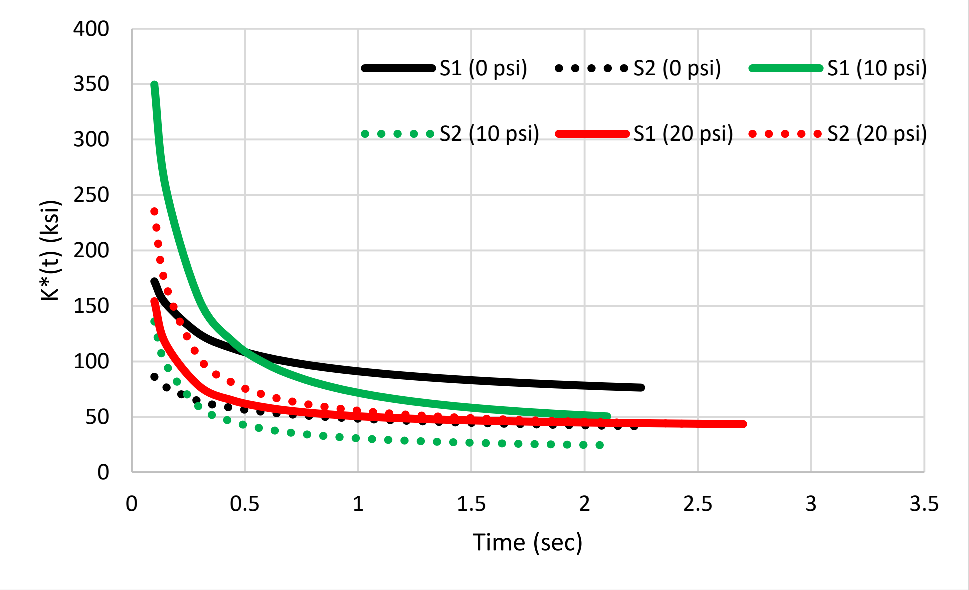

Figure 4.27 Effect of Different Confining Pressures on K*(t)

Figure 4.28 shows VPR of confined and unconfined specimens. This figure shows that the VPR at 0 psi increases with time because the shear relaxation is faster than the dilatational relaxation. However, the VPR decreases with time for the confined samples because the dilatational relaxation is faster than the shear relaxation. Also, VPR is dependent on the level of confining pressure where the lower the confining pressure, the higher the decreasing rate of VPR. The researchers recommend conducting further testing on asphalt mixtures with different gradations at different temperatures to verify the findings of this section.

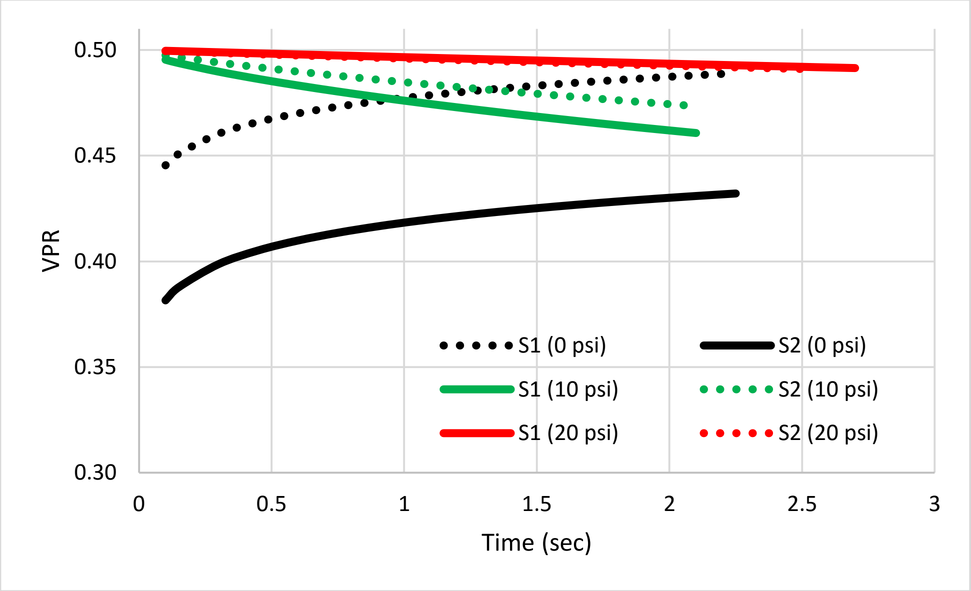

Figure 4.28 VPR versus Time under Unconfined and Confined UCSR Compression Loading- Mix-5

4.7 Summary

Various asphalt mixture samples were subjected to UCRS in tension and compression to evaluate the VPR at different conditions. The researchers found that the VPR increased with time for the unconfined test samples in both tension and compression because the shear relaxation was faster than the dilatational relaxation. While the VPR decreased for confined test samples where dilatational relaxation was faster than the shear relaxation. The researchers found that the percent error of incorrectly assuming the PR as the negative ratio of time-dependent radial strain to time-dependent axial strain is significant in some cases. In addition, the aggregate gradation was found to influence the VPR of asphalt mixtures. Coarser asphalt mixtures were found to have lower VPR compared to finer ones.

The results of this section showed that moisture-conditioned samples had relatively higher VPR compared to the dry ones. Also, the duration of moisture conditioning was found to impact the VPR. In addition, aging was found to have major effect on the VPR. The aged samples had lower VPR compared to the non-aged samples.

CHAPTER – 5 ANALYSIS OF THE ANISOTROPY OF ASPHALT MIXTURES

5.1 Introduction

The constitutive viscoelastic models assume that the asphalt concrete mixes are homogeneous and isotropic (Kassem et al. 2013; Teschegl et al. 2002). Underwood et al. (2005) proposed a test method to quantify the induced anisotropy under a hydrostatic pressure. The author used the proposed method to investigate the degree of anisotropy of asphalt mixtures at different conditions. The test samples were subjected to two hours of hydrostatic pressure and both axial and radial deformations were recorded. Figure 5.1 shows an example of the applied confining pressure of 10 and 20 psi. The author investigated the influence of mix design, level of confining pressure, temperature, and porosity on the degree of anisotropy. The results of this section shed light on the limitations of assuming asphalt mixtures being isotropic. This assumption is made to simplify the models used to analyze the performance of asphalt mixtures.

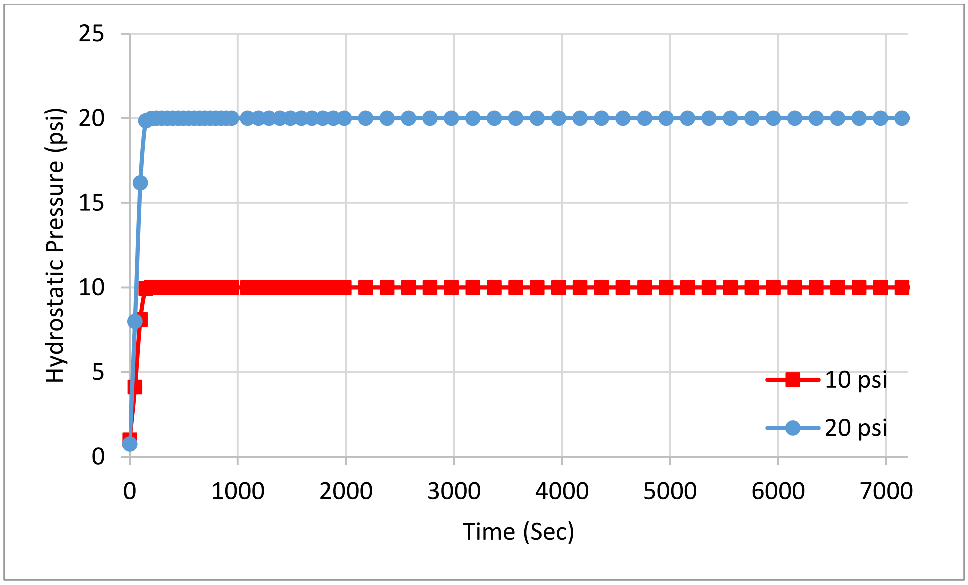

Figure 5.1 Example of Applied Hydrostatic Pressure for Two Hours

5.2 Influence of Mix Design on the Degree of Anisotropy of Asphalt Mixtures

This section discusses the influence of the mix design on the anisotropy of asphalt mixtures. Four mixtures were evaluated: Mix No. 1, 2, 3, and 4. Test samples of these mixtures were subjected to confining pressure of 20 psi at 55^{o}C. The calculated axial and radial strains for Mix-2 are presented in Fig. 5.2. Figures C.1 to C.3 in Appendix C show the calculated strains for Mix-1, 3, and 4, respectively. The strains are expressed with a negative sign to indicate contraction.

It can be seen from Fig. 5.2 that a significant deformation occurred once the hydrostatic pressure was applied, then a gradual change in deformation was observed with time. It should be noted that this test was conducted at 55^{o}C, so the samples were soft enough to deform with a faster rate compared to low temperatures, as discussed later in this chapter.

The degree of anisotropy was quantified by a parameter called anisotropy ratio as presented in Eq. 2.50. This parameter is the ratio of radial strain to axial strain. For isotropic material, the strain ratio should be 1 and the degree of anisotropy increases as the anisotropy ratio increases. Figure 5.2 shows that the radial strain is larger than the axial strain because of the anisotropy nature of asphalt mixtures. It should be noted that two replicates or samples were tested at each condition (S1 and S2).

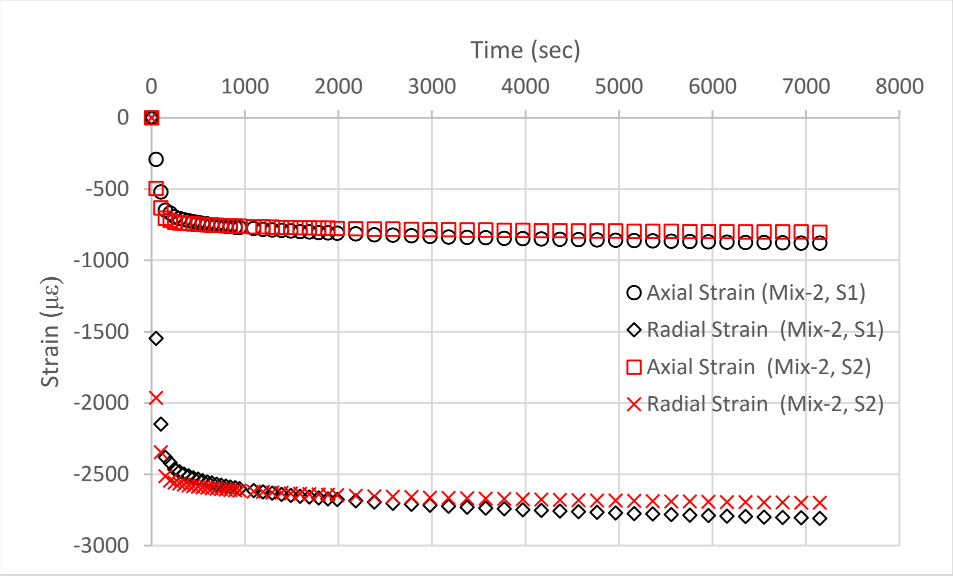

Figure 5.2 Mix-2 Axial and Radial Strains under Hydrostatic Pressure of 20 psi at 55°C

Figure 5.3 demonstrates that of the anisotropy ratio of various asphalt mixtures evaluated in this study. The anisotropy ratio results showed that various asphalt mixtures demonstrated different levels of anisotropy (e.g. Mix-1 had an anisotropy ratio of 3.6 to 2.7, from 3.6 to 3.4 for Mix-2, from 5 to 4 for Mix-3, and from 3.6 to 3.5 for Mix-5). The variation of the anisotropy of these mixtures are discussed below.

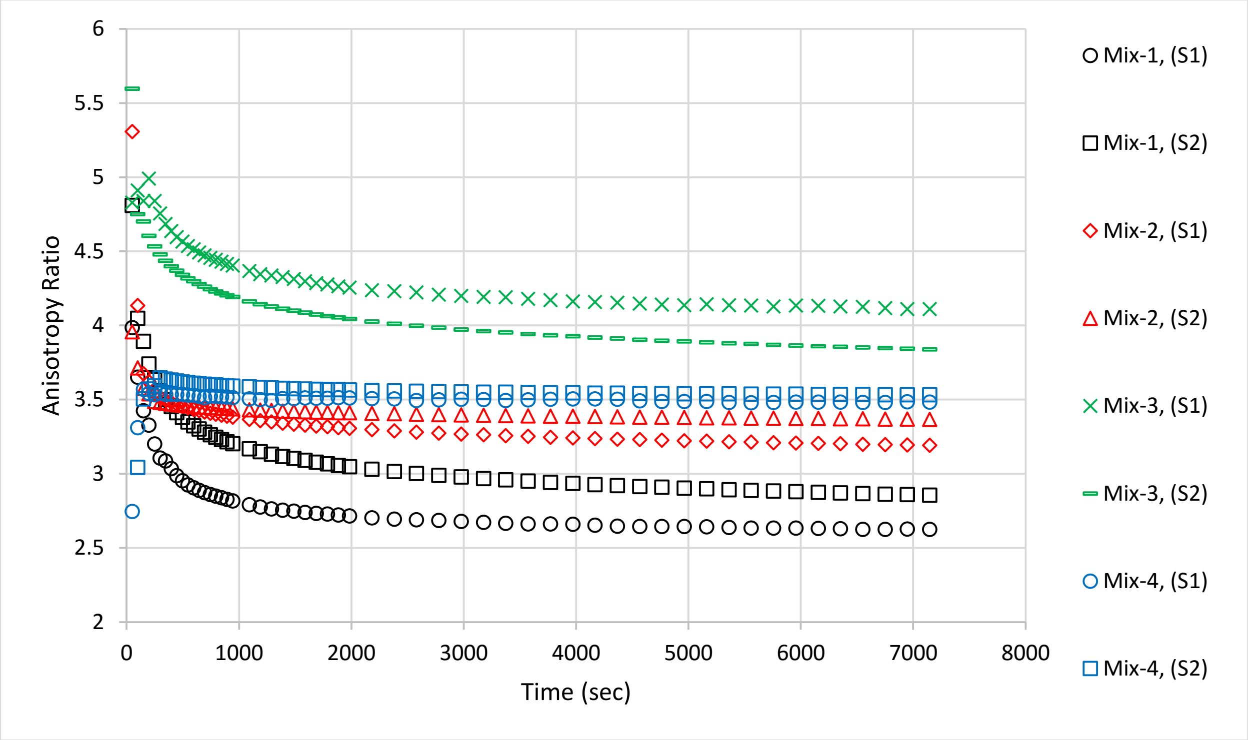

Figure 5.3 Anisotropy Ratio of Different Asphalt Mixtures at 55ºC

Since the evaluated mixtures had different mix design, the author investigated the influence of aggregate gradation and binder content of the evaluated asphalt mixtures on the anisotropy. Figure 5.4 shows the binder content in the mixtures versus the maximum strains. The maximum strains are defined in this study as the terminal (final) axial and radial strains after two hours of the application of confining pressure. It can be seen that there is no clear trend or relationship between binder content and maximum axial or radial strains.

Figure 5.5 shows a relationship between the nominal maximum aggregate size (NMAS) and maximum strains. It is obvious that the radial strain increased with the increase of NMAS. It is reported in the literature that the longest axis of aggregate particles has preferred orientation toward the perpendicular direction of compaction of asphalt mixtures (Tashman et al. 2001; Masad et al. 2002). The author believes that there is no significant effect for the NMAS on the axial strain due to the aggregate interlock (aggregate-to-aggregate contact); however, the aggregates can mobilize easier in the radial direction with the increase of the NMAS.

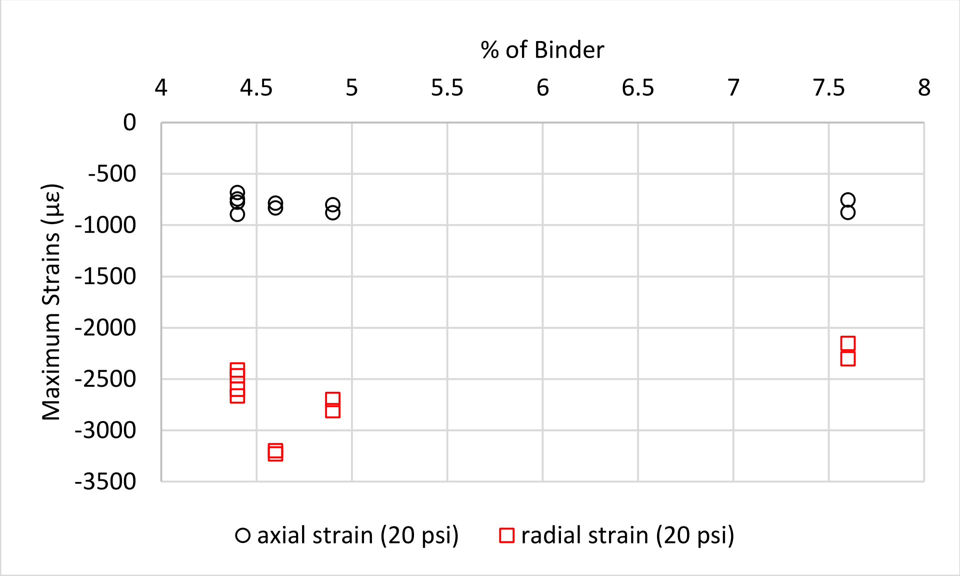

Figure 5.4 Influence of Binder Content on the Maximum Strains at 55ºC

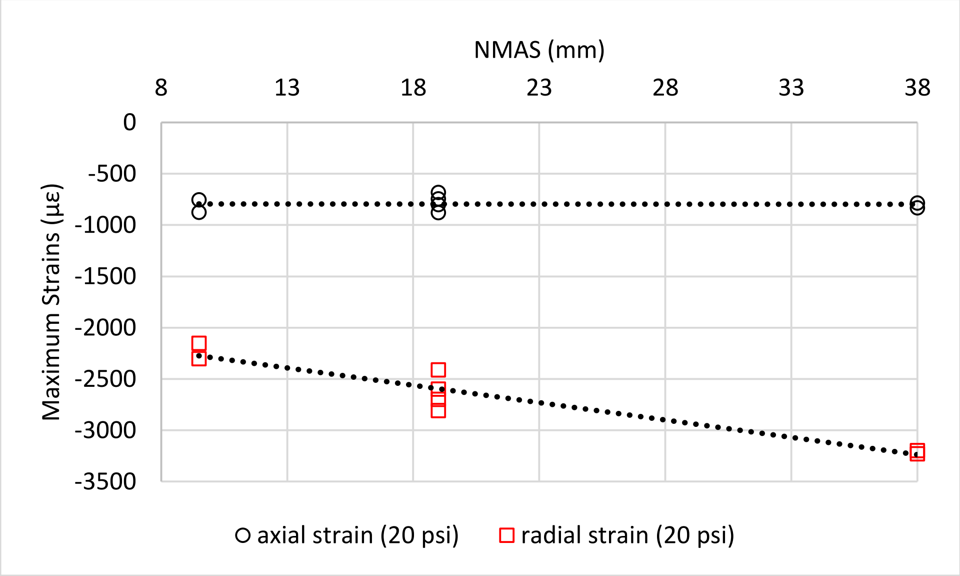

Figure 5.5 Influence of the NMAS on the Maximum Strains at 55ºC

5.3 Influence of Confinement Level and Temperature on Anisotropy

In this section, the author investigated the dependency of anisotropy on the level of confinement and temperature. Mix-4 was confined at 10 psi and 20 psi, at different temperatures of 19^{o}C, 40^{o}C, and 55^{o}C. The resulting strains (axial and radial) at 20 psi are shown in Fig. 5.6 and 5.7 at 19^{o}C and 40^{o}C, respectively. The resulting strains for other conditions are shown in Figs. C.4 to C.7 in Appendix C. Comparing the change of the strains versus time shown in Figs. 5.6 and 5.7, the resulting strains at 19^{o}C had lower increase rate compared to 40^{o}C since the asphalt mixtures are stiffer at lower temperatures.

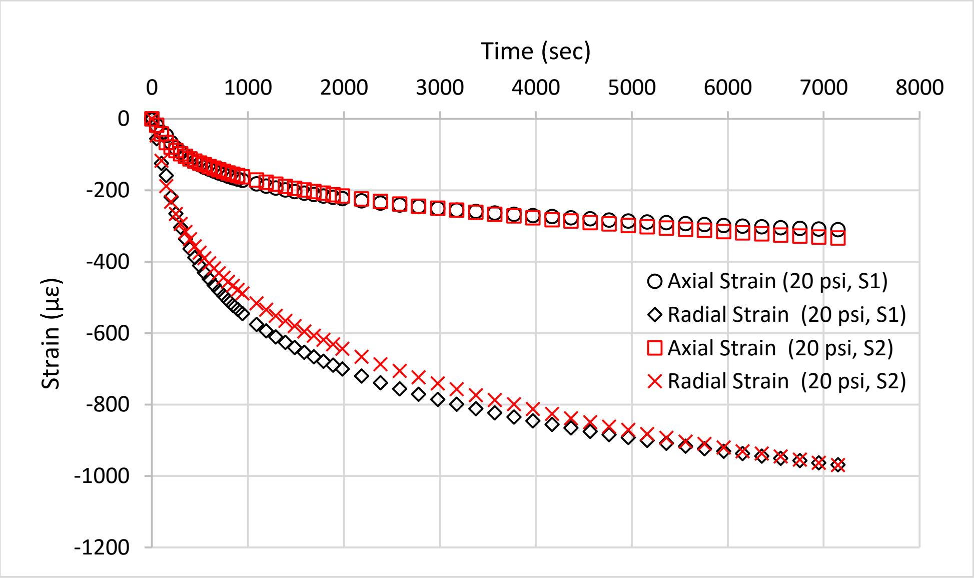

Figure 5.6 Mix-4 Axial and Radial Strain under Hydrostatic Pressure of 20 psi at 19^{o}C

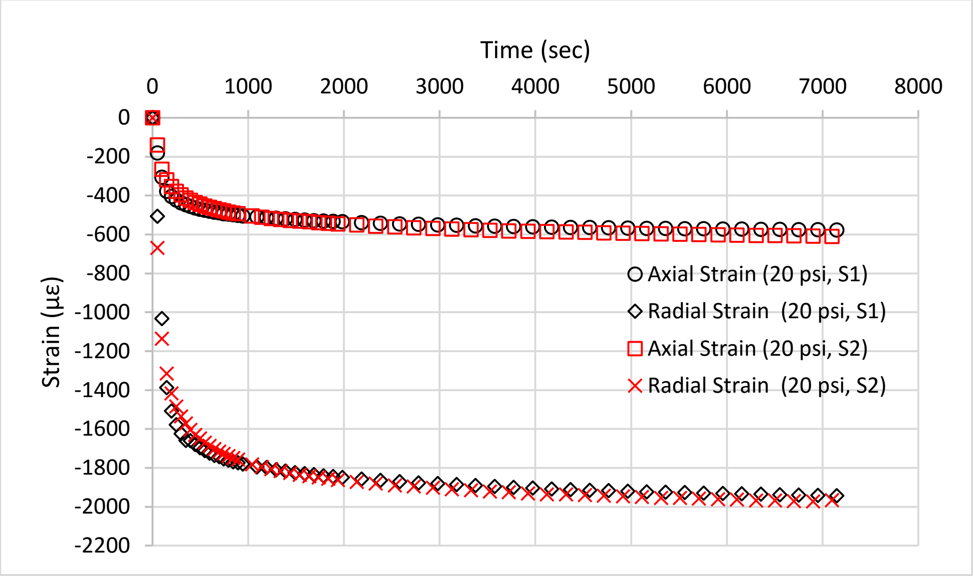

Figure 5.7 Mix-4 Axial and Radial Strain under Hydrostatic Pressure of 20 psi at 40ºC

Figures 5.8 to 5.10 show the effect of the confining pressure on the anisotropy ratio at 19ºC, 40ºC, and 55ºC, respectively. It is clear that as the confining pressure increases, the anisotropy ratio increases. Therefore, the anisotropy is dependent on the level of confining pressure. Also, the effect of temperature on the anisotropy is shown in Fig. 5.11 and 5.12 at confining pressure of 10 psi and 20 psi, respectively. The results demonstrated that the anisotropy ratio increases as the temperature increases, so the anisotropy is also dependent on temperature.

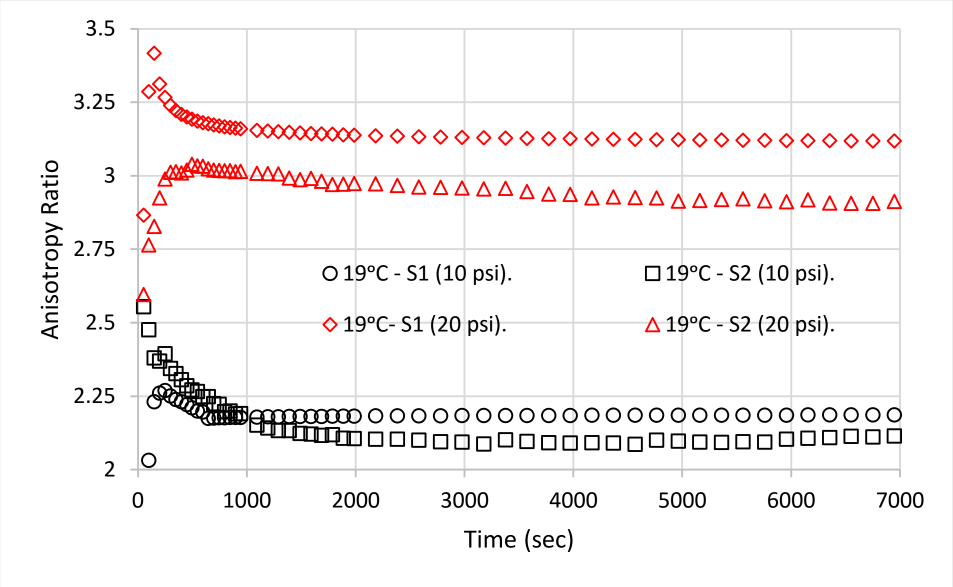

Figure 5.8 Anisotropy Ratio of 10 psi and 20 psi at 19ºC

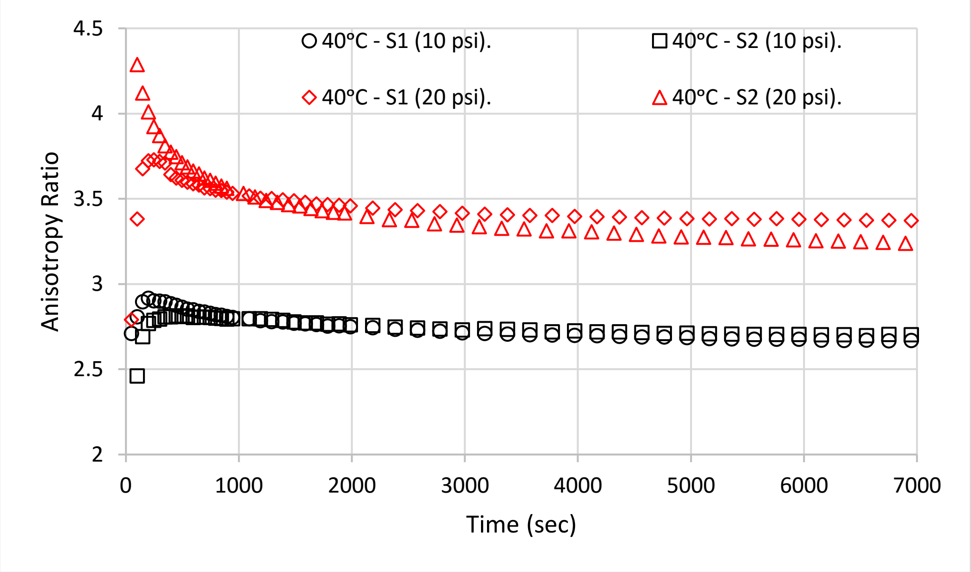

Figure 5.9 Anisotropy Ratio of 10 psi and 20 psi at 40ºC

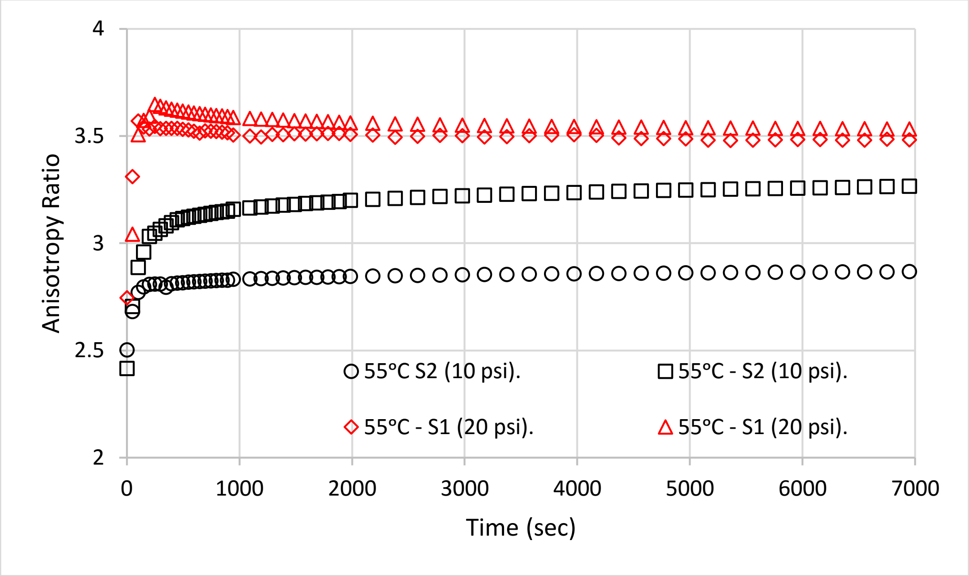

Figure 5.10 Anisotropy Ratio of 10 psi and 20 psi at 55ºC

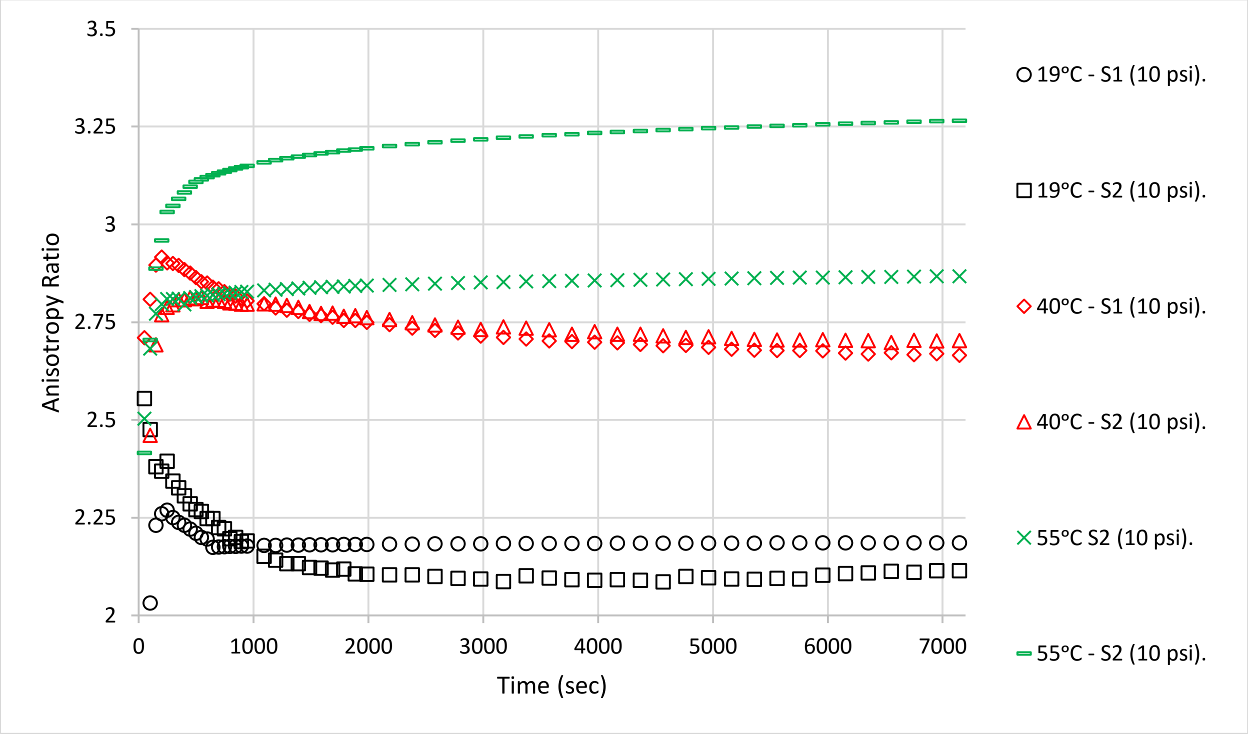

Figure 5.11 Influence of Temperature on the Anisotropy Ratio at 10 psi

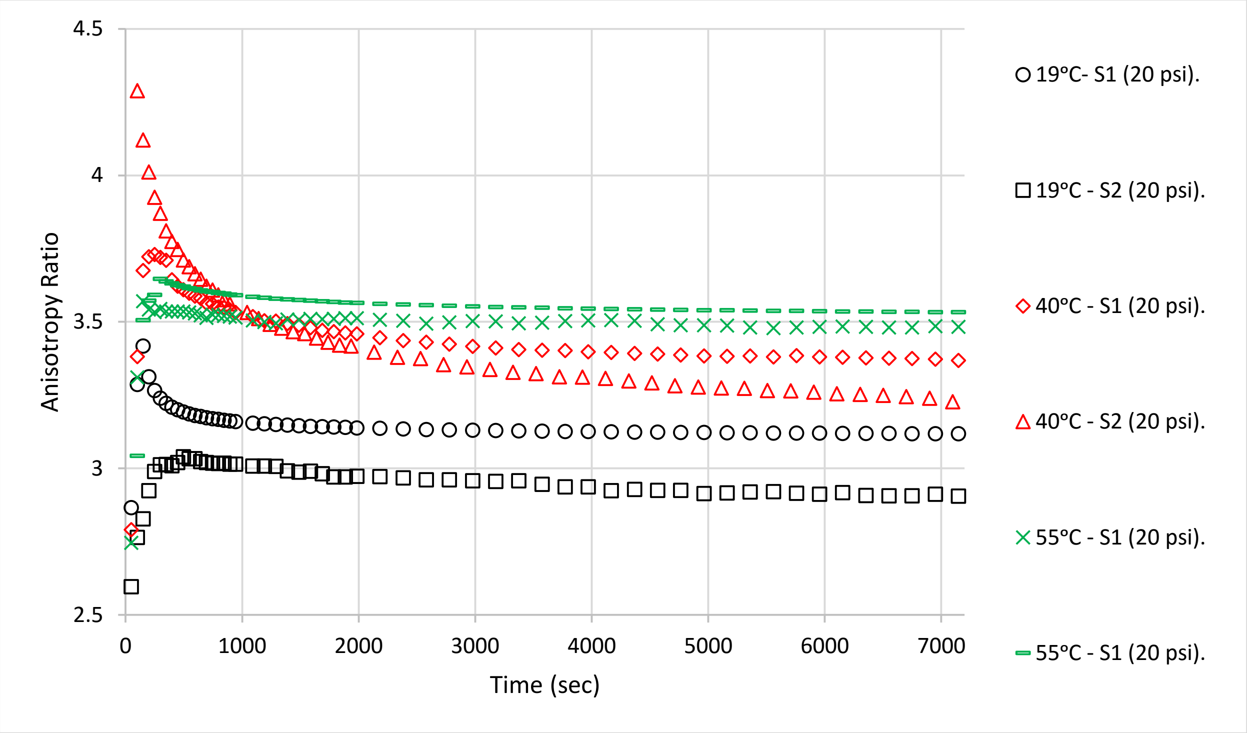

Figure 5.12 Influence of Temperature on the Anisotropy Ratio at 20 psi

Figures 5.13 and 5.14 show the influence of the confining pressure and temperature on the maximum axial and radial strains, respectively. One can see from Fig. 5.13 that the maximum axial strains at 20 psi are slightly higher than the ones at 10 psi which indicates that the level of confinement is slightly effecting the axial strain. However, Fig. 5.14 demonstrates that maximum radial strains are greatly influenced by the level of confinement pressure. The radial strain increased with the confining pressure, thus the anisotropy ratio increases with increasing level of confining pressure.

In addition, Figs. 5.13 and 5.14 show that both maximum axial and radial strains are dependent on the temperature, and both increase with temperature. Also, it is noted that the increasing rate of the maximum radial strain is higher than the maximum axial strain which explains the increasing in the anisotropy with temperature. As explained in section 5.2, the radial side is always weaker because of the preference of the longest axes of the aggregate particles to orient perpendicularly to the direction of compaction.

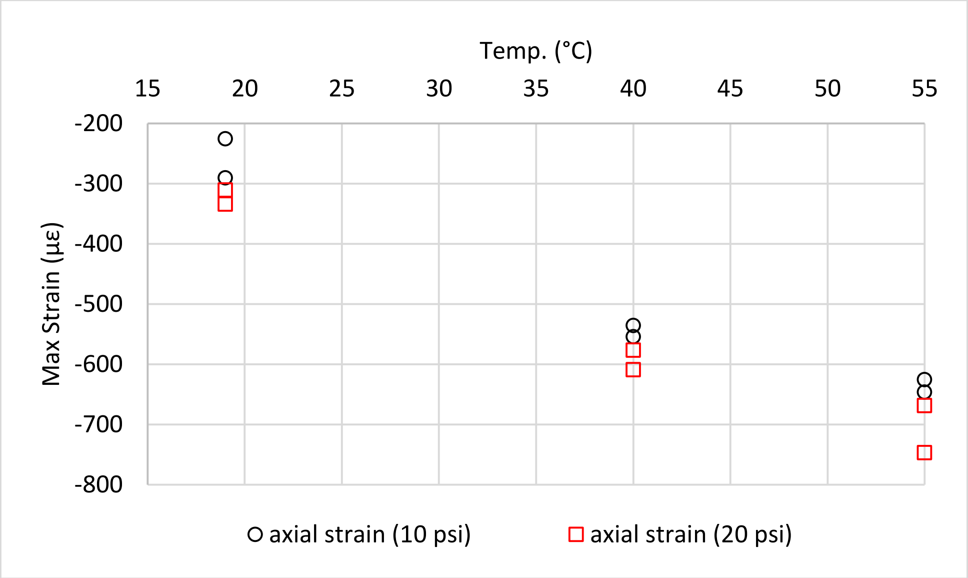

Figure 5.13 Influence of both Hydrostatic Pressure and Temperature on the Maximum Axial Strains

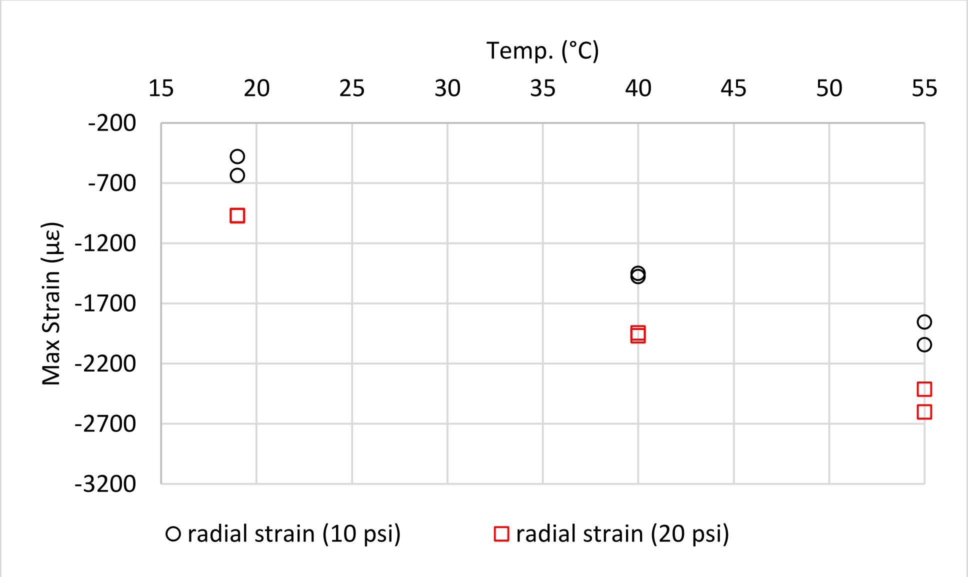

Figure 5.14 Influence of both Hydrostatic Pressure and Temperature on the Maximum Radial Strains

5.4 Effect of Air Void Content on The Anisotropy

The influence of the air void content on the anisotropy is investigated in this section. Mix-4 was compacted to produce test samples with 4 ± 0.5% and 7 ± 0.5% air voids. The test samples were subjected to a confining pressure of 20 psi at 40^{o}C. Figures 5.15 and 5.16 show the creep strains at 4% and 7% air void, respectively. Also, Fig. 5.17 show the anisotropy ratios at these conditions.

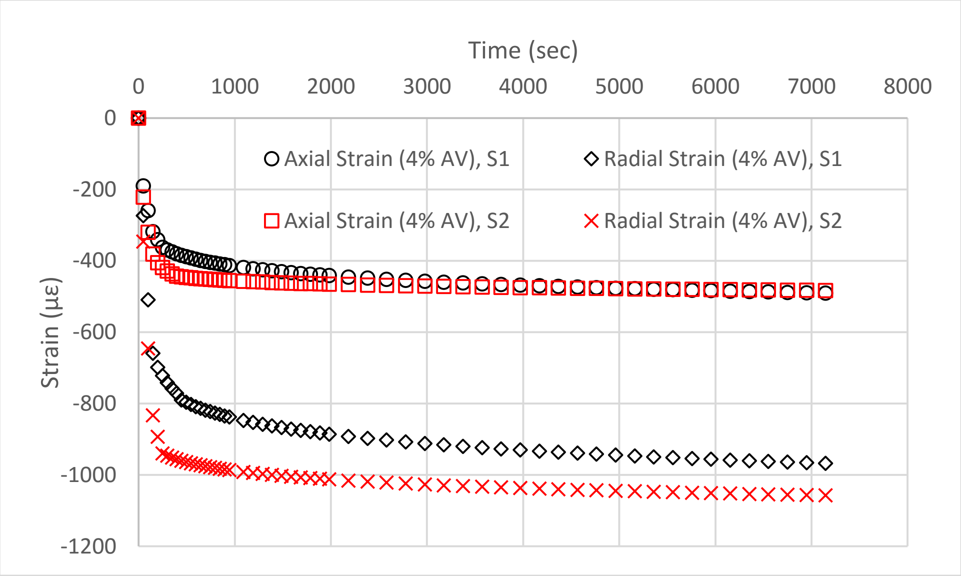

Figure 5.15 Creep Strains of 4% Air Void Samples at 40^{o}C (Mix-4)

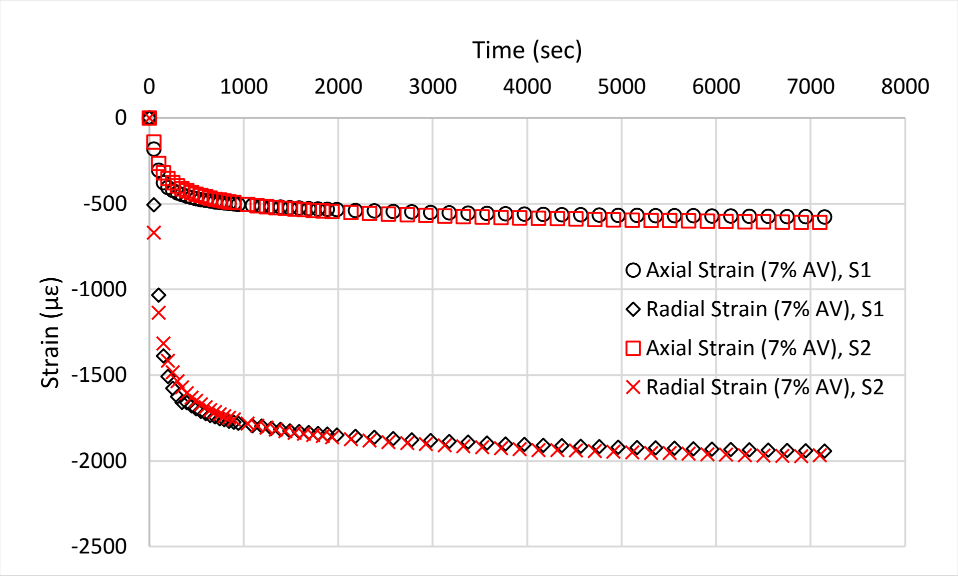

Figure 5.16 Creep Strains of 7% Air Void Samples at 40^{o}C (Mix-4)

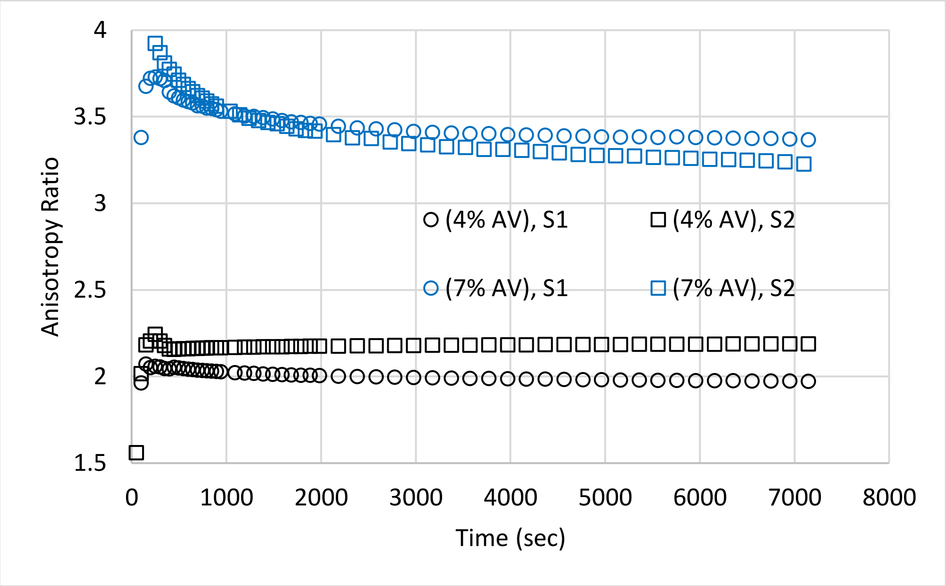

Figure 5.17 Anisotropy Ratio of 4% and 7% Air Void Samples at 40^{o}C (Mix-4)

The 4% air void samples had an isotropy ratio of about 2.2 to 2.1, whereas the 7% air void samples have an isotropy ratio of about 3.6 to 3.2. It should be noted that Underwood et al. (2005) reported an isotropy ratio of 1.7 for asphalt mixtures at 4% air voids and at a temperature of 25^{o}C; however, the aspect ratio of the test samples of Underwood's study was 1.2 whereas it is 1.5 in this study. In addition, as demonstrated in this study, asphalt mixtures with different mix design at different temperature have different anisotropy ratio.

The results of this section demonstrated that the anisotropy increases with increasing the percent of air void. The increase in the anisotropy is explained by the creep strains in Figs. 5.15 and 5.16. One can observe that the percent of air voids effects both the axial and radial strains, but the difference between the radial strains is relatively higher than the axial ones because it is the weaker side as in Fig. 5.18 which shows the maximum strains.

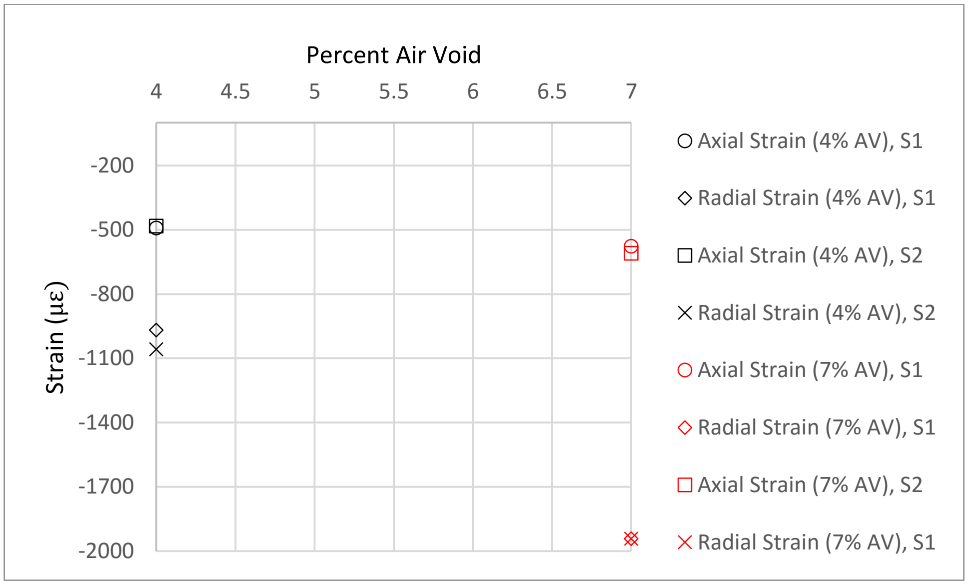

Figure 5.18 Influence of Percent Air Void on Both Maximum Axial and Radial Strains at 40°C

5.5 Quantification of the Anisotropy using X-ray CT Analysis

In this section, the degree of anisotropy (DA) of air void distribution in asphalt mixture tests samples was examined. Field cores were extracted from pavement test sections subjected to a different number of compaction passes to produce different level of densities. These sections were constructed using dense graded asphalt mixtures (9.5 mm Superpave mixture) and compacted using static and vibratory rollers. The reader is referred to Kassem et al. (2012) for more information about the mix design and construction of these test sections. Field cores were extracted after compaction and the cores were 6 in. in diameter and 2 in. thick.

The X-ray Computed Tomography (CT) was used to scan the field cores. The X-ray CT is a nondestructive technique used to study the internal structure of an object. The test specimen is placed in between the X-ray source and linear detector as shown in Fig. 5.19. The source sends X-rays that penetrate through the sample with no destruction or damage and the intensity of the x-rays is measured before and after they penetrate the test sample. The change of intensity of the X-rays is related to the intensity of different phases in the sample. The sample is rotated 360° and moved up or down to take X-ray CT scans along the height of a test sample. The scanned images were further processed to separate the air voids from other constituents (rock and mastic). Figure 5.20 shows an example where the black area represents air voids while other constituents are in white.

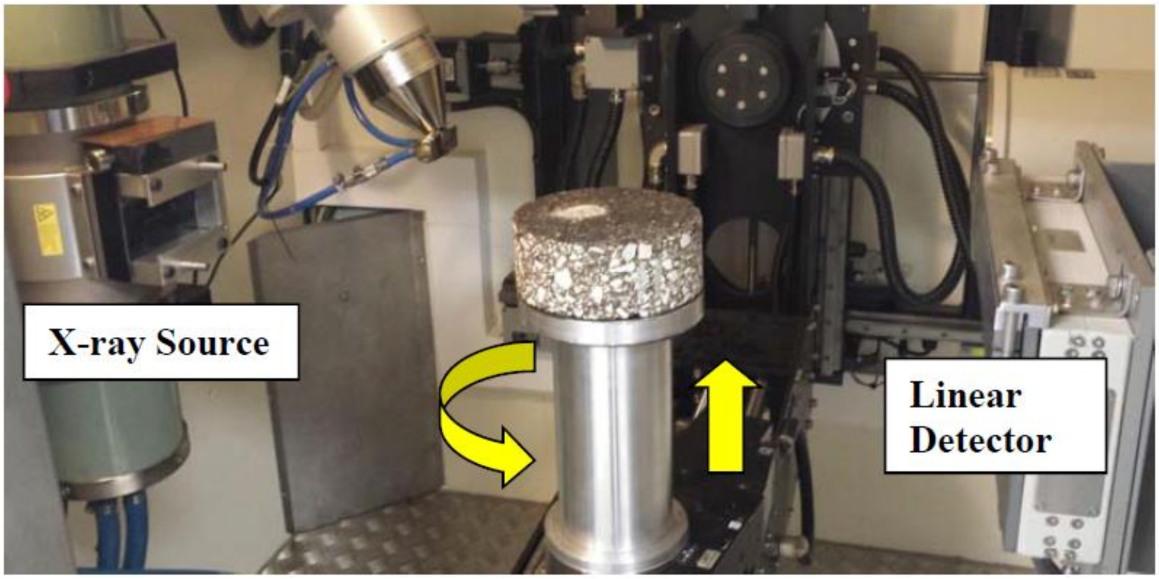

Figure 5.19 X-ray CT Scanning System

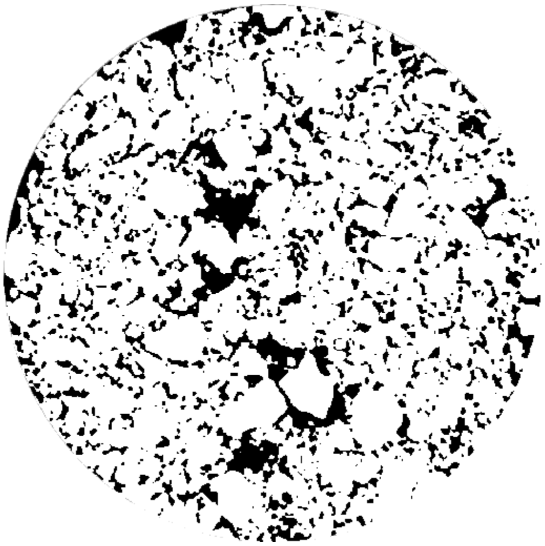

Figure 5.20 A Typical Image Slice with Air Voids (Black) and Other Internal Structure (White)

Kassem et al. (2016) used a software called Image-Pro Plus to study the air void distribution along the height of these cores as shown in Fig. 5.21. Figure 5.21 shows that the air void decreases with the number of passes. The vibratory roller was more effective in reducing the air voids compared to the static roller at the corresponding number of passes. In addition, the air void was more uniform towards the top of the field cores (Kassem et al. 2016).

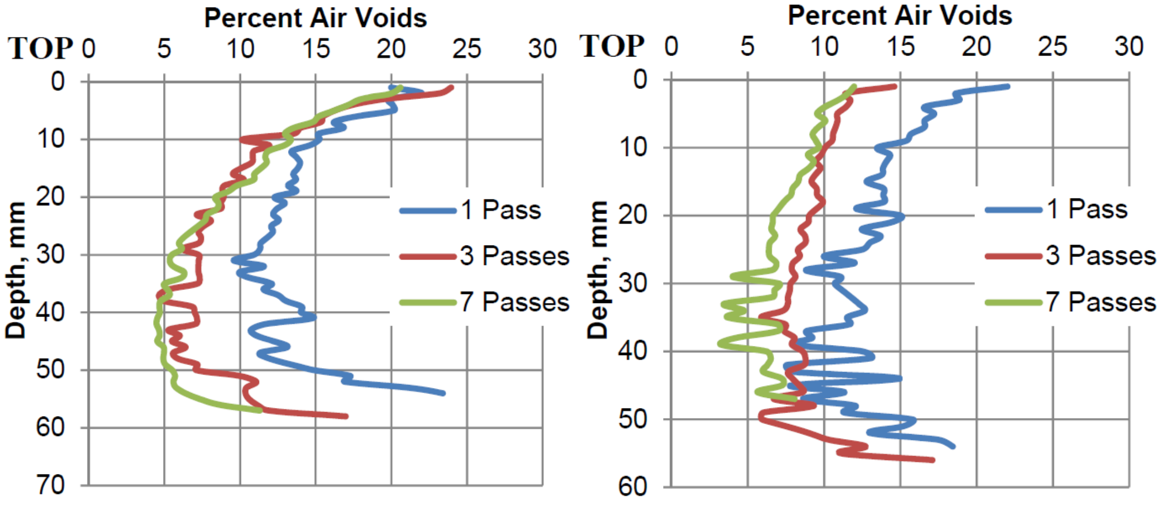

(a) Static Roller (b) Vibratory Roller.

Figure 5.21 The Air Void Distribution Across the Depth of (a) Static Roller and (b) Vibratory Roller (Kassem et al. 2016)

There are several methods and parameters used to quantify the DA in a composite material. These parameters include the Mean Intercept Length (MIL), Star Length Distribution (SLD), and Star Volume Distribution (SVD) (Ketcham 2005; Ketcham and Ryan 2004). The MIL uses the mean distance between material intersections of two-component composite and number of intersections. The MIL is defined as the total length divided by the number of intersections. However, the orientation of the interface rather than the object may influence the MIL measure according to Bhasin et al. (2011). Alternative methods used to quantify the degree of anisotropy (DA) are the SLD and SVD. The SLD measures the DA based on randomly distributed points in the material of interest and measuring the length of lines that emanating from these points in different directions until they encounter a boundary (Bhasin et al. 2011; Ketcham 2005; Ketcham and Ryan 2004). Figure 5.22 shows a schematic view of SLD measurements in two dimensions (2D) (Bhasin et al. 2011). The SVD is similar to the SLD, but the lines are replaced with cones emanating from the randomly distributed points. The SLD and SVD are calculated according to Eqs. 5.1 and 5.2, respectively.

$$S_w = \frac{1}{n}\sum_{i=1}^{n} L_i \tag{5.1}$$

$$U_w = \frac{\pi}{3n}\sum_{i=1}^{n} {L_i}^3 \tag{5.2}$$

where *L* is the intersection length that passes through point *i* and *n* is the number of points at an orientation *w*.

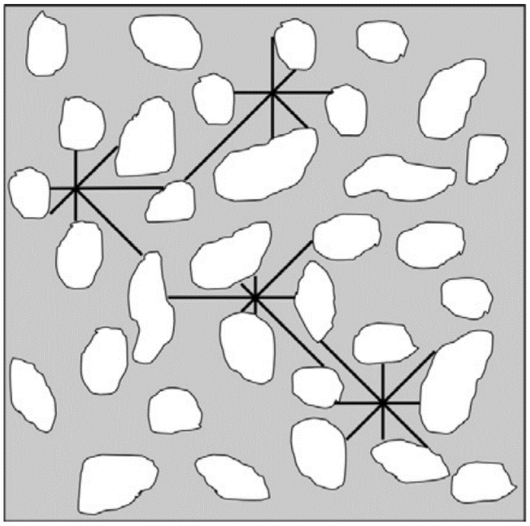

Figure 5.22 2D Schematic View of SLD between Aggregates (white) and Mastic (gray) (Bhasin et al. 2011)

Two approaches are often used to summarize the MIL, SLD, and SVD measurements. These approaches are the fabric tensor and three-dimensional rose diagram.

The fabric tensor describes how the moment of inertia or a certain quantity varies at different orientation (Ketcham and Ryan 2004).

The fabric tensor eigenvectors (**û₁, û**₂, **û**₃) and eigenvalues ($\hat{\tau}_1 > \hat{\tau}_2 > \hat{\tau}_3$) are calculated as follows:

- Consider a vector $\mathbf{a}_i$ from point *i* along an orientation that has spherical coordinates of (θ_i, ϕ_i). The vector $\mathbf{a}_i$ at an orientation coordinates of (θ_i, ϕ_i) can be calculated as

$$a_i = \begin{bmatrix} a_{xi} \\ a_{yi} \\ a_{zi} \end{bmatrix} = \begin{bmatrix} |a_i|\ sin\theta_i \cos\phi_i \\ |a_i|\ sin\theta_i \sin\phi_i \\ |a_i|\ cos\theta_i \end{bmatrix} \tag{5.3}$$

where $|a_i|$ is the measured value of the vector at that orientation.

- At an arbitrary axis **u**, the moment of inertia can be calculated as

$$I(u) = \sum_{i=1}^{n} |a_i|^2 - u^T T u \tag{5.4}$$

where T is the orientation matrix which can be found as:

$$T = \sum_{i=1}^{n} a_{xi} a_i{}^T = \begin{bmatrix} \sum_{i=1}^{n} a_{xi}{}^2 & \sum_{i=1}^{n} a_{xi}a_{yi} & \sum_{i=1}^{n} a_{xi}a_{zi} \\ \sum_{i=1}^{n} a_{xi}a_{yi} & \sum_{i=1}^{n} a_{yi}{}^2 & \sum_{i=1}^{n} a_{yi}a_{zi} \\ \sum_{i=1}^{n} a_{xi}a_{zi} & \sum_{i=1}^{n} a_{yi}a_{zi} & \sum_{i=1}^{n} a_{zi}{}^2 \end{bmatrix} \tag{5.5}$$

The three eigenvalues of *T* are denoted $\hat{\tau}_1$, $\hat{\tau}_2$, and $\hat{\tau}_3$ and the corresponding eigenvectors are **û₁, û**₂, and **û**₃. The fabric tensor eigenvalues and eigenvectors define the orthogonal principal axes. The two eigenvectors are **û₁ and û₃** corresponding to the direction along which the moment of inertia is minimized and maximized, respectively (Ketcham and Ryan 2004; Bhasin et al. 2011).

The DA is defined according to Eq. 5.6.

$$DA = \frac{\hat{\tau}_1}{\hat{\tau}_3} \tag{5.6}$$

where $\hat{\tau}_1$ and $\hat{\tau}_3$correspond to the minimum and maximum moment of inertia, respectively.

The Quant 3D software was developed by Ketcham and his group (Ketcham 2005; Ketcham and Ryan 2004) to analyze the X-ray scanned images in 3D. Quant 3D is a useful software that is used to compute MIL, SLD, and SVD. In this study, the Quant 3D software was used to determine the DA based on the SLD measurements according to Eq. 5.1.

Figure 5.23 shows the DA for the test samples. The results demonstrated that the degree of anisotropy decreases with the increase of compaction level (i.e. higher density) in test samples compacted using both vibratory and static rollers. Since the vibratory roller produced test samples with higher density at the corresponding number of passes (Fig. 5.21) compared to the static roller, the degree of anisotropy of test samples compacted using vibratory roller is lower than the one for test samples compacted using static roller. In addition, Fig. 5.21 shows that the vibratory roller produces uniform air void across the depth of test samples (especially towards in the top half) compared to static roller. These results are in good agreement with the previous findings in Fig. 5.17 where the anisotropy decreases with the increase in density (decease in percent air voids).

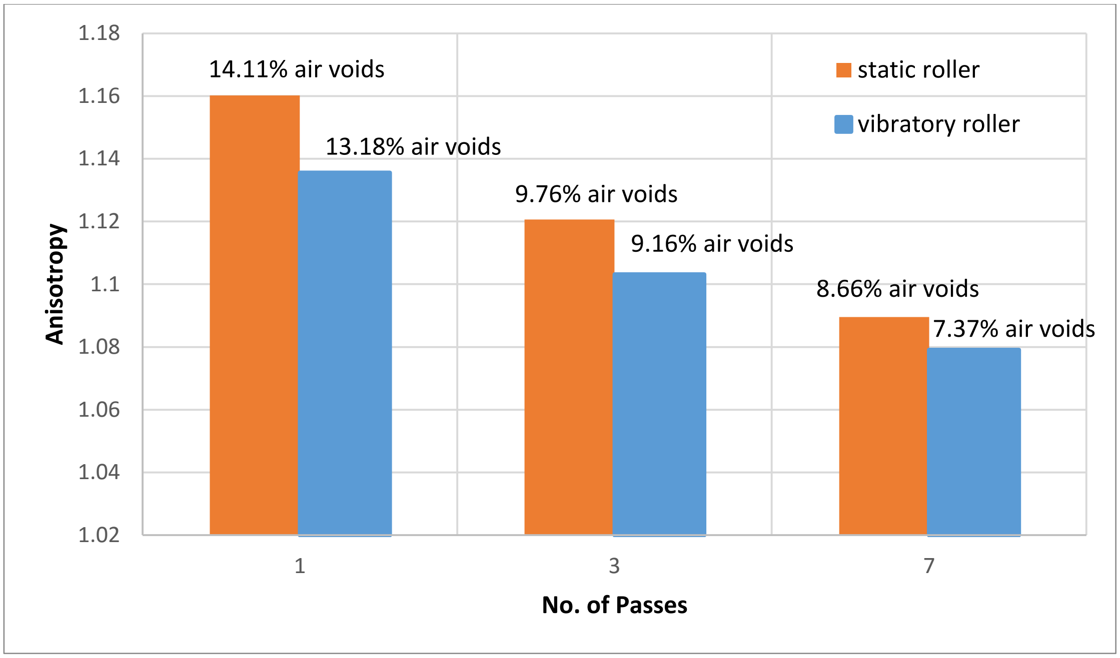

Figure 5.23 The Degree of Anisotropy with Respect to the Number of Passes and the Compaction Method.

5.6 Summary

In Chapter 5, the researchers evaluated the induced anisotropy of asphalt mixtures and studied the effect of mix design, level of confining pressure, temperature, and percent of air void on the degree of anisotropy. The results showed that the anisotropy is dependent on the mix design. Asphalt mixtures with coarser aggregate gradation were found to have higher level of anisotropy comparted to mixture with finer aggregate gradation. In addition, the anisotropy increased with the increase of both confining pressure and temperature. It is believed that the preferred orientation of the longest axes of the aggregate particles to the radial direction (perpendicular to the direction of compaction) contributes to the degree of anisotropy of asphalt mixtures under different confining pressure and temperature.

Under the hydrostatic pressure, the radial direction of the cylindrical test specimens always deforms larger than the axial direction. Furthermore, the researchers found that the percent of air void had a major effect on the anisotropy. It was found that the anisotropy ratio is 2.2 to 2.1 for 4% air void samples, while it jumped to 3.6 to 3.3 for 7% air void samples.

The analysis of the anisotropy using the X-ray CT images and Quant 3D software confirmed that degree of anisotropy decreases with the increase of density (i.e. decrease of percent air voids). In addition, the vibratory roller produced asphalt mixtures with more uniform air void and less anisotropy compared to static roller.

CHAPTER – 6 CONCLUSIONS AND RECOMMENDATIONS

6.1 Conclusions

The main objective of this study was to conduct a comprehensive evaluation of the viscoelastic Poisson's Ratio and degree of anisotropy of the asphalt mixtures under various conditions. The main findings of this study are summarized in this section.

Evaluation of VPR of Asphalt Mixtures

- The author presented and used accurate methods to calculate the VPR of asphalt mixture under various conditions. The percent error of incorrectly assuming the PR as the negative ratio of radial strain to axial strain was significant in some cases.
- The VPR increased with time for the unconfined test samples in both tension and compression because the shear relaxation was faster than the dilatational relaxation.
- The VPR decreased with time for the confined test samples where the dilatational relaxation was faster than the shear relaxation.
- The aggregate gradation was found to influence the VPR of asphalt mixture. Coarser asphalt mixtures were found to have lower VPR compared to finer ones.
- The moisture-conditioned samples were found to have relatively higher VPR compared to the dry samples at 19^{o}C. Also, the researchers found that the duration of moisture conditioning influences the VPR.
- The aging had a significant effect on the VPR. The aged samples had lower VPR compared to the non-aged samples because aging causes asphalt mixtures to behave more elastically.

Evaluation of Degree of Anisotropy of Asphalt Mixtures

- The degree of anisotropy is dependent on the mix design. Asphalt mixtures with coarser aggregate gradation were found to have higher level of anisotropy compared to the asphalt mixtures with finer aggregate gradation.
- The degree of anisotropy increased with the increase of confining pressure and temperature. Under the hydrostatic pressure, the radial direction of the cylindrical test specimens always deforms larger than the axial direction.
- The percent of air void had relatively high impact on the anisotropy ratio. The anisotropy ratio was in between 2.2 and 2.1 for 4% air void samples, and it jumped to 3.6 to 3.3 for 7% air void samples. The analysis of the anisotropy using the X-ray CT images and Quant 3D software confirmed that degree of anisotropy decreases with the increase of density (i.e. decrease of percent air voids).

6.2 Recommendations

- In this study, the aggregate gradation was found to be more dominant in influencing the VPR. It is recommended to assess the influence of the roundness and angularity of the aggregate particles on the VPR.
- It is recommended to study the effect of strain rate on VPR at different temperatures and a wider range of strain rates.
- Conduct further testing on asphalt mixtures with different gradations at different temperatures to verify the results of VPR under confining pressure.
- The anisotropy of asphalt mixture should be considered and incorporated in the models used for the analysis and performance evaluation of asphalt mixtures.

- It is recommended to study the influence of the aspect ratio of the asphalt mixture test samples on the anisotropy.

REFERENCES

AASHTO. (2002). “Preparing and determining the density of hot-mix asphalt (HMA) specimens by means of the Superpave gyratory compactor.” T312, Washington, DC.

AASHTO T283-89. (1993) Resistance of Compacted Bituminous Mixture to Moisture Induced Damage. Standard Specifications for Transportation Materials and Methods and Sampling and Testing Part II: Tests. Washington D.C.

Benedetto, H. D., Delaporte, B., and Sauzéat, C. (2007a). “Three dimensional linear behavior of bituminous materials: Experiments and modeling.” Int. J. Geomech., 7(2), 149–157.

Benedetto, H. D., Mondher, N., and Olard, S. F. (2007b). “Three dimensional thermo-viscoelastic behaviour of bituminous materials.” Road Mater. Pavement Design, 8(2), 285–315.

Bhasin, A., Izadi, A., & Bedgaker, S. (2011). Three dimensional distribution of the mastic in asphalt composites. Construction and Building Materials, 25(10), 4079-4087. doi:10.1016/j.conbuildmat.2011.04.046

Chou, P. C., and Pagano, N. J. (1967). Elasticity: Tensor, dyadic, and engineering approaches, D. van Nostrand Co., Princeton, NJ.

Darabi, M. K., Abu Al-Rub, R., Masad, E., Little, D., Kassem, E., Kim, S., Shakiba, M., and Rahmani, E. (2015). “PANDA: Pavement Analysis Using Nonlinear Damage Approach.” Texas A&M Transportation Institute, College Station, TX (in review).

Gaver, D. P. (1966). Observing Stochastic Processes, and Approximate Transform Inversion. Operations Research, 14(3), 444-459. doi:10.1287/opre.14.3.444

Elseifi, M. A., Al-Qadi, I. L., and Yoo, P. J. (2006). "Viscoelastic modeling and field validation of flexible pavements." *J. Eng. Mech.*, 132_2_, 172–178.

Glover, C. J., Davison, R. R., Domke, C. H., Ruan, Y., Juristyarini, P., Knorr, D. B., and Jung. S. H.(2005). "Development of New Method for Assessing Asphalt Binder Durability with Field Validation," Report FHWA/TX-05/1872-2, Texas Transportation Institute, College Station, Texas.

Grasley, Z. C., and Lange, D. A. (2007). "The viscoelastic response of cement paste to three-dimensional loading." Mech. Time-Depend. Mater., 11(1), 27–46.

Hilton, H. H. (2001). "Implications and constraints of time-independent Poisson ratios in linear isotropic and anisotropic viscoelasticity." J. Elast., 63(3), 221–251.

Huang, C., Masad, E., Muliana, A. H., and Bahia, H. (2007). "Nonlinearly viscoelastic analysis of asphalt mixes subjected to shear loading." Mech. Time-Depend. Mater., 11(2), 91–110.

Kassem, E., Awed, A., and Masad, E. (2016). "Effect of Compaction on Skid Resistance of Asphalt Pavements." the International Chinese European Workshop on Functional Pavement Design, June 29 to July 1, 2016, Delft, the Netherlands.

Kassem, E., Grasley, Z., and Masad, E. (2013). "Viscoelastic Poisson's Ratio of Asphalt Mixtures." Int. J. Geomech., 10.1061/(ASCE)GM.1943-5622.0000199, 162-169.

Kassem, E., Masad, E., Lytton, R., & Chowdhury, A. (2011). Influence of Air Voids on Mechanical Properties of Asphalt Mixtures. Road Materials and Pavement Design, 12(3), 493-524. doi:10.1080/14680629.2011.9695258

Kassem, E., Scullion, T., Masad. E., and Chowdhury, A. (2012). “Comprehensive Evaluation of Compaction of Asphalt Pavements and a Practical Approach for Density Predictions.” Transportation Research Record: Journal of the Transportation Research Board, 2268, 98-107

Ketcham, R. A. (2005). Computational methods for quantitative analysis of three-dimensional features in geological specimens. Geosphere, 1(1), 32. doi:10.1130/ges00001.1

Ketcham, R. A., & Ryan, T. M. (2004). Quantification and visualization of anisotropy in trabecular bone. Journal of Microscopy, 213(2), 158-171. doi:10.1111/j.1365-2818.2004.01277.x

Kim, J., Byron, T., Sholar, G., and Kim, S. (2008). “Comparison of a three-dimensional viscoelastic pavement model with full-scale field tests.” 87th Annual Meeting of the Transportation Research Board, Transportation Research Board, Washington, D.C.

Kim, J., Lee, H., and Kim, N. (2010). "Determination of Shear and Bulk Moduli of Viscoelastic Solids from the Indirect Tension Creep Test." J. Eng. Mech., 10.1061/(ASCE)EM.1943-7889.0000151, 1067-1075.

Lee, H. S., and Kim, J. (2009). “Determination of viscoelastic Poisson’s ratio and creep compliance from the indirect tension test.” J. Mater. Civ. Eng., 21(8), 416–425.

Maher, A., and Bennert, T. (2008). “Evaluation of Poisson’s ratio for use in the Mechanistic Empirical Pavement Design Guide (MEPDG).” Technical Rep. FHWA-NJ-2008-004, New Jersey Department of Transportation, Trenton, NJ.

Mamlouk, M.S., et al., 2002. Effect of anisotropy on compressive and tensile properties of asphalt mixtures. Journal of Testing and Evaluation, 30 (5), 432–438.

Masad, E., et al., 2002. Micromechanics-based analysis of stiffness anisotropy in asphalt mixtures. Journal of Material in Civil Engineering, 14 (5), 374–383.

Mehrez, L., Kassem, E., Masad, E., and Little, D. (2014). "Stochastic Identification of Linear-Viscoelastic Models of Aged and Unaged Asphalt Mixtures." J. Mater. Civ. Eng., 10.1061/(ASCE)MT.1943-5533.0001103, 04014149.

Poisson, S. D. (1829a). “Addition au memoire sur l’equilibre et le mouvement des corps elastiques.” Mem. Acad. Sci. Inst. France, 8, 623–627.

Poisson, S. D. (1829b). “Memoire sur l’equilibre et le mouvement des corps elastiques.” Mem. Acad. Sci. Inst. France, 8, 357–570.

Rahmani, E., Darabi, M. K., Al-Rub, R. K., Kassem, E., Masad, E. A., & Little, D. N. (2013). Effect of confinement pressure on the nonlinear-viscoelastic response of asphalt concrete at high temperatures. Construction and Building Materials, 47, 779-788. doi:10.1016/j.conbuildmat.2013.05.090

Read, W. T. (1950). “Stress analysis for compressible viscoelastic materials.” J. Appl. Phys., 21(7), 671–674.

Tashman, E, et al., 2001. International structure analysis of asphalt mixes to improve the simulation of SuperPave gyratory compaction to field condition. In: Proceedings of Association of Asphalt Paving Technologists. Vol. 70, 605–645. Lino Lakes, MN: Association of Asphalt Paving Technologists.

Tschoegl, N. W., Knauss, W. G., and Emri, I. (2002). “Poisson’s ratio in linear viscoelasticity—A critical review.” Mech. Time-Depend. Mater., 6(1), 3–51

Underwood, S, et al., 2005. Experimental investigation of anisotropy in asphalt concrete. Transportation Research Record: Journal of the Transportation Research Board, 1929, 238–247.

Wang, Q., & Zhan, H. (2015). On different numerical inverse Laplace methods for solute transport problems. Advances in Water Resources, 75, 80-92. doi:10.1016/j.advwatres.2014.11.001

APPENDIX A

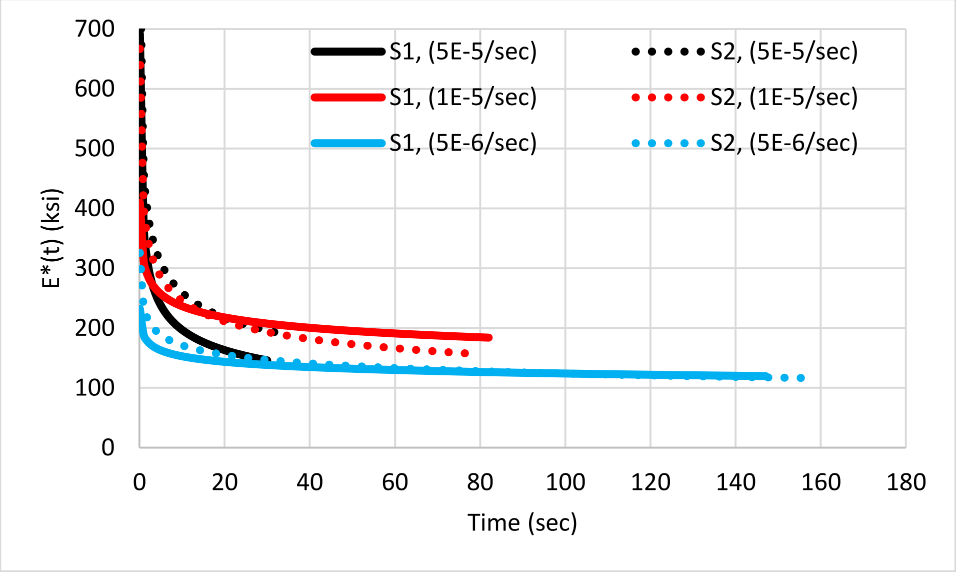

(a) E*(t)

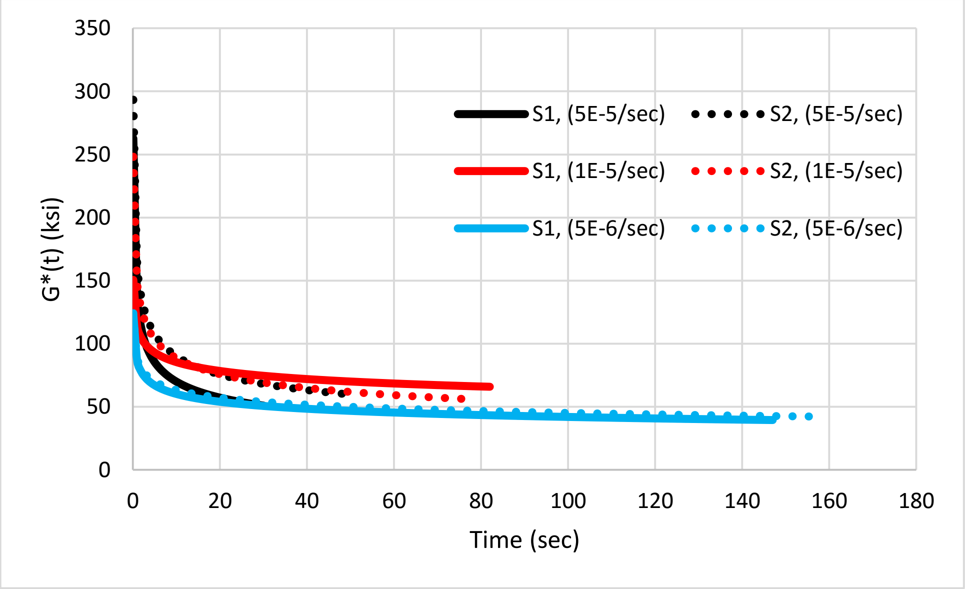

(b) G*(t)

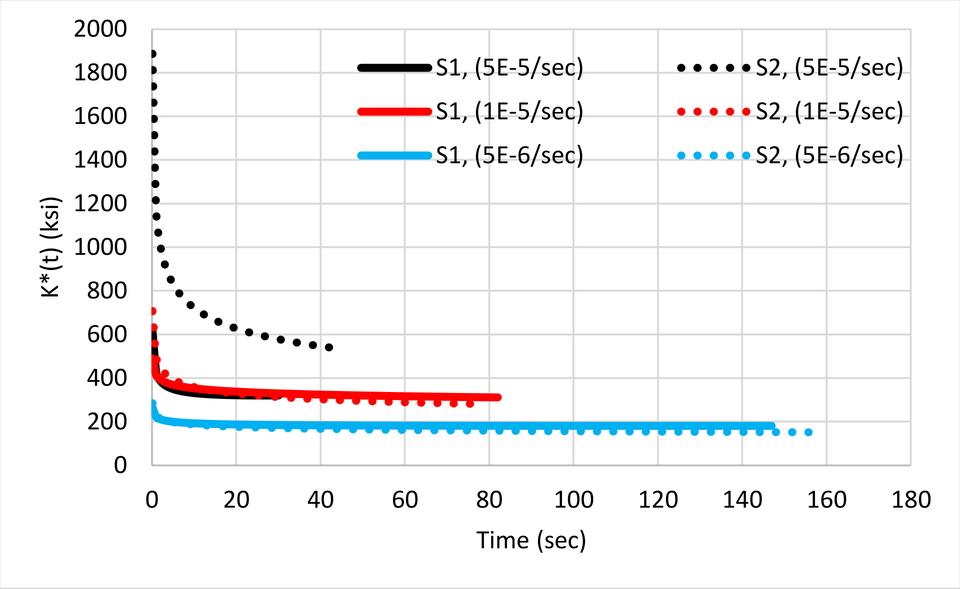

(c) K*(t)

Figure A.1 (a) E*(t), (b) G*(t), and K*(t) of Mix-1 at 5ºC

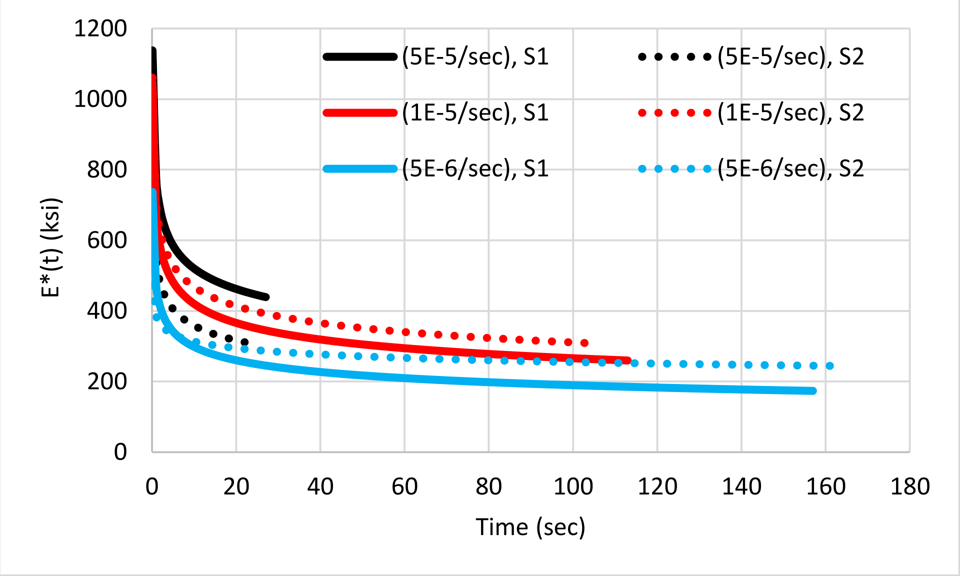

(a) E*(t)

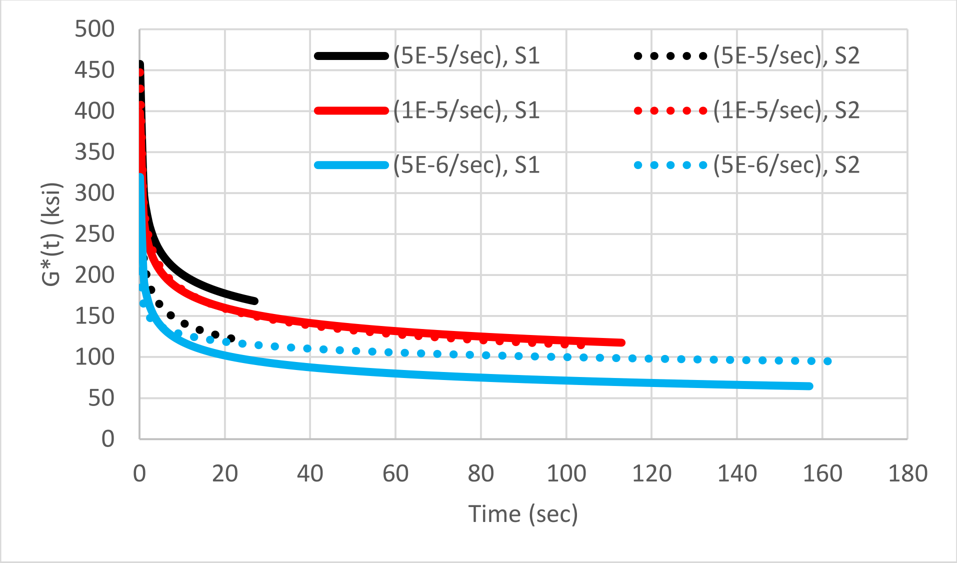

(b) G*(t)

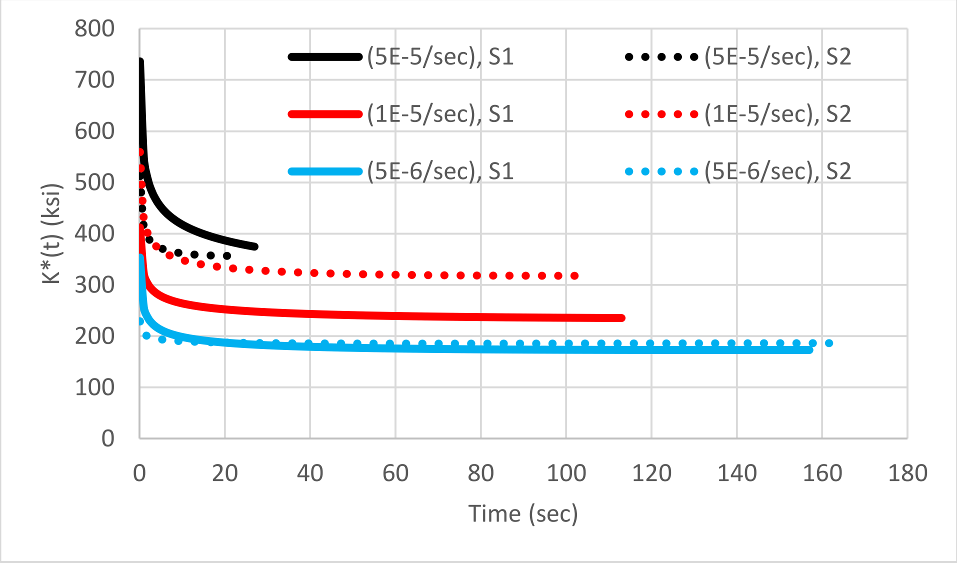

(c) K*(t)

Figure A.2(a) E*(t), (b) G*(t), and K*(t) of Mix-3 at 5ºC

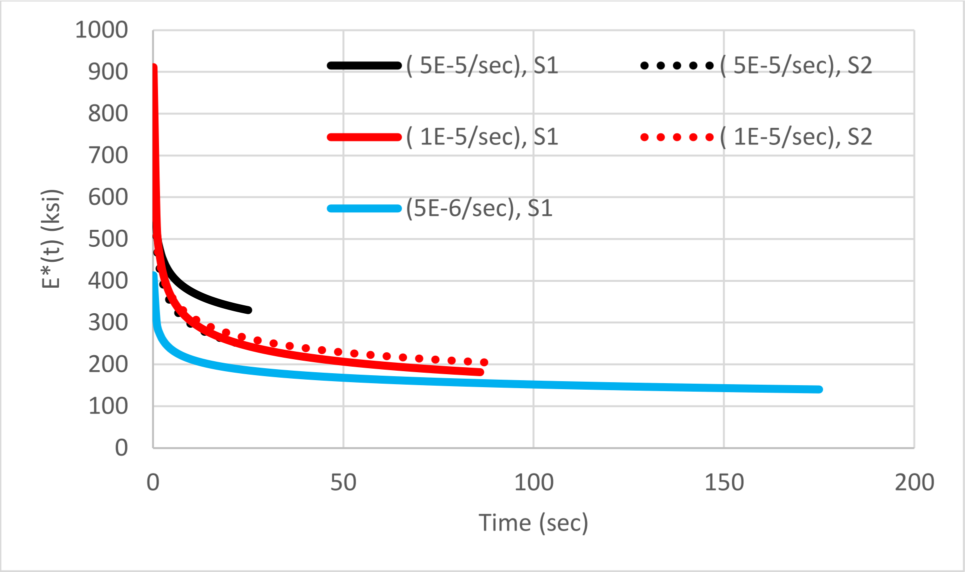
1000
900
800
700
600
500
400
300
200
100
0
E*(t) (ksi)
0
50
100
150
200
Time (sec)
(5E-5/sec), S1
(5E-5/sec), S2
(1E-5/sec), S1
(1E-5/sec), S2
(5E-6/sec), S1

(a) E*(t)

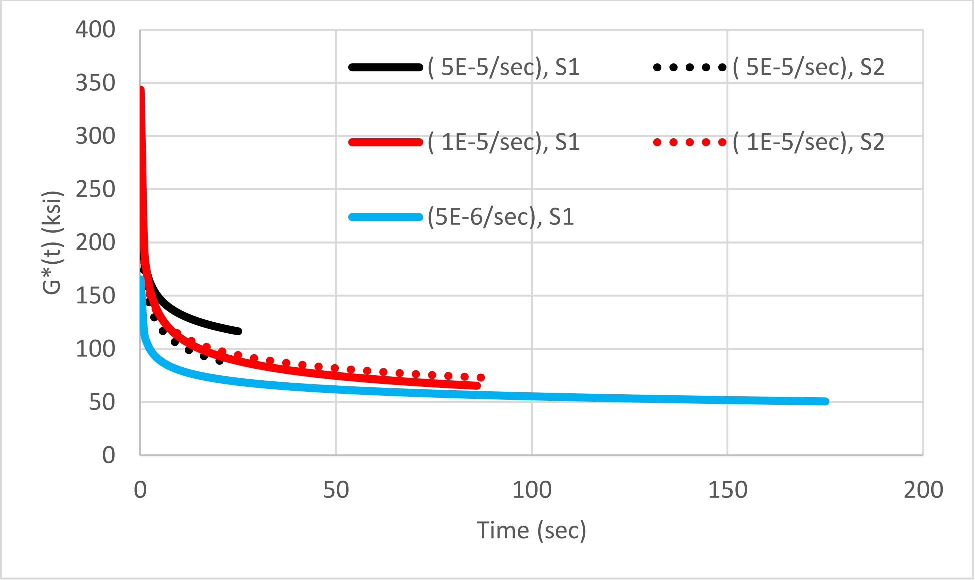
400
350
300
250
200
150
100
50
0
G*(t) (ksi)
0
50
100
150
200
Time (sec)
(5E-5/sec), S1
(5E-5/sec), S2
(1E-5/sec), S1
(1E-5/sec), S2
(5E-6/sec), S1

(b) G*(t)

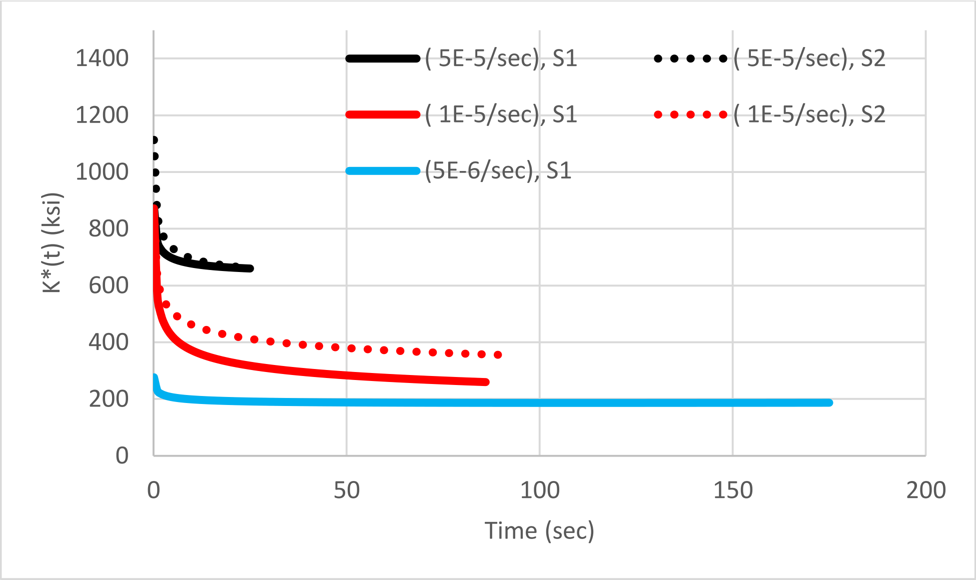

(c) K*(t)

Figure A.3 (a) E*(t), (b) G*(t), and K*(t) of Mix-5 at 5ºC

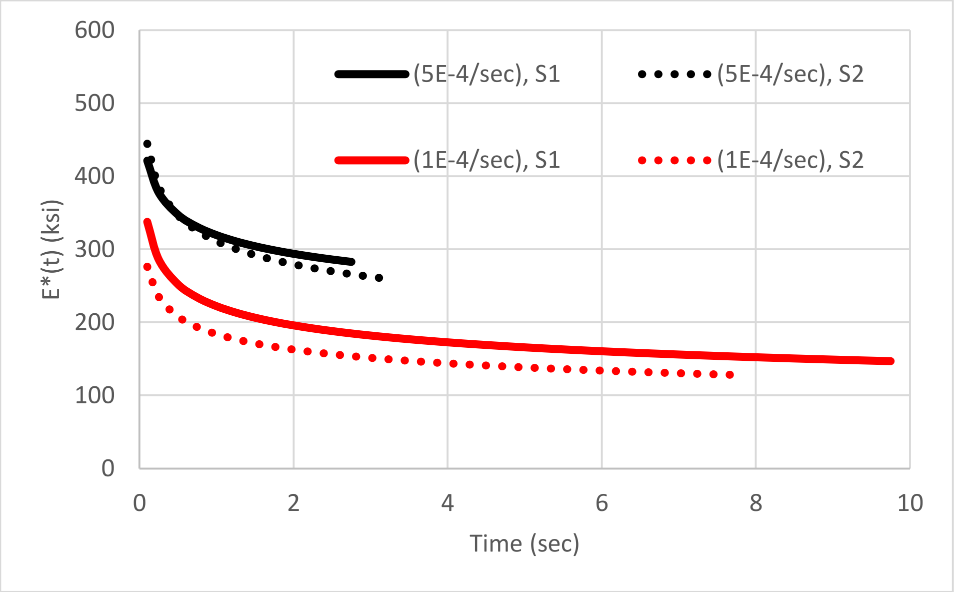

(a) E*(t)

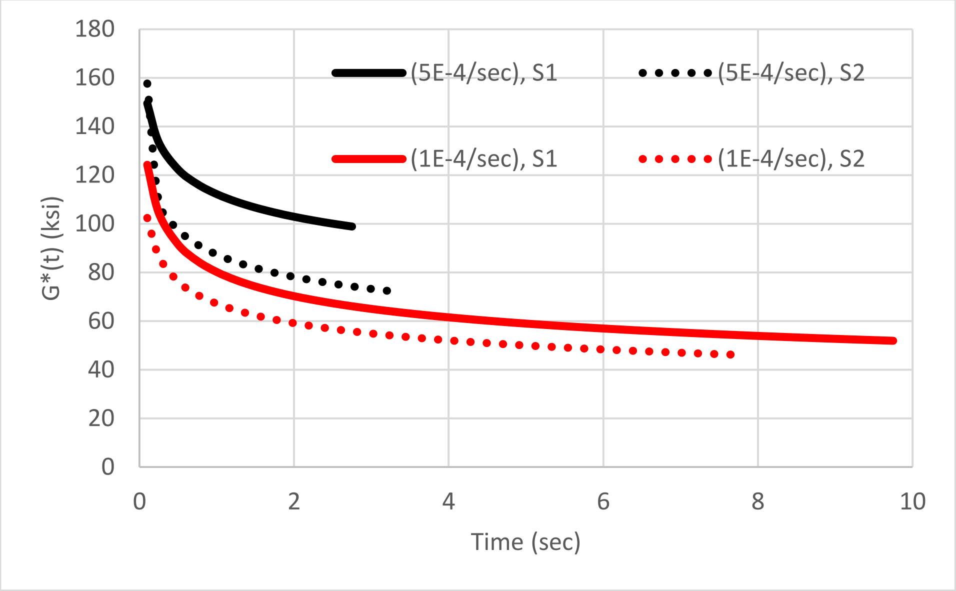

(b) G*(t)

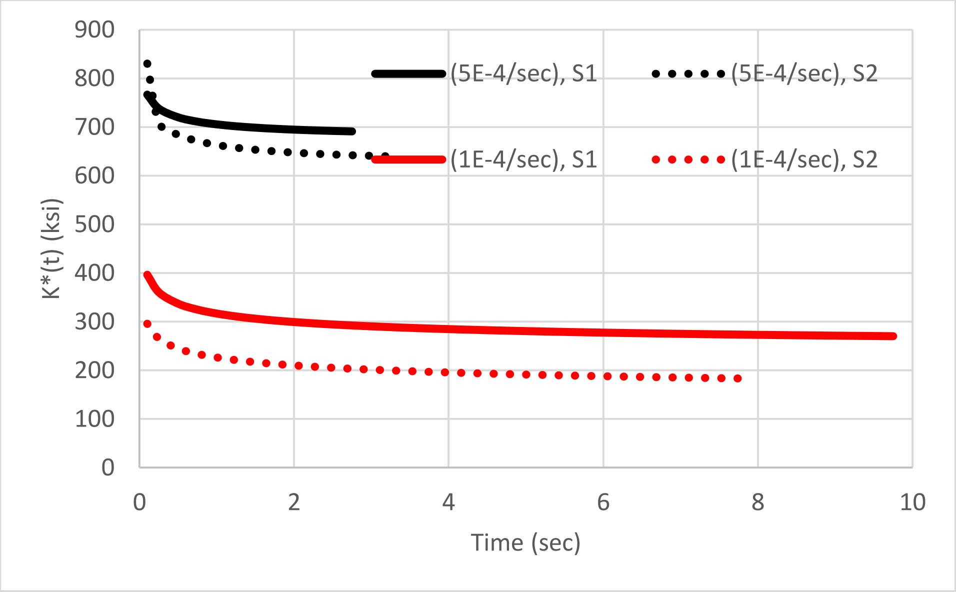

(c) K*(t)

Figure A.4 (a) E*(t), (b) G*(t), and K*(t) of Mix-5 at 19ºC

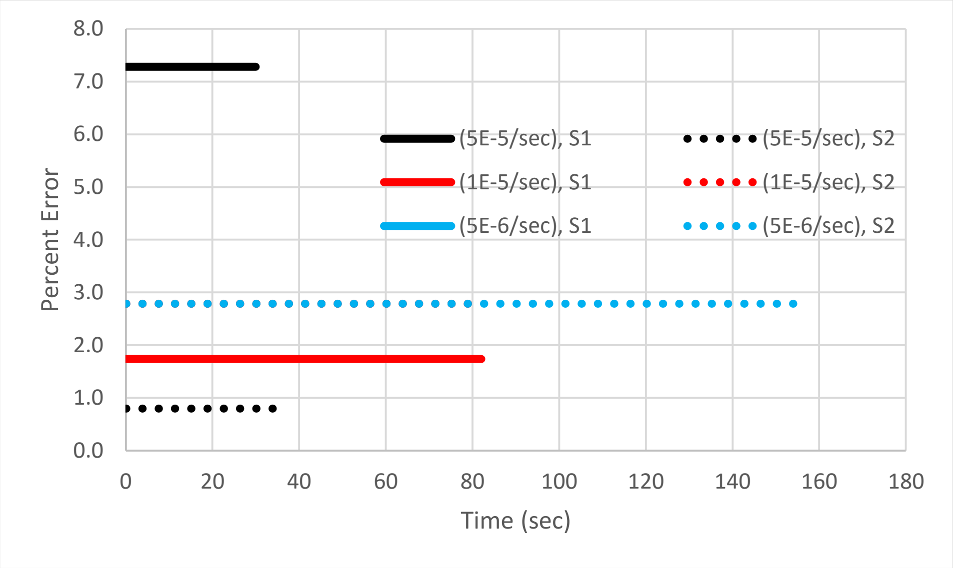

Figure A.5 Percent Error between PR and VPR for Mix-1 at 5ºC

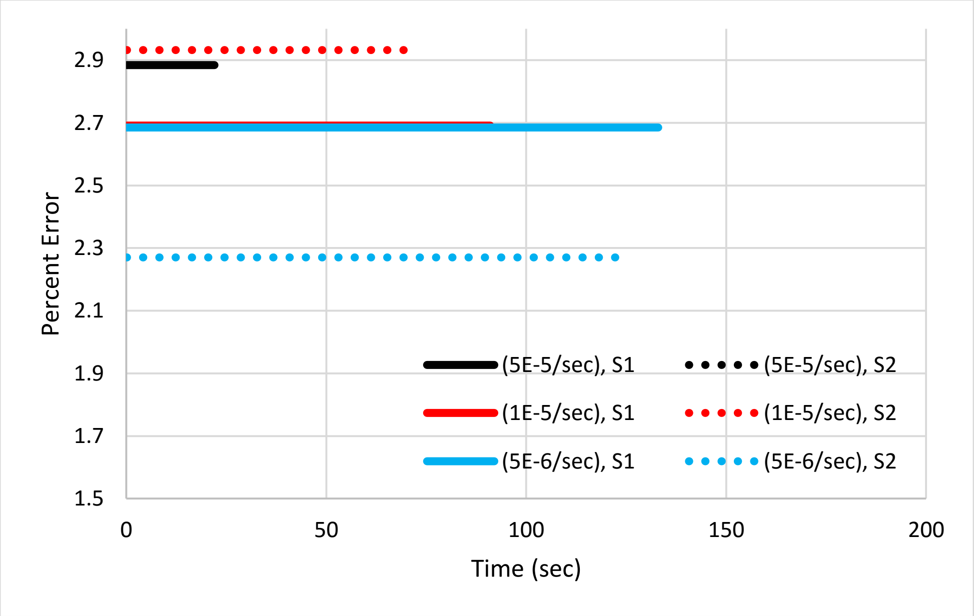

Figure A.6 Percent of Error between PR and VPR for Mix-2 at 5ºC

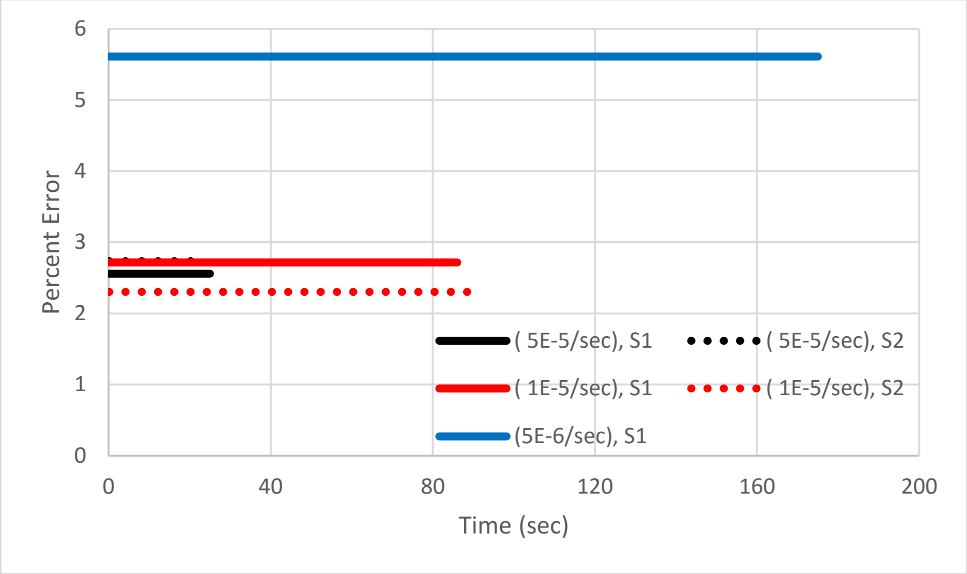

Figure A.7 Percent of Error between PR and VPR for Mix-5 at 5^{o}C

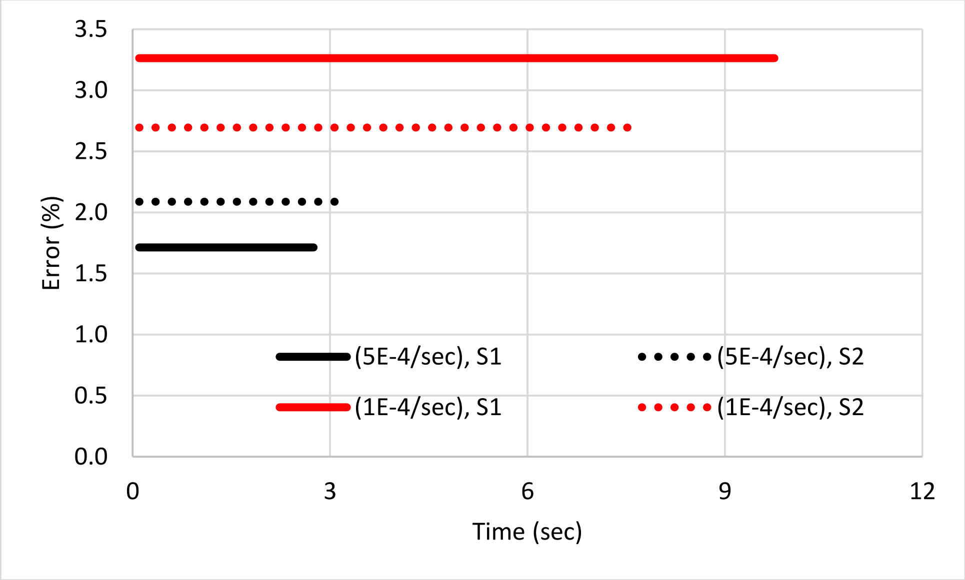

Figure A.8 Percent of Error between PR and VPR for Mix-5 at 19^{o}C

APPENDIX B

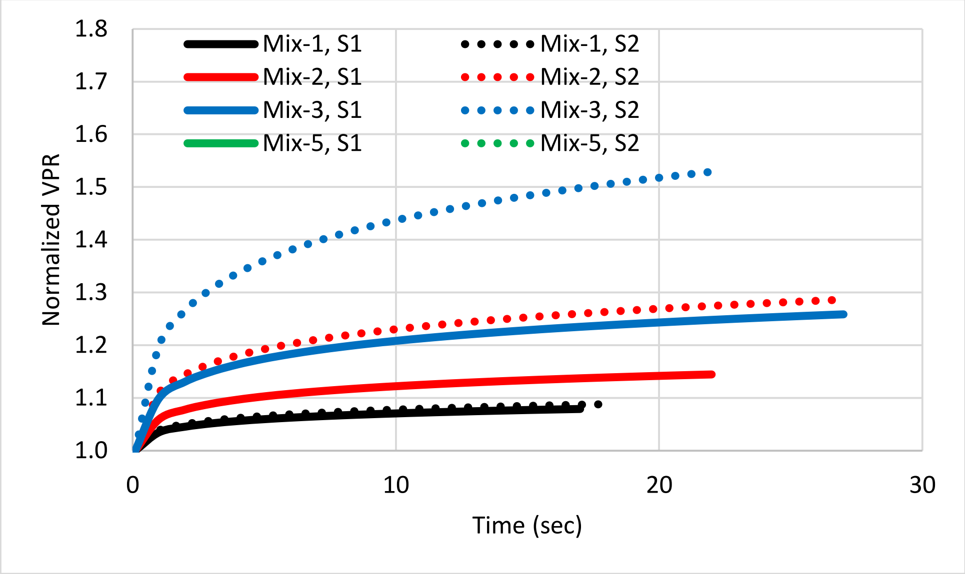

Figure B.1 Normalized VPR of Different Asphalt Mixtures at UCSR of 5E-5/sec

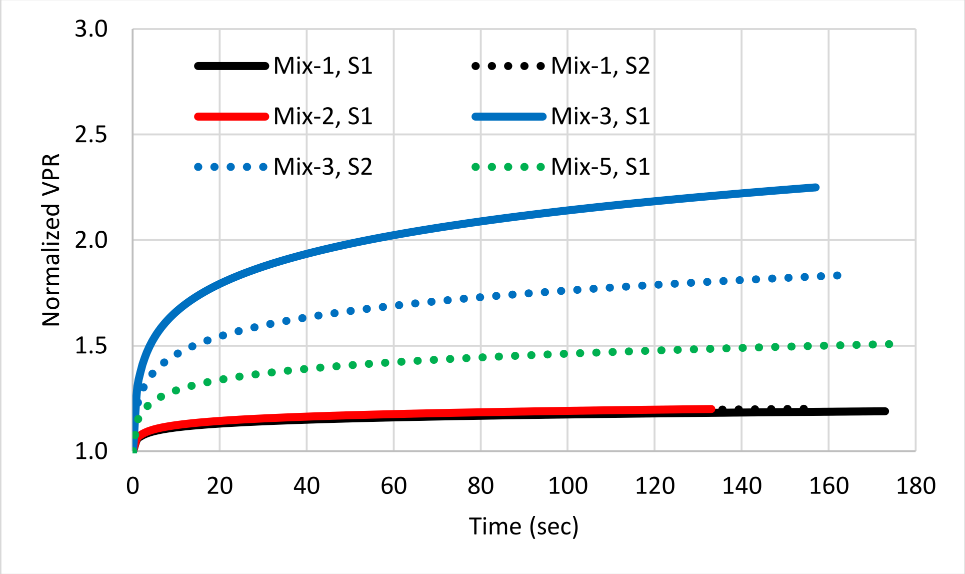

Figure B.2 Normalized VPR of Different Asphalt Mixtures at UCS of 5E-6/sec

APPENDIX C

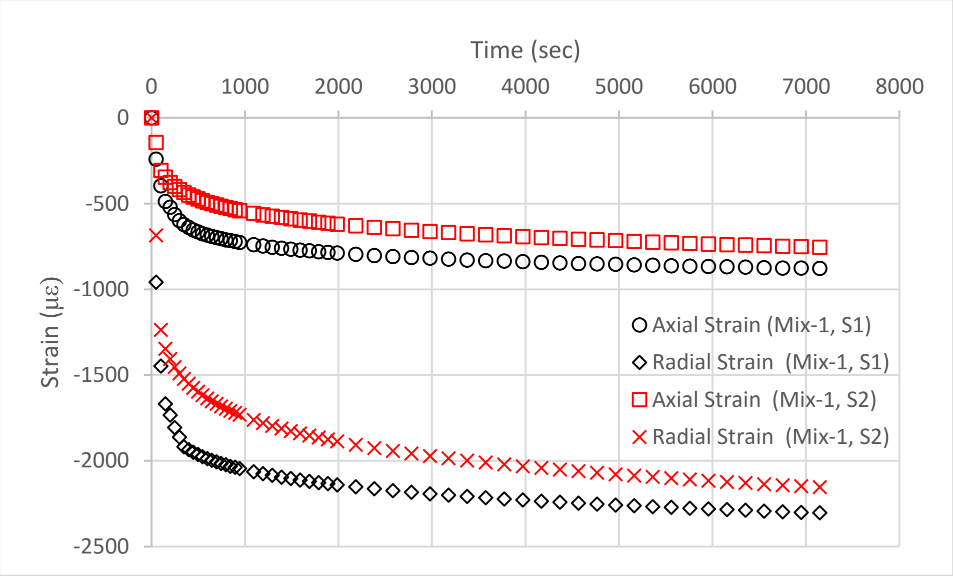

Figure C.1 Mix-1 Axial and Radial Strain under Hydrostatic Pressure of 20 psi at 55ºC

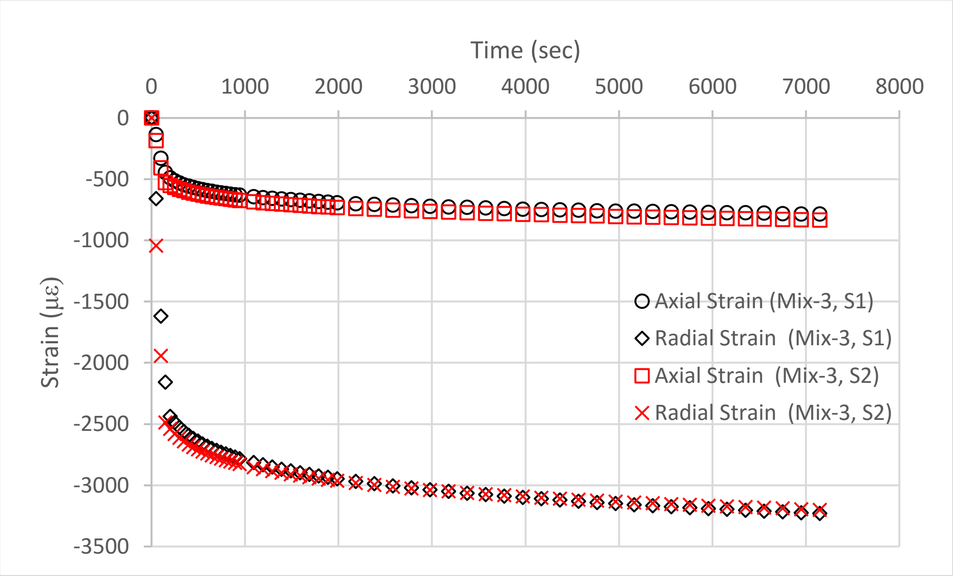

Figure C.2 Mix-3 Axial and Radial Strains under Hydrostatic Pressure of 20 psi at 55ºC

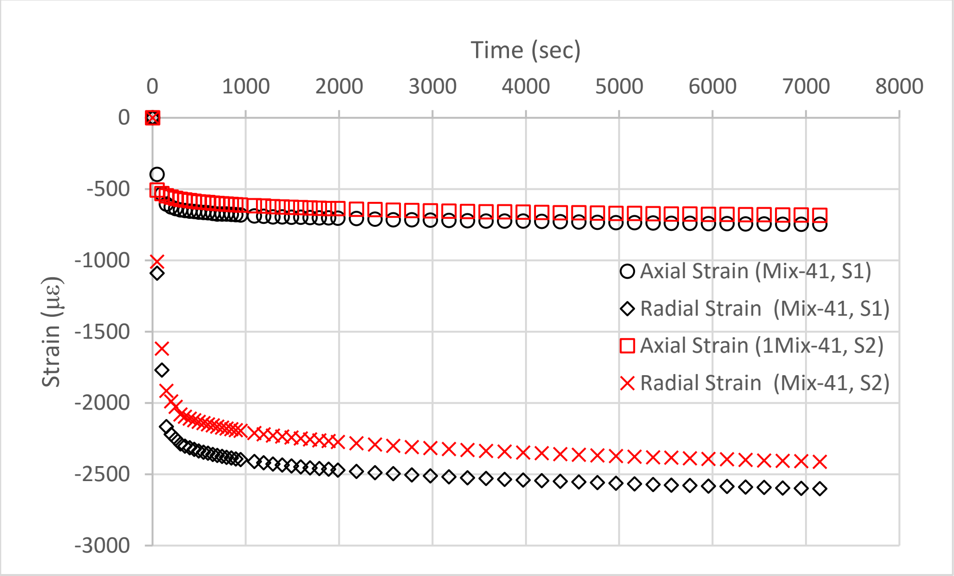

Figure C.3 Mix-4 Axial and Radial Strains under Hydrostatic Pressure of 20 psi at 55ºC

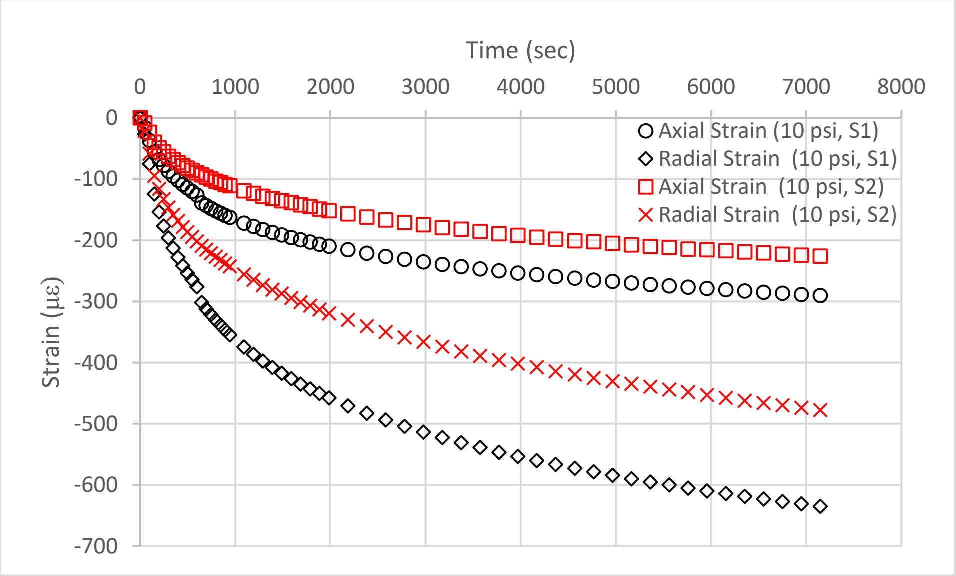

Figure C.4 Mix-4 Axial and Radial Strains under Hydrostatic Pressure of 10 psi at 19ºC

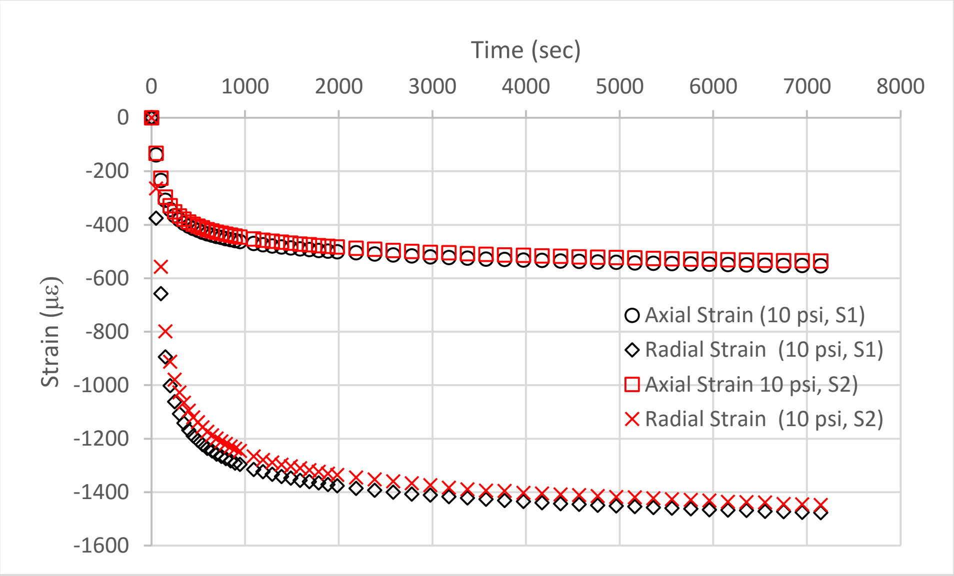

Figure C.5 Mix-4 Axial and Radial Strain under Hydrostatic Pressure of 10 psi at 40ºC

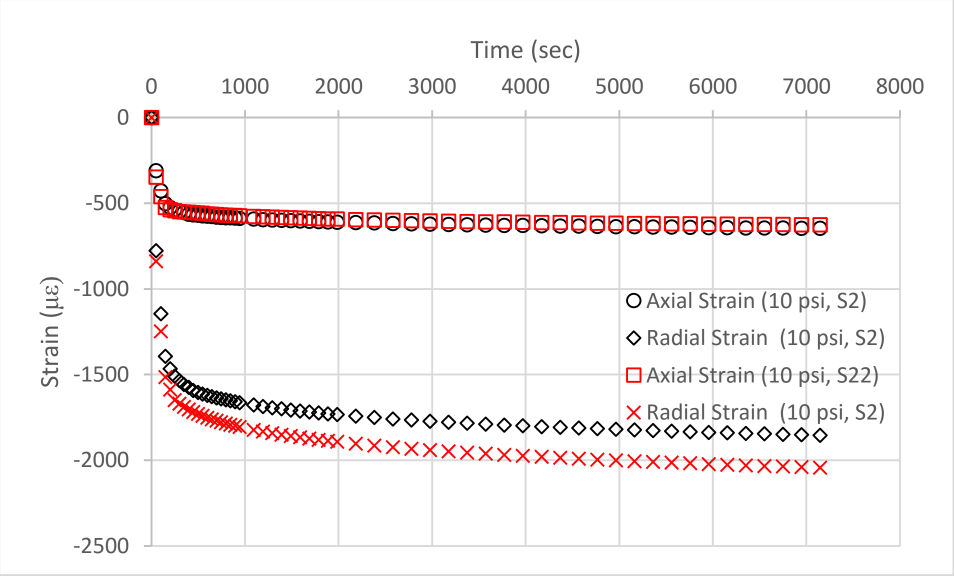

Figure C.6 Mix-4 Axial and Radial Strain under Hydrostatic Pressure of 10 psi at 55ºC

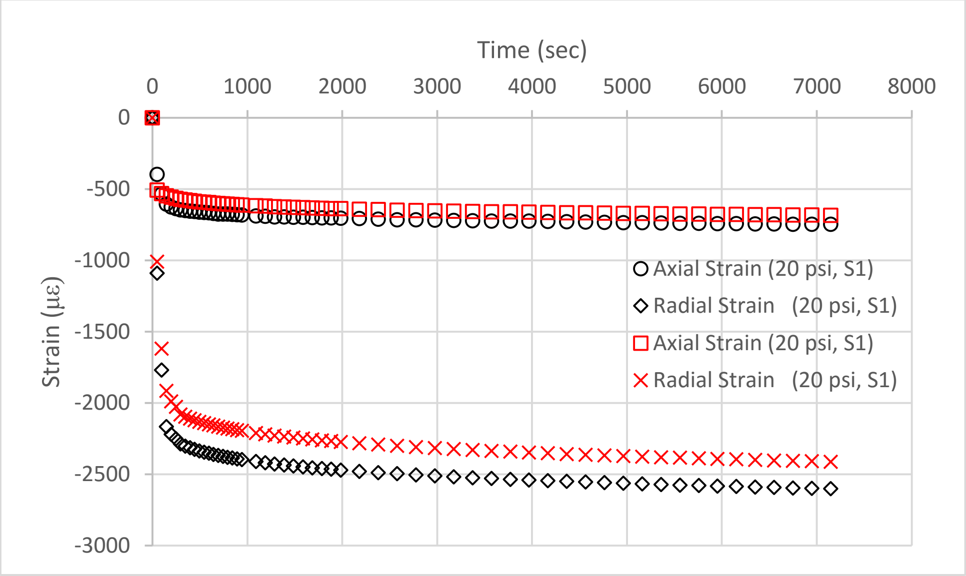

Figure C.7 Mix-4 Axial and Radial Strain under Hydrostatic Pressure of 20 psi at 55°C